QUANTIFYING THE SOIL FREEZING CHARACTERISTIC CURVE IN LABORATORY AND FIELD SOILS

A Thesis Submitted to the College of

Graduate and Postdoctoral Studies

In Partial Fulfillment of the Requirements

For the Degree of Master of Environment and Sustainability

In the School of Environment and Sustainability

University of Saskatchewan

Saskatoon

By

SETH KWAKU AMANKWAH

PERMISSION TO USE

In presenting this thesis in partial fulfillment of the requirements for a Postgraduate degree from the University of Saskatchewan, I agree that the Libraries of this University may make it freely available for inspection. I further agree that permission for copying of this thesis in any manner, in whole or in part, for scholarly purposes may be granted by the professor or professors who supervised my thesis work or, in their absence, by the Head of the Department or the Dean of the College in which my thesis work was done. It is understood that any copying or publication or use of this thesis or parts thereof for financial gain shall not be allowed without my written permission. It is also understood that due recognition shall be given to me and to the University of Saskatchewan in any scholarly use which may be made of any material in my thesis.

DISCLAIMER

Reference in this thesis/dissertation to any specific commercial products, process, or service by trade name, trademark, manufacturer, or otherwise, does not constitute or imply its endorsement, recommendation, or favoring by the University of Saskatchewan. The views and opinions of the author expressed herein do not state or reflect those of the University of Saskatchewan and shall not be used for advertising or product endorsement purposes.

Requests for permission to copy or to make other uses of materials in this thesis/dissertation in whole or part should be addressed to:

Head of the School of Environment and Sustainability
117 Science Place
University of Saskatchewan
Saskatoon, Saskatchewan S7N 5C8
Canada

OR

Dean
College of Graduate and Postdoctoral Studies
University of Saskatchewan
116 Thorvaldson Building, 110 Science Place
Saskatoon, Saskatchewan S7N 5C9
Canada

ABSTRACT

The soil freezing characteristic curve (SFC) controls the hydraulic properties of soils and is especially crucial in understanding snowmelt infiltration and runoff, frost heave formation and thawing settlement in frozen soils. The SFC can be modelled by combining information from the soil moisture characteristic curve of unfrozen soils (SMC) with the Generalized Clapeyron Equation (GCE). While such an approach is straightforward and involves no additional free parameters, the resulting SFC is not always consistent with those observed in the laboratory and field. This study was therefore designed to obtain both laboratory and field data that quantifies the SMC and SFC for different soil textures and salinities and to compare the results with those obtained from the GCE and other alternative relationships.

In the laboratory, the SMC of a silica sand was measured using a Hydraulic Property Analyzer (HYPROP). The SFC of the same sand was measured using a series of column experiments with controlled total water content and pore-water salinity. In the field, data were collected from the St Denis National Wildlife Area (SDN), a mixed grassland cropped site in the Canadian prairies in Saskatchewan and the Boreal Ecosystem Research and Monitoring Sites (BERMS) Old Jack Pine (OJP) site in Saskatchewan, Canada. Three alternative models for the SFC were developed (capillary, salt exclusion, and the combined capillary salt models), and compared with observed data from the laboratory and field experiments.

The results show that the column experiments were successful in producing well-defined SFCs that matched expectations, where the form of the decrease in liquid water content with temperature was similar to the form of the SMC. Increasing the salinity resulted in enhanced freezing point depression as was expected. The field SFCs followed the same trend as those measured in the laboratory. The modelling results suggest that salinity is a dominant control on the SFC in real soils and that the combined capillary salt model is the most realistic of the three models considered in predicting liquid water content in frozen soils.

ACKNOWLEDGEMENTS

I give thanks to the almighty GOD for granting me the strength, knowledge, confidence and resilience and for making this Master's a dream come true.

My warmest gratitude goes to my mentor, tutor and supervisor who also doubled as my dad, Dr Andrew Ireson, for his consistent and unwavering support, guidance and encouragement throughout my Master's degree. Your advice, directions, positivity, and feedbacks were very critical to the completion of this thesis and to that, I say I am grateful. Special thanks to my committee members, Dr. Yanping Li (Chair), Prof. Charles Maule, Dr. Christopher Spence and my external examiner, Prof. Bing Si, for evaluating my work and giving me constructive feedback.

I also acknowledge the financial support for this research and my Master's degree from the Global Institute for Water Security through the Global Water Futures program.

I would also want to acknowledge Rosa Brennen and Cody Miller for helping me with my laboratory experiments. My next thanks go to all the faculty and students at the School of Environment and Sustainability and the Global Institute for Water Security for being a supportive family especially Ines, Sujan, Dr. Bam, Richard, Menna, Morgan, Thyrone, and Haley.

Lastly, I would like to thank my family and friends here and in Ghana for being an anchor and an emotional booster throughout this journey.

TABLE OF CONTENTS

LIST OF TABLES

LIST OF FIGURES

CHAPTER 1

INTRODUCTION

1.1 Background

In cold regions, the way that ice and liquid water are held in the soil pore space plays a significant role in heat, solute and water transport (Spaans & Baker, 1996; He et al., 2016; Watanabe & Osada, 2017), which in turn influence winter evapotranspiration, snowmelt infiltration and runoff (Christensen et al., 2013; He et al., 2016), frost heave formation, thawing settlement, and frost depth penetration in frozen soils. Good knowledge of the properties of frozen soils is crucial in erosion control and flood risk assessment during spring melt in cold climates. In engineering, information about these properties is employed in infrastructure development such as the construction of roads, pavements, airport runways, bridges and railway lines. Further, in agronomy, these properties are useful in understanding microbial metabolism (Oquist et al., 2009; He et al., 2016; Watanabe & Osada, 2017) and crop water uptake in frozen soils as well as estimating water requirements for winter crops.

Unlike pure-free water (or bulk water) which freezes at 0℃ (at pressure = 1 atm) (Williams & Smith, 1989, p. 174), soil pore water is found to freeze progressively at sub-zero temperatures (Zhang & Liu, 2018; Hayashi, 2013; Williams & Smith, 1989, p. 175). Such a phenomenon is termed as freezing point depression. As a result of freezing point depression, some water remains as a liquid in frozen soils pores. Studies have attributed freezing point depression to 1) capillarity and adsorption (Williams & Smith, 1989, p. 5; Spaans & Baker, 1996; Zhou et al., 2018), and 2) the presence of salts (salinity effects) (Williams & Smith, 1989, p 5; Williams, 1970, p. 16; Williams, 1964; Watanabe & Mizoguchi, 2002).

Freezing can be explained based on free energy (FE). Spontaneous processes, such as the phase change process, always occur to minimize free energy. Ice (i) and liquid water (l) can co-exist only when they have equal free energy, and this occurs at 0 ℃ for bulk water (which is defined as T_0, ℃) (Zhang & Liu, 2018). Above T_0, liquid water has lower free energy than ice, and therefore liquid water is the stable phase. When the temperature of bulk water drops below T_0, the free energy of the liquid phase becomes higher than that of the solid phase. This drives the transformation of liquid water into ice, and ice becomes the stable phase. However, in any individual soil pore, the effects of salts and the attractive forces generated with the soil solids (capillarity and adsorption forces) reduce the free energy of the liquid water, so that liquid water does not freeze at T_0. For freezing to proceed, the temperature must reduce further to bring the free energy of ice below that of the depressed liquid water (the freezing temperature of the depressed liquid water is defined as T_f, ℃). The effect of salt and capillary forces on the freezing point of soil water is progressive, which is to say the water in the continuum of soil pore spaces has a distribution of freezing temperatures and freezing occurs progressively as the temperature drops below T_0. In terms of the capillary effect, the capillary forces and thus the freezing point of the water in an individual pore depends upon the pore size (analogous to matric potential), so smaller pores have lower freezing temperatures (Spaans, 1994). In terms of salt, during freezing, salt is excluded from the ice making the resulting solution more concentrated, and thus the freezing temperature of the remaining liquid water is further depressed (Spaans & Baker, 1996; William, 1970, p. 17).

Freezing point depression is quantified at the soil continuum scale through the freezing characteristic curve (SFC). The SFC relates the liquid water content to temperature in frozen soils. The SFC is analogous to the soil moisture characteristic curve (SMC) (soil matric potential versus moisture content) in unfrozen soils (Spaans & Baker, 1996; Flerchinger et al., 2006; Koopmans & Miller, 1966). The widely used generalized Clapeyron equation (GCE) assumes that in frozen conditions the temperature predicts an equivalent effective soil matric potential (Zhang & Liu, 2018; Mohammed et al., 2018; Teng, 2020). Based on this assumption, the GCE has been employed extensively in literature for establishing the SFC with information from the SMC. The advantage of using such an approach to quantify the SFC is that there are no additional unknown parameters, beyond those that describe the SMC for the same soil. While such an approach is straightforward

and inexpensive, the effects of salts are not accounted for explicitly (the GCE accounts for the sole effect of capillary forces on the freezing point), and the resulting SFC is not always consistent with those observed in the field and laboratory. Secondly, there is limited published work that shows how well this theoretical relationship (GCE) fits with field and laboratory observations of the SFC. The aim of this work, therefore, is to obtain both laboratory and field data that quantifies the SMC and SFC for different soil textures and salinities and to compare the results with those obtained from the GCE and other alternative relationships. Insights from such studies will increase the capacity of cold climate models in quantifying the liquid water content more explicitly. Improvement in the prediction of liquid water content in frozen soils will translate into a more accurate prediction of hydrological processes and events in cold climates.

1.2 Research Objectives

The specific objectives of this study are to;

1) Obtain laboratory and field data that characterize the soil moisture and soil freezing characteristic curves for varying soil types and soil salinities.
2) Test how well the observed relationships from new laboratory experiments where salinity is controlled can be explained by the alternative (capillary and salinity effect) models.
3) Test how well the observed relationships from established field experiments at a range of diverse sites can be explained by the alternative (capillary and salinity effect) models.

1.3 Thesis structure

This thesis is organized into five chapters. This chapter is an introduction to the problem and presents the research objectives. Chapter two is a literature review that covers relevant topics in unfrozen and frozen soil physics. Chapter three describes the methods employed in the field and laboratory experiments, including experimental set-ups, and the acquisition, storage, processing, and analysis of data. Chapter four presents and discusses the results. Lastly, the insights from this work will be summarized in chapter 5.

CHAPTER 2

LITERATURE REVIEW

2.1 Context of this research

The coexistence of liquid water with ice in frozen soil, as a function of temperature, is an important property of frozen soils. For instance, the hydraulic, thermal and mechanical properties of frozen soils depend on the liquid water and ice contents (Zhou et al., 2014; He et al., 2016). These properties, in turn, controls water, solute and heat transport in frozen soils (Spaans & Baker, 1996; He et al., 2016; Ren & Vanapalli, 2020; Watanabe & Osada, 2017), water uptake by plants, soil microbial metabolism (Öquist et al., 2009; He et al., 2016; Watanabe & Osada, 2017) and evaporative water loss from frozen soils as well as snowmelt infiltration and runoff in frozen soils (Christensen et al., 2013; He et al., 2016). Thus, research on liquid water content is vital in improving agricultural productivity, mitigating flooding and soil erosion during spring melt and for engineering application in cold climates. Such studies are also crucial in modelling moisture and thermal fluxes in surface and subsurface soil systems.

2.2 Physics of unfrozen soils

2.2.1 Soil moisture

Soil moisture from a physical viewpoint can be defined as water stored in soil pores. There are two ways to quantify soil moisture: as an equivalent storage of water S (mm) within some depth of the soil profile, or as a water content (i.e. a relative mass or volume of the water relative to the bulk or dry soil mass/volume). Water content can be expressed in gravimetric, θ_g ($g\ g^{-1}$), or volumetric, θ_v ($m^3\ m^{-3}$) terms (Romano, 2014).

Expressions of the volumetric and gravimetric moisture contents are provided in Equations 2.1, and 2.2, respectively.

$$\theta_g = \frac{m_w}{m_d} \tag{2.1}$$

$$\theta_v = \frac{V_w}{V_t} \tag{2.2}$$

$$\theta_v = \theta_g \cdot \frac{\rho_b}{\rho_w} \tag{2.3}$$

Where m (kg), V (m^3), and ρ ($kg\ m^{-3}$) stands for mass, volume and density, respectively. Subscripts d, w, t, and b represent oven-dried soil, wet soil, total, and bulk soil, respectively. θ_g and θ_v are related through Equation 2.3 above. Soil moisture storage is related to the volumetric water content through the relation

$$S = \int_{z=z_1}^{z_2} \theta_v dz \tag{2.4}$$

Where z is the soil depth. Typically, this will be applied over the depth range z_1 = 0 (the ground surface) and z_1 = depth of the root zone. For agronomic purposes, two soil moisture storage thresholds are identified: field capacity and permanent wilting point (Susha Lekshmi et al., 2014). Moisture at field capacity is the moisture retained in the soil after gravitational moisture has drained and movement of capillary water is negligible (Day & Ludeke, 1993, p. 19; Susha Lekshmi et al., 2014) (only capillary and hygroscopic moisture exist), while moisture at permanent wilting point refers to the moisture content at which plants cannot recover from wilting (Susha Lekshmi et al., 2014; Silva et al., 2014). The available water capacity, that is the water that is available to plants, is the difference between the moisture content at field capacity and permanent wilting point (Grewal et al., 1990; Susha Lekshmi et al., 2014; Silva et al., 2014).

2.2.2 Soil water potential

Soil water potential refers to the work that would need to be done to move an infinitesimal amount of water from a reference point in the soil to a pool of pure free water (Irwin. Remson, 1962, p. 66). Water potential encompasses matric, pressure, gravitational, and solute potential (Campbell, 1988).

Gravitational potential

Gravitational potential is the energy of soil water due to its position above or below a datum (Campbell, 1988; Hohmann, 1997). Consider an object at a height z meters above a datum (Figure 2-1).

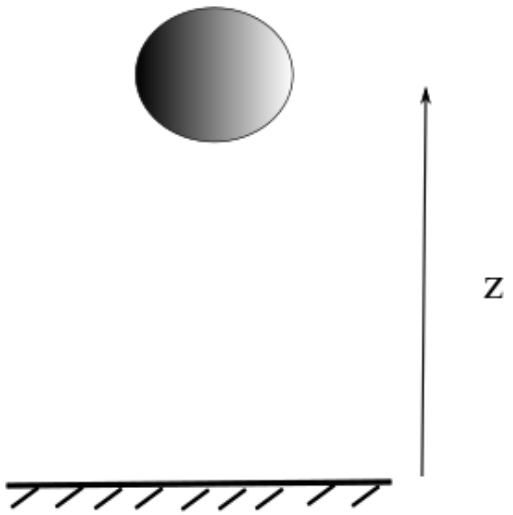

Figure 2-1: Elevation of water molecule relative to a reference datum

The body will have a gravitational potential energy $E_G\ (J)$ equal to:

$$E_G = m \cdot g \cdot z \tag{2.5}$$

Where g $(m\ s^{-2})$ is acceleration due to gravity. Given the situation above, a volume of water at an elevation z meters above a reference datum (Figure 2-2) will have the same potential energy as in Equation 2.5.

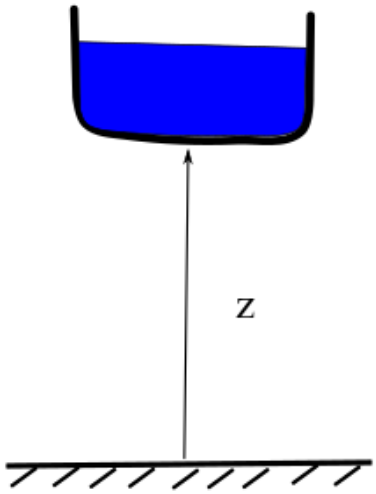

Figure 2-2: A volume of water at a height (Z) above a datum

But the mass of water (m), and weight of water (W) are given as

$$m = \rho_w \cdot V_w \tag{2.6}$$

$$W = \rho_w \cdot V_w \cdot g \tag{2.7}$$

Where subscript w stands for water. Hence, the gravitational potential energy becomes

$$E_G = \rho_w \cdot V_w \cdot g \cdot z \tag{2.8}$$

The gravitational potential energy per unit volume of water, E_{vG} $(J\ m^{-3})$ is given by

$$E_{vG} = \rho_w \cdot g \cdot z \tag{2.9}$$

The gravitation potential energy per unit weight of water (Equation 2.8 divided by Equation 2.7) ψ_z (m) is given by

$$\psi_z = z \tag{2.10}$$

Potential energy per unit weight of water is a convenient unit to work with, having units of length, and is referred to as head. Thus, ψ_z is referred to as the gravitational head.

Pressure Potential

Pressure potential refers to the hydrostatic pressure exerted by soil water (Clark, 1990).

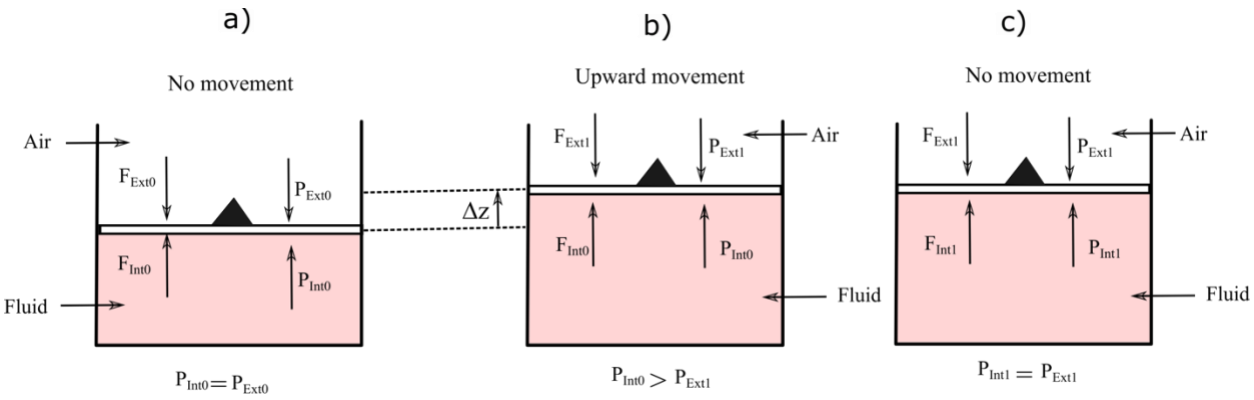

Figure 2-3: Pressure exerted by a piston in a cylinder (after Anderson, 2005, P. 39)

Consider a piston in a cylinder (Figure 2-3). The force exerted by each phase is the product of the pressure and surface area as in Equation 2.11.

$$F = P \cdot A \tag{2.11}$$

At equilibrium, there is no pressure difference $P_{Int0} = P_{Ext0}$ (Figure 2.3a), and the resultant force, F_R, of the system is

$$F_R = F_{Int0} - F_{Ext0} = 0 \tag{2.12}$$

Where subscripts Int and Ext means internal and external. 0 and 1 are the first and second time steps, respectively. Since the net force is zero, there will be no work done. When there is a reduction in the external pressure, where $P_{Ext1} < P_{Ext0}$ the pressure difference creates an upward resultant force given by

$$F_R = F_{Int0} - F_{Ext1} > 0 \tag{2.13}$$

The net force will result in work in the form of the expansion of the fluid, and the upward movement of the piston through a distance Δz (m) (Figure 2-3b). The work done by the net force is the product of the net force applied and the distance moved.

$$W = F_R \cdot \Delta z \tag{2.14}$$

$$W = (P_{Int0} - P_{Ext1}) \cdot A \cdot \Delta z \tag{2.15}$$

$$W = \Delta P \cdot \Delta V \tag{2.16}$$

When work is done, the system moves from one (higher) potential to another (lower) potential, i.e. $W =$ change in potential, hence, the pressure potential, E_p (J), in a given state is given as:

$$E_p = P \cdot V \tag{2.17}$$

The pressure potential per unit volume of water, E_{vP}, is given by

$$E_{vP} = P \tag{2.18}$$

The pressure potential per unit weight of water (Equation 2.17 divided by Equation 2.7), also known as pressure head, ψ_p (m), is given by

$$\psi_p = \frac{P}{\rho_w \cdot g} \tag{2.19}$$

After the piston has moved through a distance Δz (m), a new equilibrium is established where there is no difference in pressure (Figure 2-3c).

Matric potential

The above discussion of pressure head applies to soils that are under positive hydrostatic pressures. In partially saturated soils, water is retained in the soil pores due to matric forces (Williams, 1964). In smaller pores, there is an attraction between individual water molecules (cohesion) and with the wall of the soil pore (Campbell, 1988) (adhesion) (Figure 2-4).

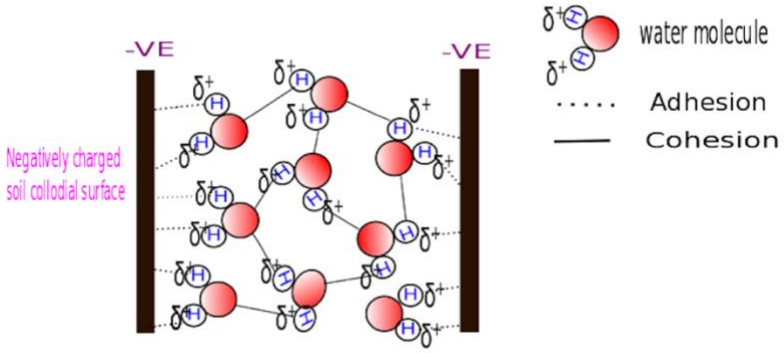

Figure 2-4: Water molecules in smaller pores

The soil matric potential is conceptually equivalent to having negative pressures in the soil pore. Given water in a cylindrical soil pore, there is a downward force F_{down} due to the weight of the water molecules (Equation 2.20).

$$F_{down} = m \cdot g \tag{2.20}$$

The mass, m (kg), of water is the product of its density and volume of the cylindrical pore.

$$m = \rho_w \cdot \pi \cdot r^2 \cdot z \tag{2.21}$$

Therefore F_{down} is

$$F_{down} = \rho_w \cdot \pi \cdot r^2 \cdot z \cdot g \tag{2.22}$$

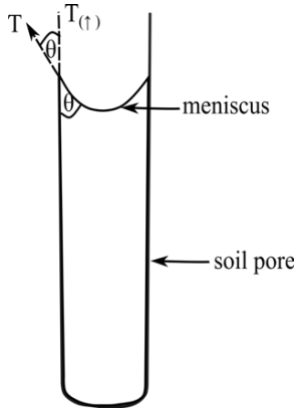

Figure 2-5: Tension generated at the liquid-soil colloid interface in soil pores

There is also an upward force F_{up} due to surface tension, T ($N\ m^{-1}$), generated at the liquid-soil colloid interface (Figure 2-5). The tension has both vertical T_v and horizontal T_h components (Whalley et al., 2013). The vertical component is given as

$$T_v = T cos\theta \tag{2.23}$$

The tension is exerted at the entire circumference of the soil pore $(2 \cdot \pi r)$. The total vertical upward force acting on the water is given as:

$$F_{up} = 2 \cdot \pi \cdot r \cdot T cos\theta \tag{2.24}$$

At equilibrium, the upward and downward forces are equal so

$$F_{down} = -F_{up} \tag{2.25}$$

The negative sign in Equation 2.25 means that the force is acting against gravity. Based on Equation 2.25, equations 2.24 and 2.22 can be equated as:

$$\rho_w \cdot \pi \cdot r^2 \cdot z \cdot g = -2 \cdot \pi \cdot r \cdot T cos\theta \tag{2.26}$$

By dividing both sides of Equation 2.26 by the term $\pi . r^2$, Equation 2.26 can be simplified as

$$\rho_w \cdot z \cdot g = \frac{-2 \cdot T cos\theta}{r} \tag{2.27}$$

Equation 2.27 is the Young–Laplace equation (Whalley et al., 2013). The left-hand side of Equation 2.27 is equal to the matric potential energy per unit volume of water, E_{vm} . Thus, E_{vm} is a function of surface tension, T $(N\ m^{-1})$, pore radius, r (m), and contact angle, θ (degrees) (Whalley et al., 2013). The matric potential energy per unit weight of water, or matric head, ψ_m (m), is given by

$$\psi_m = \frac{-2 \cdot T cos\theta}{\rho_w \cdot g \cdot r} \tag{2.28}$$

Osmotic potential

The presence of solutes also affects the energy status of soil water. The energy possessed by soil water due to its interaction with dissolved salts is called the solute or osmotic potential, ψ_s, (Campbell, 1988; Malaya & Sreedeep, 2012). The osmotic potential energy per unit volume, E_{vs} ($J\ m^{-3}$), is a function of the concentration of solutes in the soil, c ($mol\ m^{-3}$), and the temperature T(K) (Equation 2.29) (Clark, 1990).

$$E_{vs} = -c \cdot R \cdot T \tag{2.29}$$

Where R is the real gas constant (8.314 $J\ mol^{-1}\ K^{-1}$). This can also be expressed as an equivalent head, ψ_s (m), by

$$\psi_s = \frac{-c \cdot R \cdot T}{\rho_w \cdot g} \tag{2.30}$$

The total water potential, ψ_t, of soil water is estimated as the sum of all the potentials (Campbell, 1988; Hohmann, 1997) (Equation 2.31).

$$\psi_t = \psi_z + \psi_m + \psi_p + \psi_s \tag{2.31}$$

In unsaturated porous media, we typically consider hydraulic head as the dominant potential energy term, where

$$\psi_h = \psi_z + \psi_m \tag{2.32}$$

2.2.3 Soil moisture characteristic curve

The soil moisture characteristic curve (SMC) (Wang et al., 2011; Malaya & Sreedeep, 2012), also referred to as the soil water retention curve (SWRC) (Iiyama, 2016; Dey et al., 2017) or moisture release curve, describes the relationship between soil moisture content and matric potential (Wang et al., 2011; Malaya & Sreedeep, 2012; Pham & Fredlund, 2005; Iiyama, 2016; Dey et al., 2017; Qi et al., 2018).

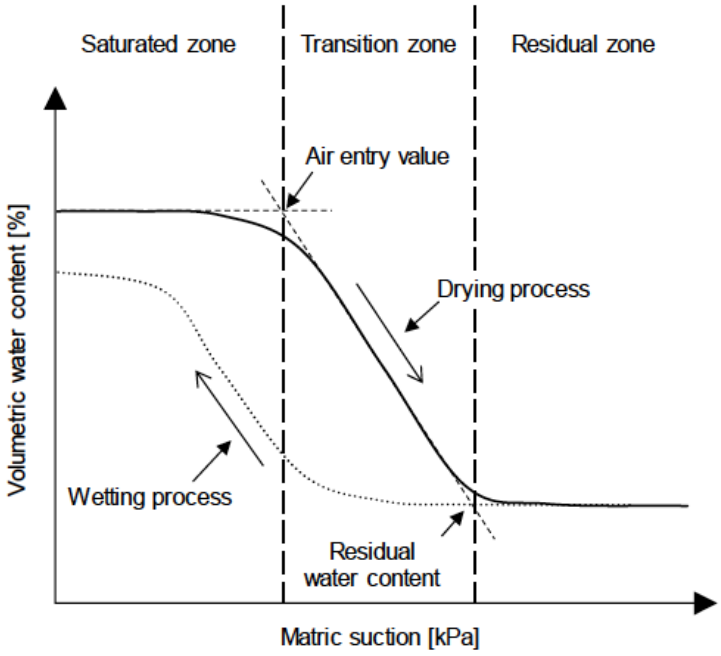

Figure 2-6: Typical SMC curve showing the different zones (after Hong et al., 2016)

The SMC can be divided into three zones namely the saturated zone, transition zone and the residual zone (Figure 2-6) (Vanapalli et al., 1996; Hong et al., 2016). At the saturated zone, most of the soil pores are filled with water, and the soil does not drain until the matric potential exceeds the air entry value (AEV) (Vanapalli et al., 1996). The air entry value is the matric potential value at which air firsts enters the bigger pores as they begin to drain. The transition stage is where there is a rapid decrease in moisture content with increasing matric potential (Vanapalli et al., 1996). The soil drains under suction until it reaches the residual zone where the moisture content stays almost constant with increasing matric potential (Hong et al., 2016).

One fundamental feature of the SMC is that it is hysteretic (Pham & Fredlund, 2005; Dey et al., 2017). Hysteresis is when the drying and wetting cycles of the same soil produce different SMCs (Pham & Fredlund, 2005; Dey et al., 2017). Thus, the drying curve of the same soil holds more moisture than the wetting curve at the same matric potential (Figure 2.6). This phenomenon is attributed to the pore neck effect, air entrapment, the difference in contact angle between soil

particle and soil water, shrink-swell behavior of soils, and ageing (Pham & Fredlund, 2005; Dey et al., 2017).

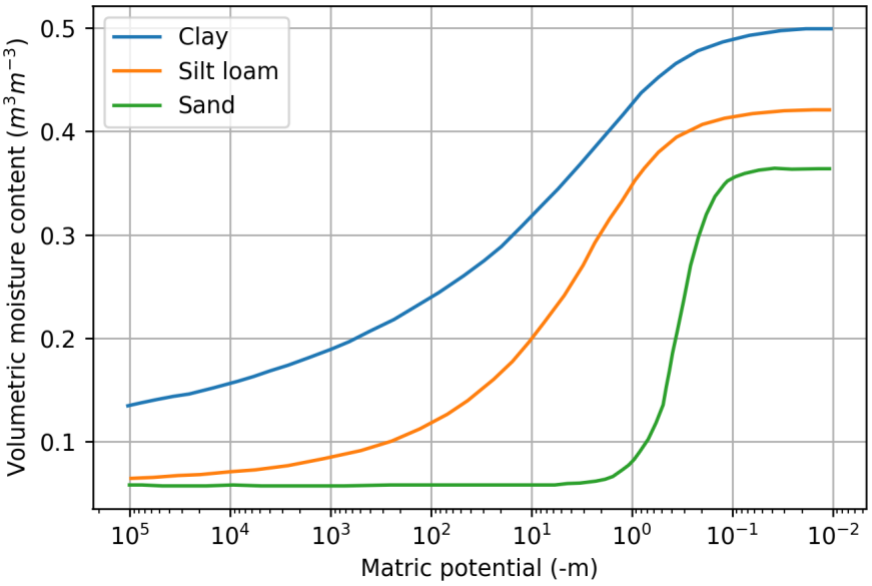

Figure 2-7: The SMC for different soil textures (after Tuller et al., 2004)

The SMC is influenced by soil texture (Qi et al., 2018). At the same matric potential, soils of different textures have different moisture contents (Figure 2-7). Clayey soils have more micro-pores and tend to hold more moisture than silt and sand at the same matric potential. Soil porosity is also a function of bulk density. As such, other determinants of soil bulk density such as compaction and structure may influence the shape of the SMC.

2.3 Physics of Frozen Soils

2.3.1 Freezing and thawing of soils

Freeze-thaw cycles in frozen soils affect most of the physical and mechanical properties of frozen soil (Xie et al., 2015). Research has shown that freezing may decrease infiltration due to the clogging of soil pores with ice (Maulé & Gray, 1994; Christensen et al., 2013; Zhao et al., 2016; Appels et al., 2018). Clogging of soil pores reduces the effective porosity and hydraulic conductivity resulting in decreased infiltration rate (Appels et al., 2018), though some findings suggest infiltration rates in frozen soils are still high due to air filled pores (Mohammed et al., 2018). Other physical properties influenced by freeze-thaw cycles are soil structure, aggregate stability, soil volume and bulk-density (Xie et al., 2015). Freeze-thaw cycles in cold climates are associated with changes in soil temperature (Xie et al., 2015; Zhou et al., 2018) in response to air temperature. As soil temperature drops below 0 ℃, ice forms in the soil pores resulting in a reduction in the volumetric liquid water content (Figure 2-8). On the reverse, as the ground warms up, pore ice begins to melt (Guan et al., 2010) and the volumetric liquid water content increases (Figure 2-8).

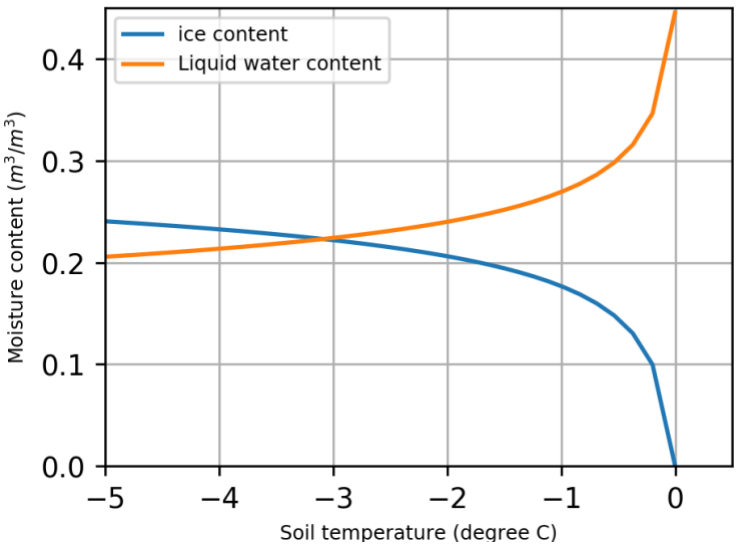

Figure 2-8: Response of soil moisture to soil temperature

2.3.2 Freezing point depression

Freezing is a spontaneous process that occurs to minimize free energy (FE). Ice (i) and liquid water (l) can co-exist only when they have equal free energy, and this occurs at 0 ℃ (T_0, ℃) for bulk water (Zhang & Liu, 2018). Above T_0, liquid water has lower free energy than ice, and therefore liquid water is the stable phase. When the temperature of bulk water drops below T_0 ℃, the free energy of the liquid phase becomes higher than that of the solid phase ($FE_l > FE_i$). This drives the transformation of liquid water into ice, and ice becomes the stable phase. Conversely, in a soil pore, the free energy of liquid water is reduced, so, soil water does not freeze at T_0. For freezing to proceed, the temperature must reduce further to bring the free energy of ice below that of the depressed liquid water (the freezing temperature of the depressed liquid water is denoted as T_f, ℃).

This phenomenon is found to be due to 1) capillarity and adsorption (capillary effect) and 2) salts (salinity effect) (He et al., 2016; Zhang & Liu, 2018). The capillary effect is due to the intermolecular forces of attraction generated between liquid water and the other constituents (soil solids, ice, and air) of partially frozen soil (Figure 2-9). These intermolecular forces of attraction reduce the free energy of liquid water below that of ice resulting in the depression of freezing point. Similarly, the ions of salts block water molecule from coming together close enough to form solids (ice) thereby, depressing the freezing point of the water.

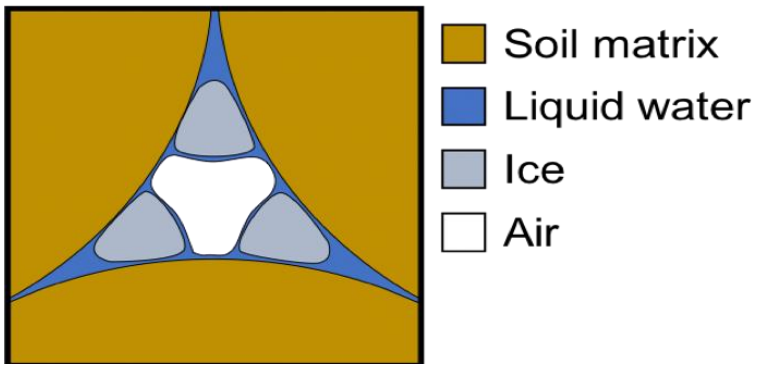

Figure 2-9: Inside a freezing soil, interaction between soil constituents (after Miller, 1980, p. 275)

Secondly, freezing point depression is progressive, which is to say the water in the continuum of different sized soil pore spaces has a distribution of freezing temperatures, and thus freezing occurs progressively as the temperature drops below T_0. In terms of the capillary effect, as the soil freezes, the remaining liquid water is held tightly unto progressively thinner absorbed films and in smaller pores (Spaans, 1994). Hence, the capillary forces and thus the freezing point of the water in an individual pore depends upon the pore size (analogous to matric potential), so smaller pores have lower freezing temperatures (Spaans, 1994). Similarly, during freezing, salts are excluded from ice, making the resulting solution more concentrated. Hence the freezing point of the remaining liquid water decreases further. The relationship between the liquid water content and the freezing temperature in frozen soil is called the soil freezing characteristic curve (SFC).

2.3.3 Soil freezing characteristic curve

The soil freezing characteristic curve (SFC) quantifies the amount of liquid water co-existing with ice in frozen soils as a function of temperature (Flerchinger et al., 2006; Zhou et al., 2014; Watanabe & Osada 2017; Ren & Vanapalli, 2019; Ren & Vanapalli, 2020). The SFC is similar to the SMC in unfrozen soils (Spaans & Baker, 1996; Flerchinger et al., 2006; Koopmans & Miller, 1966) except that here the focus is on ice rather than air in unfrozen soils. This similarity is because freezing and thawing cycles in frozen soils follow the same physical process as drying and wetting in unfrozen soils (Zhang & Liu, 2018). For example, in both freezing and drying, liquid water is removed from the soil and replaced with ice in freezing, or air in drying (Spaans & Baker, 1995; Zhang & Liu, 2018).

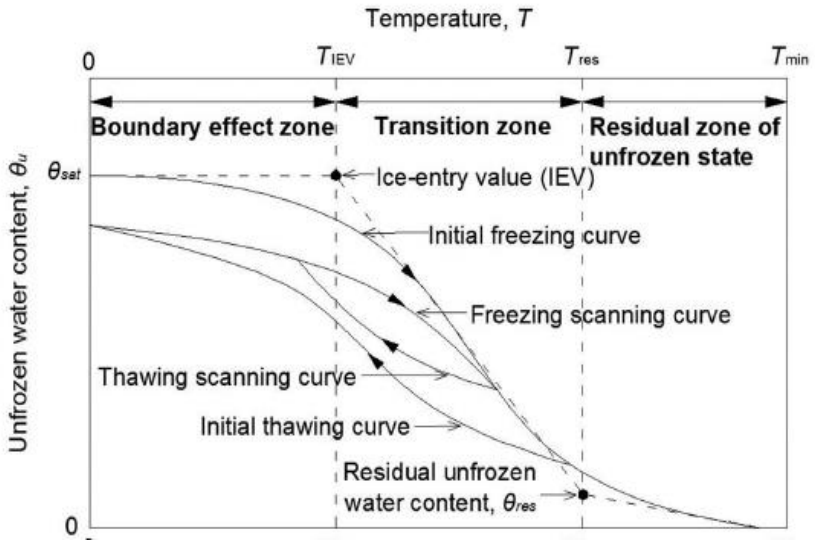

Figure 2-10: Conceptual diagram of the SFC (after Ren & Vanapalli, 2018)

Just like the SMC, the SFC can be divided into three sections, namely the boundary effect zone, the transition zone and the residual zone (Figure 2-10) (Ren & Vanapalli, 2018). At the boundary effect zone, soil water remains as a liquid at subzero temperatures. This is because the freezing point of water is depressed and freezing occurs after the ice entry value (IEV). The ice entry value is the temperature at which ice penetrates the bigger pores (Ren & Vanapalli, 2018). At the transition zone, ice crystals grow in the soil pore resulting in a rapid decrease in the liquid water content (Ren & Vanapalli, 2018). The ice crystals continue to grow in the soil pore until the residual stage where very little to no liquid water freezes (thus liquid water content stays almost constant with decreasing soil temperature) (Ren & Vanapalli, 2018). Also, the SFC is hysteretic, where the freezing curve of the SFC has more liquid water than the thawing curve at the same freezing temperature (Figure 2-10).

2.4 Measurement of the SMC

The SMC is measured either in situ in the field or in the laboratory. The various field and laboratory methods for determining the SMC are described in the sub-sections below.

2.4.1 Measuring the SMC in the field

Quantifying the SMC requires simultaneous measurement of soil moisture content and matric potential. In the field, different techniques are employed in measuring the soil moisture content and matric potential. Examples of field techniques used in measuring moisture content include the use of the Neutron Probe (Elder & Rasmussen, 1994), and the dielectric techniques (including Time and Frequency Domain Refractometers, and the Coaxial Impudence Dielectric Sensor) (Patterson & Smith, 1985; Bitelli et al., 2003; Seyfried & Murdock, 2004; Watanabe et al., 2011; Kelleners & Norto, 2012; Susha Lekshmi et al., 2014; Zhou et al., 2014; Yao et al., 2016; Tian et al., 2017). The description and operation of the dielectric techniques can be found in section 2.5.1 of this thesis. The matric potential is measured using tensiometers (Wallhan, 1939; Schmugge et al., 1980; Ridley & Burland, 1993; Tarantino et al., 2008; Susha Lekshmi et al., 2014; Caicedo, 2017), thermocouple psychrometers (Cresswell et al., 2008; Bittelli, 2010), and porous block sensors (Tarantino et al., 2008). These matric potential measuring instruments are described further in the sections below.

2.4.1.1 Tensiometers

Even though tensiometers can be used in the laboratory, especially in large column experiments, they are more intended for use in the field. Tensiometers were first introduced in the 1900s to measure the tension generated in the root zone of plants (Tarantino et al., 2008). Figure 2-11 is an example of a Jet fill vacuum tensiometer which was introduced in the late 90s (Tarantino et al., 2008). The jet fill vacuum tensiometer is made up of a reserve water tank (for refilling the reservoir and for degassing the water in the reservoir), water reservoir, a ceramic cup and a pressure gauge.

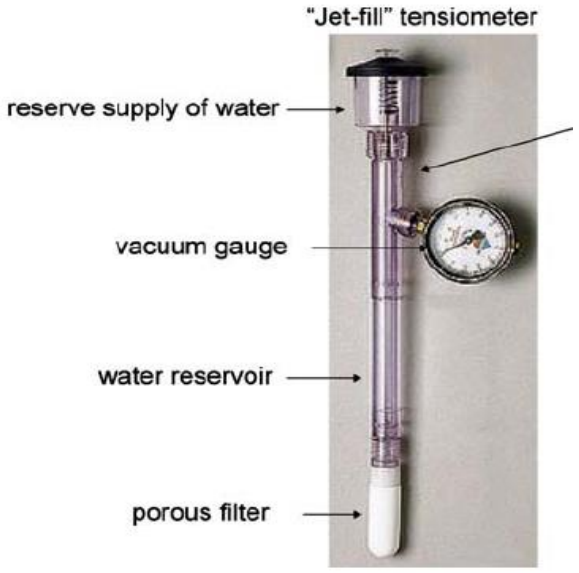

Figure 2.11: Jet fill vacuum tensiometer (taken from Tarantino et al., 2008)

When the tensiometer is inserted into dry soil, water moves from the ceramic cup of the tensiometer into the soil. This generates suction in the tensiometer, which is read by the pressure gauge (Bittelli, 2010). The design of tensiometers has evolved to more sophisticated and high-efficiency ones. For instance, modern tensiometers are equipped with pressure sensors for measuring the matric potential of the soil instead of a gauge in the old types. They also have features that allow for automating the measurement by connecting to a data logger. An example of such modern type tensiometer is the T4e tensiometer from Decagon devices (Figure 2-12). The T4e tensiometer can measure matric potential in the range of +100 to -85 kPa (Bam et al., 2019).

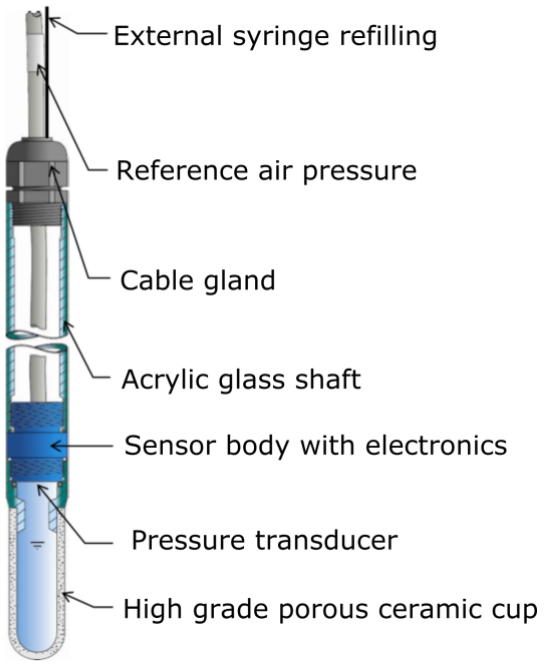

Figure 2-12: Diagram of the T4e pressure transducer tensiometer with its parts labelled (taken from the T4e Manual, UMS, 2011)

2.4.1.2 Thermocouple psychrometer

The thermocouple psychrometer method is a technique for estimating the soil matric potential by measuring the relative humidity of the air in the soil pores (Cresswell et al., 2008). The measured relative humidity is related to the matric potential, ψ_m (MPa) through Equation 2.33 (Cresswell et al., 2008), assuming that there is no salt in the soil.

$$\psi_m = \frac{R \cdot T}{M}(\ln h_r) \tag{2.33}$$

Where R is the real gas constant, T is temperature (K), M is the molecular weight of water, and h_r ($MPa\ K^{-1}$) is the relative humidity of the water vapor in equilibrium with the soil (Cresswell et al., 2008). This method is not suitable in soils with moisture contents close to saturation. Other

limitations of the thermocouple psychrometer are that it needs constant cleaning and calibration before use and that it is only suitable for small volumes of soil (Bittelli, 2010).

2.4.1.3 Porous block sensors

Porous block sensors are indirect methods for measuring soil matric potential. They are considered so because the sensors measure a known property of the block (thermal conductivity or electrical conductivity) which is then converted to matric potential through a calibration equation. For example, thermal conductivity sensors measure the changes in thermal conductivity of a porous block in response to changes in the moisture content of the block. When inserted into wet soil, water moves from the soil into the porous block, increasing the moisture content of the block. The rise in the moisture content of the porous block is measured as the rise in the thermal conductivity of the block (Bulut & Leong, 2008). The thermal conductivity of the porous block is measured by heating the block with a heater embedded in the block. The temperature rise associated with heating the block is measured and used as an index for calculating the matric potential of the soil (Bulut & Leong, 2008). One popular commercially designed thermal conductivity sensor is the Campbell Scientific 229 heat dissipation matric water potential sensor (Figure 2-13). The Campbell Scientific 229 heat dissipation matric water potential sensor has an operating range of -10 to -2500 kPa (Bam et al., 2019).

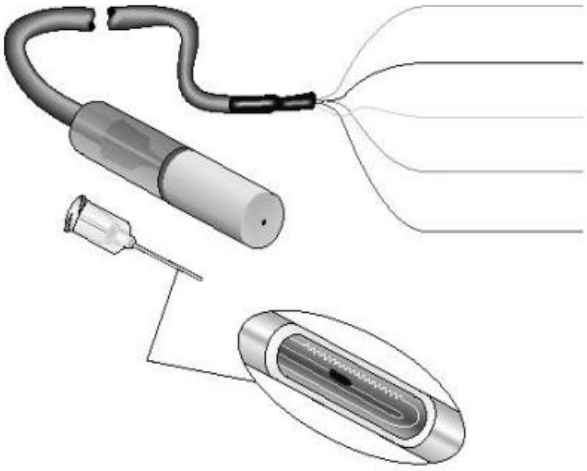

Figure 2-13: The Campbell Scientific 229 heat dissipator porous block sensor (taken from the 229 Manual, Campbell Scientific, 2009)

The electrical conductivity sensor measures the electrical conductivity of the block (Tarantino et al., 2008). The measured electrical conductivity values are then converted to matric potential value through a calibration equation. The calibration equation, however, needs to account for the salinity of the soil because salts affect the electrical conductivity of the porous block (Tarantino et al., 2008).

2.4.2 Laboratory measurement of the SMC

In the laboratory, the SMC is usually measured using the hanging column, pressure plates, hydraulic property analyzer (HYPROP), and the filter paper method. These techniques are described in detail in the sections below.

2.4.2.1 Hanging column

The hanging column (Figure 2-14) is a technique for measuring the SMC (soil moisture content-matric potential pairs).

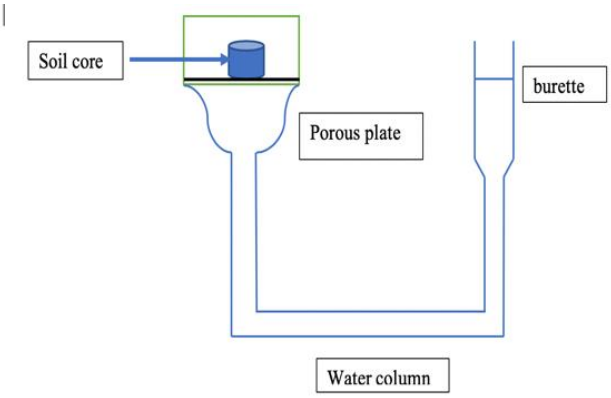

Figure 2-14: Hanging column set-up

In this technique, a metallic core containing saturated soil sample is placed in contact with a porous ceramic plate (Bittelli, 2010), which is connected to a water reservoir. The water reservoir is lowered at different heights (Bittelli, 2010) corresponding to the matric potential of the soil. Doing so creates a head gradient between the soil and the reservoir. The head gradient generates a flow of water from the soil into the water reservoir. The rise in the water level of the reservoir is measured and recorded. This procedure is repeated for different matric potential values. After the experiment, the moisture content of the soil is determined by gravimetric analysis. The soil moisture contents corresponding to the different heights (matric potential) is calculated by adding back the respective water volumes drawn out of the soil. The limitation of this method is that it can only work in wet conditions, usually up to a matric potential of -100 cm.

2.4.2.2 The pressure plate apparatus

The pressure plate apparatus (Figure 2.15) consists of a metal chamber, a ceramic plate for holding soil cores, and a system for applying pressure to the chamber (Richards & Fireman, 1943). The pressure plate can measure the SMC of only intact soil cores. If the sample is disturbed, then it must first be packed into sampling rings before measuring the SMC.

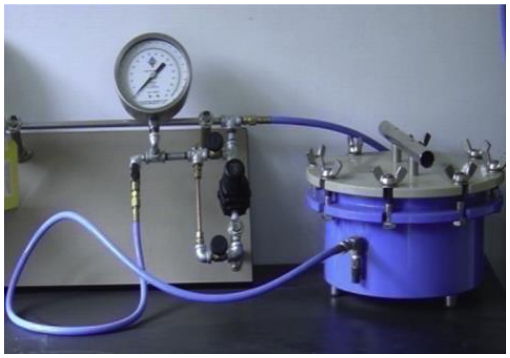

Figure 2.15: Pressure plate apparatus (after Wang et al., 2015)

First, the soil cores are placed in holes on the ceramic plate and saturated by immersing the entire ceramic plate in distilled water. This can take several hours depending on the porosity of the ceramic plate and the soil type. The ceramic plates holding the soil samples are then placed inside the metal chamber, and the chamber is closed tightly. Then, the pressure system is opened to generate specific pressures in the chamber. The pressure causes water to squeeze out of the soil cores into burettes connected to the chamber. After there is no more water draining from the soil under a particular applied pressure (equilibrium established), the volume of water collected in the burettes are measured and recorded. After the final pressure is applied, the cores are removed, oven-dried and their gravimetric moisture content determined. The soil moisture contents corresponding to the pressures applied is determined by adding back the respective water volumes drawn out of the soil. The working range of the pressure plate is -10 to -1,500 kPa (Braudeau et al., 2014; Wang et al., 2015).

2.4.2.3 The hydraulic property analyzer

The hydraulic property analyzer (HYPROP) (Figure 2-16) is an automated system that measures the SMC of a soil sample as it progressively dries by evaporation. The HYPROP can measure moisture content and matric potential simultaneously. The HYPROP has two vertically offset tensiometers, tension top and tension bottom (Breitmeyer & Fissel, 2017). These tensiometers are equipped with pressure transducers for measuring the matric potential of the soil. The matric potential measurements for the two tensiometers are averaged using equation 2.34 below (HYPROP manual version 1.0, 2011).

$$\psi_m = \frac{1}{4}\left({\psi_{m1}}^{i-1} + {\psi_{m2}}^{i-1} + {\psi_{m1}}^{i} + {\psi_{m2}}^{i}\right) \tag{2.34}$$

Where ψ_m is the average matric potential between the two tensiometers, ψ_{m1} is the matric potential measured by tension top, ψ_{m2} is the matric potential measured by tension bottom, and i is the time step for the measurements. The tensiometers have a measurement accuracy of about ±0.015 m (Breitmeyer & Fissel, 2017). The Hyprop is also equipped with a mass balance for measuring the changes in moisture content during evaporation (with an accuracy of ±0.001 g) (Breitmeyer & Fissel, 2017).

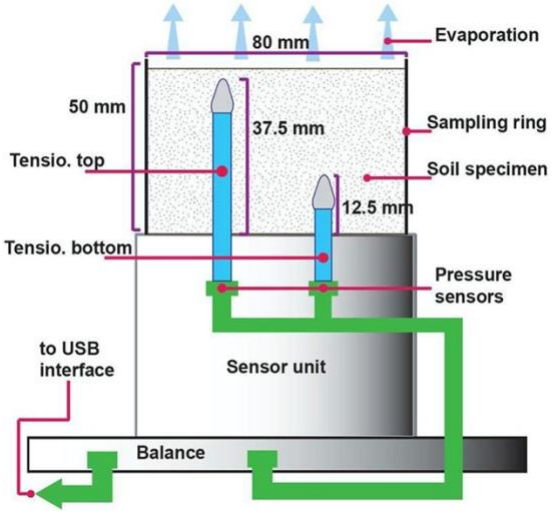

Figure 2-16: Schematic diagram of the HYPROP (after Breitmeyer & Fissel, 2017)

To measure the SMC, first, a soil sample is packed into the sampling ring and saturated by placing the sampling ring in de-aired distilled water. This allows water to rise through the soil by capillarity (Breitmeyer & Fissel, 2017). At the same time, the tensiometers are saturated under pressure and left over-night. Following this, holes are bored into the soil and the tensiometers inserted into the soil sample. After this, the sampling ring is placed on the sensor unit. The sample is then allowed to evaporate by leaving the top of the sample open to the atmosphere. Measurements of moisture content and matric potential are automated by connecting a computer to the sensor unit through a USB port.

2.4.2.4 Filter paper method

In this method, a dry filter paper is placed on a mass balance to determine its dry mass. After that, the filter paper is placed on top of a metallic core containing repacked or intact soil sample (Figure 2-17). The Whatman No. 42 and the Schleicher and Schuell No. 589 filter papers are commonly used in this method (Almeida et al., 2015). After ensuring proper contact between the filter paper and soil, the core sample is covered with PVC plastic or aluminium foil (Almeida et al., 2015) and stored in a glass jar until suction equilibrium is established between the filter paper and the soil (Almeida et al., 2015). After attaining equilibrium, the filter paper is removed and reweighed to determine its wet mass. The moisture content of the filter paper is calculated as the relative mass of water retained in the filter paper (wet mass − dry mass) relative to the dry mass of the filter paper. The matric potential corresponding to the different moisture contents of the soil is determined using Equation 2.35 (Almeida et al., 2015).

$$\psi_m = 10^{\{(6.05-2.48\log(u)\}} \text{ for } u > 47\% \qquad (2.35)$$
$$\psi_m = 10^{\{(4.84-0.0622\log(u)\}} \text{ for } u \leq 47\%$$

Where u (%) is the moisture content of the filter paper. Also, the soil sample is placed in an oven at 105 ℃ for 24 hours. After 24 hours, the soil is removed and allowed to cool in a desiccator and weighed to determine its dry mass. The moisture content of the soil is then determined using Equation 2.1 or 2.2. The accuracy of this method depends highly on the accuracy of the calibration equation used as well as having proper contact between the filter paper and the soil sample.

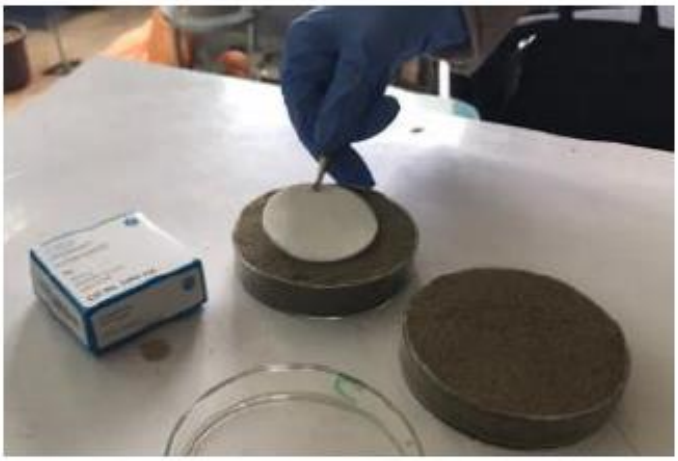

Figure 2-17: The filter paper method (after Pekrioglu Balkis, 2019)

2.5 Measurement of the SFC

There are two main approaches to quantifying the SFC, including 1) direct observation in the field or laboratory, and 2) indirect methods of modelling (Ren & Vanapalli, 2020).

2.5.1 Direct measurement of the SFC

Direct measurement of the SFC requires different instruments and techniques for simultaneous measurement of liquid water content and soil temperature. Discussed in this section are some of the common field and laboratory instruments and techniques employed in measuring the liquid water content and soil freezing temperature.

Techniques employed in measuring liquid water content of field and laboratory soils include the use of dielectric sensors (Time Domain Reflectometry (TDR), Frequency Domain Reflectometry (FDR), and the Coaxial Impedance Dielectric Reflectometry) (Patterson & Smith, 1985; Bitelli et al., 2003; Watanabe et al., 2011; Susha Lekshmi et al., 2014; Zhou et al., 2014; Yao et al., 2016; Tian et al., 2017; Seyfried & Murdock, 2004; Kelleners & Norto, 2012; Francisca & Montoro, 2012), gas dilatometer (Spaans & Baker, 1995), and the Neutron Magnetic Resonance technique

(NMR) (Tice et al., 1982; Yoshikawa & Overduin, 2005; Watanabe & Wake, 2009; Tian et al., 2018; Kong et al., 2020). These instruments have their strengths and limitations, especially in different soils. However, in recent times, the dielectric methods are mostly used because: 1) they are easy to operate; 2) they are less expensive as compared to other techniques and; 3) some of them can measure both the liquid water content and soil temperature. The dielectric methods are discussed in section 2.5.1.1.

The freezing temperature of the soil is determined with temperature probes: thermistors, thermocouples and thermometers. For example, Spaans & Baker (1996) measured the sub-zero temperature of a field soil using a thermistor (Campbell Scientific Model AM32 Logan, UT). Similarly, in a laboratory experiment, Bitelli et al. (2003) measured the freezing temperature of soil using the NTC thermistors model T101D03-DA (CornerStine Sensors, Inc., Vista). Ren & Vanapalli (2020), measured the freezing temperature of soils using RT-1 temperature sensors. Watanabe et al. (2011) inserted thirty-four constantan thermocouples into a soil column to measure freezing temperature. Cheng et al. (2014) measured the temperature of layered and homogenous field profiles with 20 temperature sensors, model DS18B20 (from Dallas semiconductor). Zhou et al. (2014) employed 9 PT100 temperature sensors (platinum resistance temperature detector) in measuring the sub-zero temperature in a soil column. Azmatch et al. (2012) measured freezing temperature using two resistance temperature probes. Lastly, Kelleners & Norto (2012) and Wu et al. (2018) measured temperature of seasonally frozen soils in the field using a dielectric HydraProbe. These are but a few of the various sensors used in measuring freezing temperature in field and laboratory experiments.

2.5.1.1 Dielectric technique of soil moisture determination

The dielectric soil moisture determination technique consists of the Time Domain Reflectometry (TDR), the Frequency Domain Reflectometry (FDR) and the Coaxial Impedance Dielectric Reflectometry Sensor. The dielectric sensors can be used to measure the liquid water content of both unfrozen and frozen soil. This technique exploits the vast difference in the dielectric constant of dry soil (= 2-5), pure water (= 81) (Susha Lekshmi et al., 2014), air (~ 1), and ice (~ 3) (West et al., 2007). Thus, the bulk dielectric constant of the soil is largely due to water. The sensors

measure the bulk dielectric constant, ε_b of the soil. The measured bulk dielectric constant is then used to estimate the liquid water content. In unfrozen soils, the liquid water content can be estimated from the measured bulk dielectric constant using a physically based dielectric mixing model (Equation 2.36) (Roth et al., 1990) or the empirically based Topp equation (Equation 2.37) (Topp et al., 1980; Susha Lekshmi et al., 2014; LeBlanc, 2017).

$$\varepsilon_b = \left[\varepsilon_L^{\beta} \cdot \theta_L + (1-\phi)\varepsilon_s^{\beta} + (\phi - \theta_L)\varepsilon_a^{\beta}\right]^{\frac{1}{\beta}} \tag{2.36}$$

$$\theta_L = 4.3 * 10^{-6}(\varepsilon_b)^3 - 5.5 * 10^{-4}(\varepsilon_b)^2 + 2.29 * 10^{-2}(\varepsilon_b) - 5.3 * 10^{-2} \tag{2.37}$$

Where θ_L ($m^3\ m^{-3}$) is the volumetric liquid water content, ϕ is soil porosity, ε_s, ε_w, ε_a are the dielectric constants of soil solids, water, and air, respectively. β is an exponent that varies from 1 to -1 depending on the structure and composition of the soil. In partially frozen soils, however, the Topp's model fails because it cannot account for ice (Tian et al., 2017). Hence, the dielectric mixing model for frozen soils (Equation 2.38) (Kelleners & Norto, 2012) is preferred.

$$\varepsilon_b = \left[\varepsilon_L^{\beta} \cdot \theta_L + \varepsilon_I^{\beta} \cdot \theta_I + (1-\phi)\varepsilon_s^{\beta} + (\phi - \theta_L - \theta_I)\varepsilon_a^{\beta}\right]^{\frac{1}{\beta}} \tag{2.38}$$

Where θ_I ($m^3\ m^{-3}$) is the volumetric ice content, and ε_I is the dielectric constant of ice.

The Time Domain Reflectometry method measures the bulk dielectric constant of soil using the difference in the incidence and reflected times of electromagnetic pulse (Susha Lekshmi et al., 2014) as in Equation 2.39.

$$\varepsilon_b = \left(\frac{C \cdot t}{2L}\right)^2 \tag{2.39}$$

Where C is the velocity of light in space ($3.0 \times 10^8\, m\, s^{-1}$), t is the transit time for the electromagnetic pulse, and L is the length of the probe.

The Frequency Domain Reflectometry (FDR) works on the same principle as the TDR, the only difference is that the FDR relates the dielectric constant of the soil to the frequency of electrometric pulses propagated through the soil (Yao et al., 2016; Susha Lekshmi et al., 2014). Just like the TDR, the FDR sends an electromagnetic pulse through the soil, and this is refracted back to the output terminal. The difference between the frequencies of the input and output electromagnetic waves is measured. This is then used as a measure of the dielectric constant of the soil.

The Coaxial Impedance Dielectric Reflectometry Sensor (Seyfried & Murdock, 2004; Kelleners & Norto, 2012; Francisca & Montoro, 2012) propagates electromagnetic waves through the soil through its metallic tines (Francisca & Montoro, 2012). Part of the electromagnetic wave is reflected to the sensor. The sensor measures the impendence of the reflected signal, which is related to the bulk dielectric constant of the soil (Francisca & Montoro, 2012). The Stevens HydraProbe (manufactured by the Stevens Water Monitoring System Inc.) is an example of commercially available Coaxial Impedance Dielectric Reflectometry Sensor. The HydraProbe (Figure 2-18) is less expensive compared to the other dielectric methods and can measure both the real and apparent (imaginary) dielectric constants of the soil (Seyfried & Murdock, 2004). The HydraProbe is made up of a cable, sensor unit and the tines. The probe is about 12.4 cm in length and has a diameter of about 4.2 cm and with tines of length 4.5 cm (Hydra II, Stevens Water Monitoring Systems Inc., 2007, User's Manual). The device also has a temperature sensor embedded in it, which measures the temperature of the soil (Francisca & Montoro, 2012). Apart from temperature and moisture content measurements, the Stevens HydraProbe can also be used to measure the electrical conductivity of the soil. The HydraProbe can measure moisture content with an accuracy of 0.01-0.03 $m^3\ m^{-3}$ depending on the soil type (Hydra II, Stevens Water Monitoring Systems Inc., 2007, User's Manual).

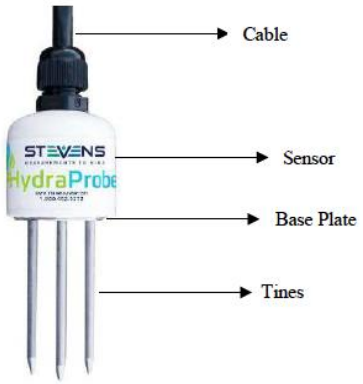

Figure 2-18: Stevens HydraProbe sensor (taken from Hydra II, Stevens Water Monitoring Systems Inc., 2007, User's Manual)

2.5.1.2 Laboratory column experiments

In situ measurement of the SFC is challenging because there is limited control over soil properties (bulk density, moisture content, soil temperature, salinity), weather conditions (humidity, rainfall, winter), and interference from animals and humans. These factors impede the progress of field experiments and introduce numerous errors in the experiments. Laboratory column experiments, however, give researchers control over these factors and helps to minimize errors in the experiments.

In this study, a soil column is defined as a small compact unit of soil in an impermeable container that allows for controlled measurement of the SFC (Lewis & Sjöstrom, 2010). Soil columns are usually constructed from PVC pipes (Kreba & Maule, 2010) or plexiglass cylinders (Stähli & Stadler, 1997; Zhou et al., 2014). Example of studies that measured the SFC of soil using a laboratory soil column includes those of Zhou et al. (2014), Holten et al. (2018), Watanabe et al. (2011), Stähli & Stadler (1997), Bing & Ma (2011), Nagare et al. (2011), and Watanabe & Osada (2017).

In most of these experiments, the SFC is measured by packing disturbed soil samples into the columns and taking simultaneous measurements of liquid water content and freezing temperature.

Two main soil packing techniques are employed in literature; these are dry packing (Oliviera et al., 1996; Lewis & Sjöstrom, 2010) and wet packing. In dry packing, the mass of soil to occupy a specific volume is calculated from the dry bulk density of the soil. The soil is then re-packed gradually to fill that entire volume (Lewis & Sjöstrom, 2010). Oliviera et al. (1996) observed that adding soil in layers of 2 cm, followed by compaction with a metal pestle produced a more homogenous column. If the soil is packed dry, the moisture content of the soil is controlled by means of a water pump connected to the base of the column (Figure 2-19) or by ponding water on the surface of the soil. In wet packing, however, the soil sample is first mixed with water to achieve the desire moisture content before packing into the column (Zhou et al., 2014; Watanabe et al., 2011).

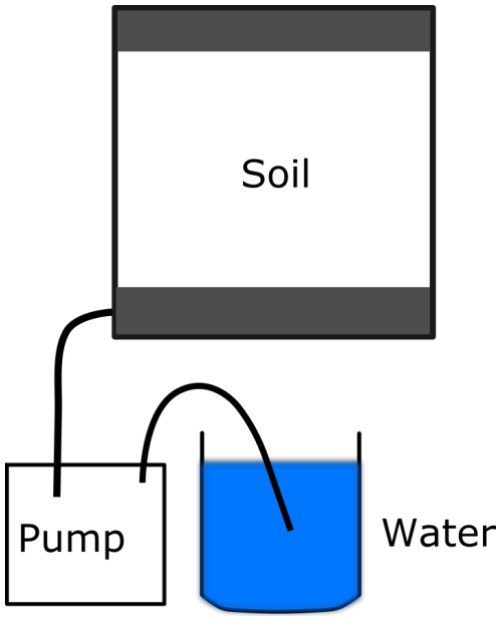

Figure 2.19: Schematic diagram showing how water is applied to a soil column through a water pump connected to the bottom of the column (after Watanabe & Osada, 2017)

The instruments for measuring the SFC are either inserted vertically into the soil (Teixeira et al., 2003; Peng et al., 2019) and the soil packed around them or horizontally through holes made at the sides of the columns (Stähli & Stadler, 1997; Teixeira et al., 2003; Watanabe et al., 2011; Nagare et al., 2011; Zhou et al., 2014; Holten et al., 2018). After packing the soil, the soil is frozen by

placing the column in a temperature-controlled bath (Bing & Ma, 2011; Watanabe & Mizoguchi, 2002) or in a refrigerator (Watanabe & Osada, 2017; Holten et al., 2018). Other means of controlling the temperature of the soil column is by bringing one end of the soil column in contact with a cold plate (Nagare et al., 2011). In most experiments where the column is placed in a refrigerator, the column is first insulated with a rubber sheet or glass wool (Stähli & Stadler, 1997; Watanabe et al., 2011; Watanabe & Osada, 2017; Holten et al., 2018). This is to ensure only vertical temperature propagation through the soil (Holten et al., 2018).

2.5.2 Theoretical or indirect measurement of the SFC

Direct measurement of the SFC is ideal as it reflects the complexities in nature. However, this approach is extremely challenging, time-consuming and requires sophisticated equipment which can be expensive. As such, the SFC has been modeled from the SMC in unfrozen soils (Zhang & Liu, 2018). The widely used generalized Clapeyron equation (GCE) (Zhang & Liu, 2018; Mohammed et al., 2018; Teng, 2020) assumes that in frozen conditions the temperature predicts an equivalent effective soil matric potential. Based on this assumption, the GCE has been employed extensively in literature for establishing the SFC. This is done by combining the GCE relationship with moisture characteristic models to find a relationship between liquid water content and temperature. For example, Zhou et al. (2018) and Zhang et al. (2016) modelled the SFC by combining the GCE with the Brooks and Corey (1964) and van Genuchten (1980) moisture characteristic models, respectively. The van Genuchten model (Equation 2.40) is widely used.

$$\theta_L = \theta_r + \frac{\theta_s - \theta_r}{(1 + |\alpha \cdot \psi_m|^n)^{-m}} \tag{2.40}$$

Where θ_L $(m^3\ m^{-3})$ is the volumetric liquid water content, $\theta_r (m^3\ m^{-3})$ is the residual moisture content, and $\theta_s (m^3\ m^{-3})$ is the saturated moisture content or porosity, $\psi_m (m)$ is the matric potential, α (m^{-1}) is approximately the inverse of the air entry value, n and m are dimensionless empirical shape-defining parameters (van Genuchten, 1980; Kelleners and Norto, 2012). This approach has presented a great opportunity for scientist to study moisture dynamics in frozen soils without having to deal with complicated, expensive and time-consuming field and laboratory

experiments. However, the approach does not account for the effects of salts on the SFC (Azmatch et al., 2012). Kurylyk & Watanabe (2013) reviewed the different forms of the GCE and concluded that all the GCE derivations ignore the salinity effect component of freezing point depression. This omission might limit the application of the GCE in real soil and may lead to underestimation of the liquid water content. For instance, earlier work by Koopmans & Miller (1966) on the SFC stated that real soils contain unavoidable impurities and the authors suggested that the effect of such impurities must be accounted for. Similar studies by Watanabe & Mizoguchi (2002) also emphasized that the effects of salts on the amount of liquid water in frozen soils are not well understood and that this effect is needed to adequately predict the behavior and amount of liquid water in partially frozen soils.

Secondly, there is limited published work that shows how well this theoretical relationship (GCE) fits with real observations of the SFC. One study that tries to do so is that of Spaans & Baker (1996). In this study, the authors measured the freezing temperature of a clayey soil using a thermistor, and the liquid water content using a TDR. The resulting SFC was converted to an equivalent SMC by converting the temperature value to matric potential using a modified form of the GCE, as shown in Equations 2.41 and 2.42. The GCE is modified to account for "osmotic potential", which the authors conclude is important at temperatures just below 0 ℃, and the temperature dependence of the latent heat of fusion. The authors compared the results with observed SMCs for the same soil measured using a combination of methods including a hanging column, a Tempe cell, and a pressure plate showing a good agreement between the SFC and SMC (Figure 2-20). However, the authors did not provide information on the measured electrical conductivities (σ_{sp}) and the temperature values for the SFC, making it impossible to replicate the study.

$$\psi_L = -712.38\ \ln(T/T_o) + 5.545\ (T - T_o) - 3.14 \times\ 10^{-3}\left(T^2 - {T_o}^2\right) - \prod_L \qquad (2.41)$$

$$\prod_L = \ -39\sigma_{sp}(W_{sp} \cdot \rho_b)/(\theta_L \cdot {\rho_L}^2)(T/298) \qquad (2.42)$$

Where T is soil temperature, $\prod_L$ ($kJ\ kg^{-1}$) is the osmotic potential, σ_{sp} ($mS\ cm^{-1}$) is the electrical conductivity of saturated paste extract, and W_{sp} ($kg\ kg^{-1}$) is the wetness of the sample.

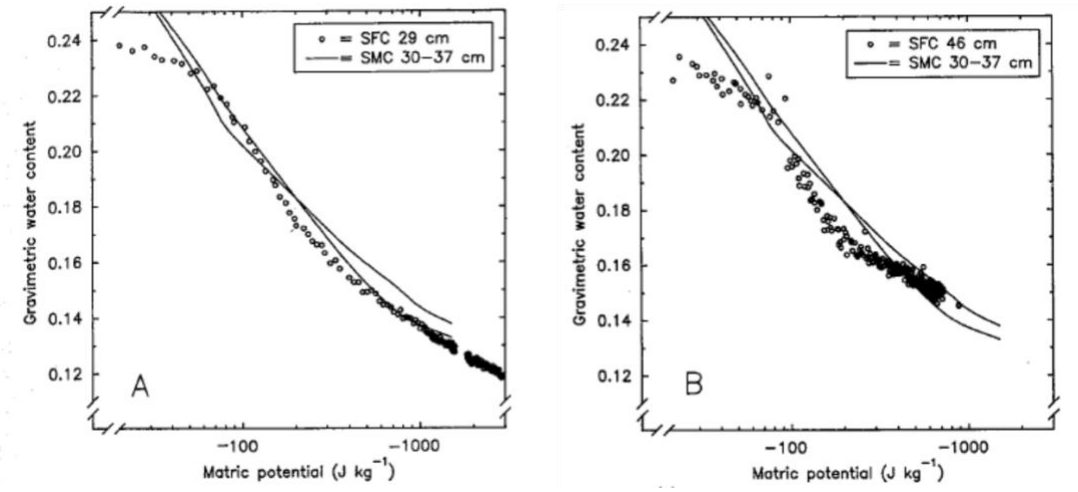

Figure 2-20: Figures showing the similarities between the observed SMCs and SFCs modelled using the GCE (after Spaans & Baker,1996)

The above research gaps have necessitated further study to understand the effect of salts on the SFC properly and to show how the GCE and other alternative models compare with observations from the laboratory and different field sites.

2.5.2.1 Derivation of the Generalized Clapeyron equation (GCE)

The GCE is a thermodynamic model that describes the equilibrium relationship between freezing temperature and pressure in frozen soils (Kurylyk & Watanabe, 2013; Teng, 2020). It stems from the Gibbs-Duhem's free energy concept of phase change (Hayashi, 2013; Kurylyk & Watanabe, 2013) which is represented by Equation 2.43.

$$dG = VdP - SdT \tag{2.43}$$

Where G ($J\ kg^{-1}$) is the Gibbs free energy, V ($m^3\ kg^{-1}$) is the specific volume, S ($J\ K^{-1}\ kg^{-1}$) is entropy, and T is soil temperature (K). Equation 2.43 can be written for the ice (I) and liquid (L) phases in a frozen soil as in Equation 2.44 and Equation 2.45, respectively.

$$dG_I = V_I dP_I - S_I dT \tag{2.44}$$

$$dG_L = V_L dP_L - S_L dT \tag{2.45}$$

At the freezing point, $dG_i = dG_l$ (Williams & Smith, 1989, p 5). Hence Equation 2.44 and 2.45 can be equated as:

$$V_I dP_I - S_I dT = V_L dP_L - S_L dT \tag{2.46}$$

Grouping like terms in Equation 2.46 gives Equation 2.47.

$$S_L dT - S_I dT = V_L dP_L - V_I dP_I \tag{2.47}$$

Equation 2.47 can be re-arranged as:

$$(S_L - S_I)dT = V_L dP_L - V_I dP_I \tag{2.48}$$

The change in entropy between the two phases is a function of temperature and latent heat of fusion, $L_f, J\ kg^{-1}$ (Equation 2.49) (Williams & Smith, 1989, p. 190).

$$dS = \frac{L_f}{T} \tag{2.49}$$

Equation 2.49 can, therefore, be substituted into Equation 2.48 as:

$$\frac{L_f}{T} dT = V_L dP_L - V_I dP_I \tag{2.50}$$

Assuming the pressure of the ice phase is constant ($dP_I = 0$). Equation 2.50 is then reduced to

$$\frac{L_f}{T} dT = V_L dP_L \tag{2.51}$$

Equation 2.51 can be simplified further to give Equation 2.52 below.

$$\frac{dP_L}{dT} = \frac{L_f}{T \cdot V_L} \tag{2.52}$$

Assuming that at atmospheric pressure, P_0= 0, then Equation 2.52 can be solved for pressure as:

$$P_L = \frac{L_f}{V_L} \ln\left(\frac{T}{T_f}\right) \tag{2.53}$$

Where T_f (K) is freezing temperature of soil water under a specific set of conditions. Dividing both sides of equation 2.53 by $\rho_L . g$ gives us

$$\frac{P_L}{\rho_L \cdot g} = \frac{L_f}{V_L \cdot \rho_L \cdot g} \ln\left(\frac{T}{T_f}\right) \tag{2.54}$$

The left-hand side of the Equation 2.54 is the same as ψ. But V_L is specific volume, $\frac{v_L}{M_L}$,which is the same as the inverse of the density of water. So, Equation 2.54 becomes

$$\psi = \frac{L_f \cdot \rho_L}{\rho_L \cdot g} \ln\left(\frac{T}{T_f}\right) \tag{2.55}$$

Equation 2.55 can be simplified further to

$$\psi = \frac{L_f}{g} \ln\left(\frac{T}{T_f}\right) \tag{2.56}$$

Equation 2.56 represents the Generalized Clapeyron equation (GCE) which is fundamental to studying freezing point depressions in frozen soils.

2.6 Summary

Freezing point depression is quantified at the soil continuum scale through the freezing characteristics curve (SFC). The ideal way of measuring the SFC is by measuring moisture content and soil temperature simultaneously in the field or laboratory using various soil moisture and temperature probes. However, this approach is extremely challenging, expensive and time consuming. As such scientists have modelled the SFC using the GCE with parameters from the SMC in unfrozen soils. Meanwhile, the effects of salts are not accounted for explicitly. Further, there is limited published work that shows how well the GCE compares with observed relationships in the field and laboratory. These gaps have set the stage for this current study. In Chapter 3, experiments are designed to obtain both laboratory and field data that quantifies the SMC and SFC for different soil textures and salinities and to compare the results with those obtained from the GCE and other alternative relationships.

CHAPTER 3

MATERIALS AND METHODS

This part of the thesis is to discuss the materials and methods used in this study. The section is organized into 3 main sections including 1) Laboratory experiments 2) Field experiments and 3) Modelling.

3.1 Laboratory experiments

The objective of the laboratory experiments was to study the SMC and SFC of silica sand under controlled conditions. Silica sand was used with de-ionized water to give very low dissolved solutes in the pore water. The silica sand used was a fine-medium standard graded sand (ASTM C778 graded sand from Ottawa, Illinois Region, United States) with particle size ranging from 0.01 mm to 1 mm. The particle size was determined using the mechanical shaking method (Yan et al., 2017; Pekrioglu Balkis, 2019) with a set of sieves. The results for the particle size analysis is shown in Figure 3-1. Other physical properties of the sand, including particle density, dry bulk density, and porosity are summarized in Table 3-1. Particle density was measured using the pycnometer method as described by Pires et al. (2015), and the soil porosity was determined as the saturated volumetric moisture content of the soil. In both methods, adequate soil packing was achieved by carefully beating the sides of the soil container with a wooden meter rule until there was no change in the level of the sand in the container. If the level of the sand dropped, more soil was added and the beating repeated. The bulk density of the soil was computed from the measured particle density and porosity.

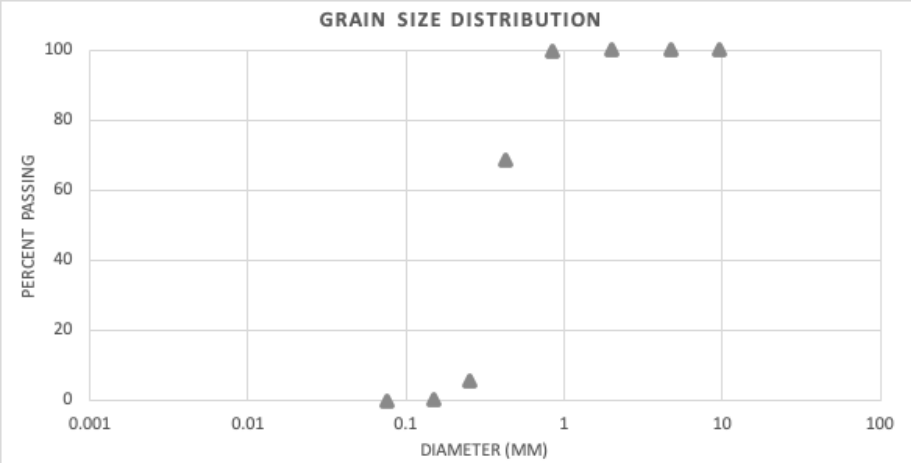

Figure 3-1: Grain size distribution for the silica sand

Table 3-1: Physical properties of the silica sand

Soil property	value	Method
Particle density (ρ_s)	2.5 $g\ cm^{-3}$	Pycnometer method
Porosity (η)	0.42	$\eta = \frac{V_f}{V_t}$
Bulk density (ρ_b)	1.45 $g\ cm^{-3}$	$\rho_b = (1-\eta)\cdot\rho_s$

Where V_f is the volume occupied by fluid and V_t is the total volume of the soil.

3.1.1 Soil moisture characteristic curve

The soil moisture characteristic curve (SMC) of the sand was measured using the HYPROP set-up (Figure 3-2) (UMS GmBH in Munich, Germany). A detailed description of the HYPROP and its operation can be found in chapter 2.4.2.3 of this thesis. The sand was repacked into the sampling ring of the HYPROP using the same packing techniques as described in section 3.1 above. The measured bulk density of the repacked soil was 1.55 $g\ cm^{-3}$, which is higher than the actual bulk density of the sand (Table 3-1). This may be due to overpacking of the soil sample. Following soil packing, the sample was saturated by placing the sampling ring in a bowl of de-aired distilled water for 24 hours. After 24 hours, the sampling ring was removed from the bowl and placed on top of the sensor unit of the equipment. The soil was then allowed to dry by evaporation. Soil moisture content and matric potential were measured simultaneously by the HYPROP using a mass balance and two vertically offset tensiometers, respectively. The entire set-up was connected to a computer to log the soil moisture and matric potential measurements.

Figure 3-2: Laboratory set-up for measuring the SMC of the silica sand using the HYPROP equipment

3.1.2 Soil freezing characteristic curves

The freezing characteristic curve (SFC) of the silica sand was measured using two soil columns (Seth 1 and Seth 2) each with dimensions 20 cm (diameter) × 40 cm (height). Seth 2 was used as a control experiment, but its results are not reported due to some errors in the measuring instruments. The columns were made from PVC pipes with one end glued unto an acrylic plexiglass using a waterproof JB weld Epoxy. The columns were insulated at their sides with two layers of single-faced fiberglass to minimize horizontal temperature propagation through the columns. The top of the columns was left open so that freezing will begin from the surface of the soil. The bottom of the columns was not insulated, but the acrylic plexiglass seal at the bottom of the columns was thick enough to prevent freezing from beneath the columns.

The soil was prepared at two different target moisture contents, 0.05 and 0.24 $m^3\,m^{-3}$ by thoroughly mixing by hand the appropriate amount of oven-dried soil and de-ionized water in a 34 L plastic container (Figure 3-3). For the saline treatments, the appropriate mass of salt was weighed and dissolved completely in the appropriate amount of de-ionized water before missing with the soil. Sodium chloride salt (181331 sodium chloride, crystalline) with percent purity ≥ 99.0 % from Fisher scientific was used for this experiment. The mass of salt, m_S, and volume of water, V_w, used for the various salt and moisture content treatments are detailed in Table 3-2 below.

Figure 3-3: Picture depicting the mixing of soil and water treatments with the hand

Table 3-2: Salt and water treatments used in the laboratory freezing experiment

Treatment	V_t (l)	θ_v $(m^3\ m^{-3})$	V_w (l)	c_S $(g\ l^{-1})$	m_S (g)
1	12.580	0.05	0.629	0	0
2	12.580	0.05	0.629	2	1.258
3	12.580	0.05	0.629	8	5.032
4	12.580	0.05	0.629	16	10.064
5	12.580	0.24	3.0192	0	0
6	12.580	0.24	3.0192	2	6.0384

Where c_S is the concentration of salt.

The soil was then packed into the columns at 5 cm intervals and compacted with the base of a 250 ml flat bottom flask. Three (3) pre-calibrated Steven's HydraProbes were inserted into the soil at 5 cm, 15 cm, and 30 cm depths in the columns (Figure 3-4). The Stevens HydraProbe was used because of three reasons 1) it was readily available 2) it can measure soil moisture content and temperature simultaneously and 3) it is the same instrument used in the field experiments. The Stevens HydraProbe measures soil moisture content using the dielectric method, which relates the measured dielectric constant to the moisture content through a calibration equation (calibration equation specified by the Steven Water monitoring System Inc, 2007). At each soil depth, a probe was inserted vertically into the soil, and the soil was packed around it. The probes were numbered according to their position within the column (probe 1 at 5 cm, probe 2 at 15 cm, and probe 3 at 30 cm, all from the start of the tines of the probes). This was to ensure that the same probe was used at the same depth every time the SFC was measured. Following the soil packing, the columns were covered with a polyethylene sheet to prevent evaporation and allowed to sit for two days for moisture to equilibrate in the columns.

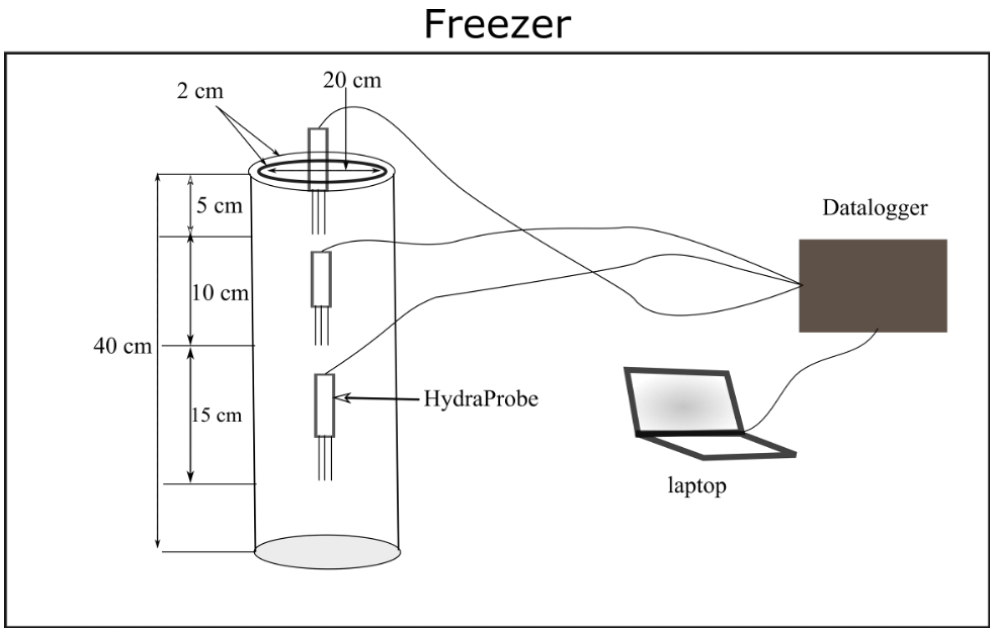

Figure 3-4: Schematic diagram of laboratory set-up for measuring the SFC

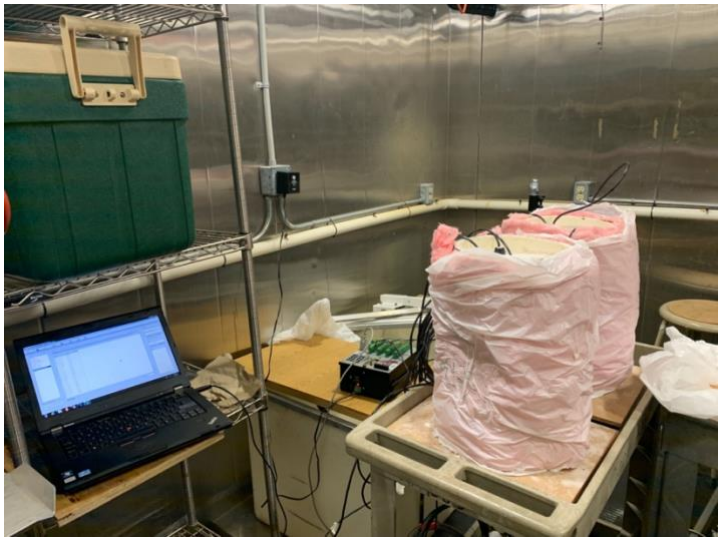

Figure 3-5: Actual laboratory set-up for measuring the SFC

The columns were then placed in a freezer (Figure 3-5) to measure the SFC. For every treatment, both the freezing and thawing curves were measured. For the freezing runs, the temperature of the freezer was set constantly at -5 ℃. The soil was allowed to freeze until the temperature of all the soil depths approached the freezer temperature or when the moisture content stayed constant. Afterwards, the temperature of the freezer was raised to and kept constant at 4 ℃ for the soil to thaw. The thawing runs were terminated when all the soil depths reached a temperature greater than 0 ℃. Soil moisture content ($m^3\ m^{-3}$) and temperature (℃) data were logged every minute using a CR 3000 series data logger from Campbell Scientific. The stored data were retrieved manually by means of a laptop for analysis.

3.2 Field Experiments

3.2.1 Description of study sites

The rationale behind the field study was to characterize the SMC and SFC for different fields with varying texture and salinity. The field studies were conducted using observations collected at the St Denis National Wildlife Area (SDN) in the Canadian prairies (Bam et al., 2019; Bam & Ireson, 2019) and the Boreal Ecosystem Research and Monitoring Sites (BERMS) Old Jack Pine (OJP) site in the boreal plans ecozone in Saskatchewan (Ireson et al., 2015; Nazarbakhsh et al., 2020), each of which is described below.

3.2.1.1 St. Denis study site

The St Denis (SDN) field site is located in the semi-arid, cold Canadian prairies ecozone about 40 km east (106° 5' 36" W, 52° 12' 34" N) of Saskatoon, Saskatchewan (Hayashi et al., 1998; Nachshon et al., 2014; Budhathoki, 2018). The site is partly cropped with wheat, barley, and canola while the rest of the vegetation is a combination of native and introduced grasses (Hayashi et al., 1998, Bam et al., 2019). The SDN site is characterized by an undulating hummocky topography (Hayashi et al., 1998; Nachshon et al., 2014; Bam et al., 2019) with silty stratified sediments and glacial tills (Hayashi et al., 1998; Nachshon et al., 2014; Bam et al., 2019). The top 5 m of the till is weathered and has hydraulic conductivity values ranging from 10^{-8} -$10^{-6}\ m\ s^{-1}$(Parsons et al., 2004). Soils at SDN can be high in salt, particularly sulphate salts (Nachshon et al., 2014). The site experiences mean annual precipitation (1967-1996) of about 358 mm, of which about 74 mm occurred as snow (November to April) (Budhathoki, 2018). The mean monthly temperature for the site is -14.7 ℃ around January and February and 18.7 ℃ between July and August months (Bam & Ireson, 2019).

3.2.1.2 Old Jack Pine study site

The Berms Old Jack Pine (OJP) site is located east of Prince Albert National park in the southern Canadian Boreal Forest (104.69° W, 53.92° N, and at an altitude of 579.3 m), Saskatchewan, Canada (Nazarbakhsh et al., 2020). As the name implies, the OJP site is dominated by jack pine (*Pinus banksiana Lamb.)* with an understory of reindeer lichen (*Cladonin spp*.) (Barr et al., 2012; Nazarbakhsh et al., 2020). The soil at OJP is a well or rapidly drained sandy soil (Barr et al., 2012; Nazarbakhsh et al., 2020) with a water table depth of at least 5 m below the soil surface (Barr et al., 2012). The OJP site receives an average precipitation of between 430 and 640 mm annually (Ireson et al., 2015). It is estimated that about 21 % to 31 % of the total precipitation at this site occurs as snow (Ireson et al., 2015, Nazarbakhsh et al., 2020). The site experiences a mean monthly temperature of around -10 ℃ in January and 20 ℃ in July (Nazarbakhsh et al., 2020).

3.2.2 Description of field data sets

The various data sets used in the field studies (for both the SDN and OJP sites), how the data were measured, and the steps involved in post-processing the data are described in this section.

3.2.2.1 SDN field site

At SDN, soil moisture data were measured on a stretch of cultivated land called the Uri transect which lies between two ponds (pond 107 and 108) (Budhathoki, 2018). A detailed description of the Uri transects and the pond system at the site is found in Budhathoki (2018). The Uri transect has three soil profiles, namely upslope, mid-slope and downslope (Budhathoki, 2018). In this study, however, only observation from the upslope profile is used and is referred to as URI 1. Data sets used in the SDN analysis include time series data of soil moisture content ($m^3\,m^{-3}$), soil temperature (℃), and matric potential (m). The soil moisture content and soil temperature were measured using Steven's HydraProbes from Campbell Scientific for five different soil depths (5 cm, 20 cm, 50 cm, 100 cm, and 300 cm). These HydraProbes are the same as those used in the laboratory experiments. In this study, soil moisture content and temperature measurements at the 5 cm, 20 cm and 50 cm depths are used. The reason the deeper depths were not used is that the soil

temperatures did not drop much below 0 ℃ at these depths. The soil matric potential was measured at the same soil depths as the other data sets (5 cm, 20 cm, and 50 cm) using the 229 heat dissipation matric water potential sensor from Campbell scientific.

3.2.2.2 OJP field site

For the OJP site, soil moisture content and temperature data sets for different soil depths exist. However, in this study, soil temperature data at 5 cm depth and moisture content data at the top 15 cm were used. The reason is that the soils do not freeze much below 15 cm, which could be because the trees and understory provide insulation that keeps the soil warm. This site also does not have matric potential measurements, which are needed for establishing the SMC. As such, SMC data set published by Cuenca et al. (1997) for the same field site was used in this study. Cuenca et al. (1997) measured moisture content using both the neutron probe (Campbell Pacific Nuclear 503 Hydroprobe) and the TDR. Soil matric potential was also measured using a combination of in situ tension disk infiltrometers and water retention data from the laboratory (measured using soil cores). These experiments are described in detail in the paper. The raw data points were extracted from the original plot using a WebPlotDigitizer application software (Version 4.2) (Rohatgi, 2015).

3.2.3 Data retrieval and post-processing

The data sets for both field sites were accessed and retrieved through the Global Institute of Water security's Water Information System KIsters (WISKI) using a python script. The data were stored as csv files and further imported into python for processing. Different start and end dates were selected each year for the drying curves (unfrozen period) as well as the freezing and thawing curves (frozen period) by carefully looking at the data sets. The start and end dates for the SDN site are published in Tables 3.3 and 3.4 below. Featured in the tables are the frequencies at which the data sets were sampled. Hourly frequency is denoted with 'H' in the tables. This same technique was employed at the OJP site to identify the start and end dates for the freezing and thawing periods. The start and end dates for the OJP site are not reported here because they are not as uniform as those of the SDN site.

Table 3-3: Start and end dates for the SDN URI 1 drying curves

Year	Start date	End date	Frequency of data
URI 1, 5cm			
2013	2013-05-01	2013-09-24	H
2014	2014-08-15	2014-09-30	H
2015	2015-06-28	2015-07-30	H
2016	2016-06-24	2016-07-10	H
2017	2017-06-21	2017-07-31	H
2018	2018-06-13	2018-07-20	H
URI 1, 20 cm			
2013	2013-08-10	2013-09-24	H
2014	2014-08-02	2014-09-24	H
2015	2015-06-28	2015-07-26	H
2016	2016-06-29	2016-07-28	H
2017	2017-06-30	2017-07-29	H
2018	2018-06-20	2018-09-20	H
URI 1, 50 cm			
2013	2013-08-29	2013-09-30	H
2014	2014-08-20	2014-09-30	H
2015	2015-07-21	2015-07-26	H
2016	2016-08-31	2016-09-30	H
2017	2017-07-31	2017-09-30	H
2018	2018-08-31	2018-09-30	H

Table 3-4: Start and end dates for the freezing period (F) and thawing period (T) for SDN URI 1

Year	Start date	End date	Data type	Frequency of data
URI 1, 5cm				
2013	2013-11-06	2013-12-12	F	H
	-	-	-	-
2014	2014-11-30	2014-12-31	F	H
	2014-03-01	2014-04-24	T	H
2015	2015-01-31	2015-02-28	F	H
	2015-03-01	2015-03-30	T	H
2016	2016-11-30	2016-12-31	F	H
	-	-	-	-
2017	2017-11-22	2017-12-31	F	H
	2017-03-01	2017-04-09	T	H
2018	2018-11-30	2018-12-31	F	H
	2018-03-31	2018-04-23	T	H
URI 1, 20 cm				
2013	2013-11-11	2013-12-31	F	H
	-	-	-	-
2014	2014-11-30	2014-12-31	F	H
	2014-03-01	2014-04-29	T	H
2015	2015-01-31	2015-02-28	F	H
	2015-03-01	2015-04-04	T	H
2016	2016-11-30	2016-12-31	F	H
	-	-	-	-
2017	2017-11-17	2017-12-31	F	H
	2017-03-01	2017-05-02	T	H

2018	2018-11-17	2018-12-31	F	H
	2018-03-01	2018-04-25	T	H
URI 1, 50 cm				
2013	-	-	-	-
	-	-	-	-
2014	2014-01-31	2014-02-28	F	H
	2014-03-01	2014-05-02	T	H
2015	2015-01-21	2015-02-28	F	H
	2015-03-01	2015-04-09	T	H
2016	-	-	-	-
	-	-	-	-
2017	2017-01-31	2017-02-28	F	H
	2017-03-01	2017-05-10	T	H
2018	2018-01-31	2018-02-28	F	H
	2018-03-01	2018-04-25	T	H

3.3 Modelling

As noted earlier, two possible causes of freezing point depression in soils have been identified: i) capillarity and adsorption effects on the free-energy of the pore-water, which is related to the soil pore-size distribution (hereafter capillary effects); and ii) effect of salt on the freezing temperature of water. In this study, models are applied to simulate the soil freezing characteristic curve assuming: 1) capillary effects alone; 2) salinity effects alone; and 3) combined capillary and salt effects. The objective of this part of the thesis is to develop models to represent all three scenarios so they can be validated using the field and laboratory observations.

3.3.1 Model governing equations

Note that here, the unit of temperature is always in Kelvin. The soil temperature is denoted T. The freezing temperature for free pure water at atmospheric pressure is denoted T_0 and has a value of 273.15K. The freezing temperature of soil water under a specific set of conditions is denoted as T_f. The freezing point depression of soil water is also denoted T_d and is the negative temperature below T_0. Hence

$$T_f = T_0 + T_d \tag{3.1}$$

3.3.1.1 Capillary effect model

In the absence of salt, freezing point depression is solely due to attractive forces generated by the soil pores (capillarity and adsorption) and this is represented by the Generalized Clapeyron Equation, GCE, which relates matric potential to freezing temperature as in Equation 2.56 of section 2.5.2.1. For the purpose of this study, Equation 2.56 is slightly modified as in Equation 3.2.

$$\psi = min\left(\psi_a, \frac{L_f}{g} \ln\left(\frac{T}{T_f}\right)\right) \tag{3.2}$$

Equation 3.2 can be approximated as

$$\psi = min\left(\psi_a, \frac{L_f\left(T_f - T_0\right)}{g \cdot T_f}\right)$$

which is the same as

$$\psi = min\left(\psi_a, \frac{L_f \cdot T_d}{g \cdot T_f}\right) \tag{3.3}$$

Where ψ_a is the actual matric potential.

The effective matric potential, ψ (m) is related to liquid water content through the van Genuchten equation (VGN) as in equation 3.4 (van Genuchten, 1980; Kelleners & Norto, 2012; Qi et al., 2018)

$$\theta_L = \theta_R + (\theta_s - \theta_R)(1 + (\alpha\psi)^n)^{-m} \quad (3.4)$$

Combining Equation 3.3 and 3.4 results in a relationship for the liquid water content as a function of freezing temperature and the actual matric potential. This relationship describes the SFC for soils without salts. Figure 3-6 below shows the behavior of the capillary model simulated using arbitrary soil parameters (parameters values are summarized in Table 3-5).

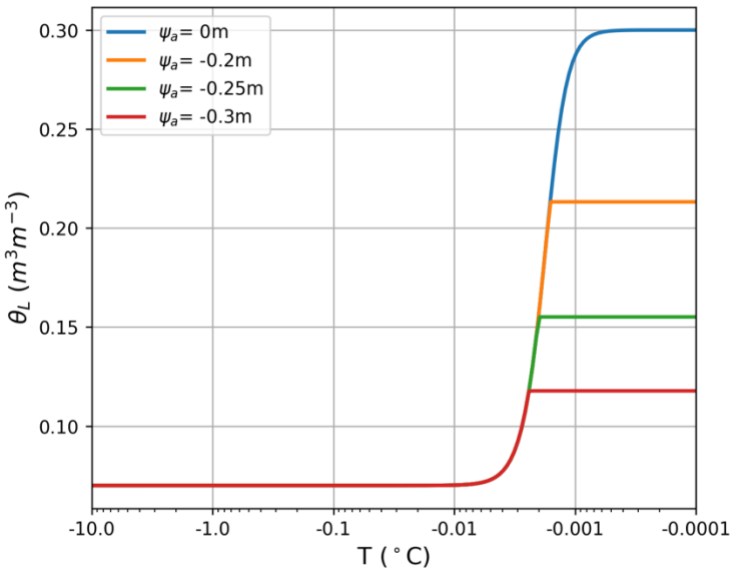

Figure 3-6: Capillary model simulations with arbitrary soil parameters and differing ψ_m (or differing total water contents)

Table 3-5: Arbitrary soil parameters used in the model simulations

VGN parameters	Value
α (m^{-1})	-4.79
n	5
$m(1 - 1/n)$	0.8
θ_r (m^3 m^{-3})	0.07
θ_s (m^3 m^{-3})	0.3

3.3.1.2 Salt exclusion model

In saline frozen soils, salts are excluded from the ice phase during freezing, making the remaining solution more concentrated leading to a further depression in the freezing point of the remaining liquid water. If capillary effects are ignored, the freezing point depression (T_d) will depend solely on salt concentration. Table 3-6 show observed data for salt concentration against freezing point depression for sodium chloride salt (NaCl).

Table 3-6: Freezing point depression of an aqueous NaCl solution (from Haghighi et al., 2008)

Salt mass X (%)	1	5	10	15	18
$\mathbf{T_d}$ **(K)**	0.58	3.04	6.79	11.02	14.29

Let X (%) be the mass fraction of salt in an aqueous solution such that

$$X = \left(\frac{m_s}{m_w}\right) 100 \tag{3.5}$$

The mass of salt can be converted to concentration of salt, $c\ (g\ l^{-1})$ by multiplying by the density of liquid water, $\rho_L\ (g\ l^{-1})$, as in Equation 3.6

$$c = \frac{X \cdot \rho_L}{100} \tag{3.6}$$

The relationship between freezing point depression and salt concentration is assumed to be a 2nd order polynomial function passing through the origin

$$c = p_1 \cdot {T_d}^2 + p_2 \cdot T_d \tag{3.7}$$

p_1 and p_1 are found by fitting Equation 3.7 to the observed data using linear regression (Figure 3-7).

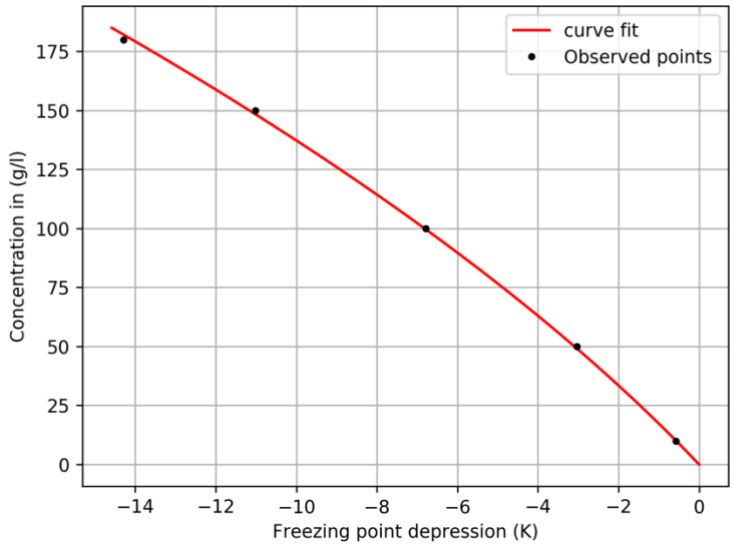

Figure 3-7: Polynomial relationship describing freezing point depression of NaCl saline solution

Following the fitting, the values of p_1 and p_2 were found to be -0.34179 and -17.36659, respectively. Moreover, making T_d the subject of Equation 3.7 above results in a quadratic formula (Equation 3.8).

$$T_d = \frac{-p_2 - \sqrt{{p_2}^2 + 4p_1 \cdot c}}{2p_1} \tag{3.8}$$

Now, assuming that the mass of salt in a control volume, m_s, is fixed, then;

$$c = \frac{m_s}{(\theta_L - \theta_R) \cdot V} \tag{3.9}$$

Inserting Equation 3.9 into 3.8 gives Equation 3.10, which can further be substituted into Equation 1 to give equation 3.11.

$$T_d = \frac{-p_2 - \sqrt{{p_2}^2 + \frac{m_s \cdot 4p_1}{(\theta_L - \theta_R) \cdot V}}}{2p_1} \tag{3.10}$$

$$T_f = T_0 + \frac{-p_2 - \sqrt{{p_2}^2 + \frac{m_s \cdot 4p_1}{(\theta_L - \theta_R) \cdot V}}}{2p_1} \tag{3.11}$$

Solving Equation 11 for θ_L gives

$$\theta_L = \frac{m_s \cdot 4p_1}{\left(\left((T_0 - T_f)2p_1 - p_2\right)^2 - {p_2}^2\right)V} + \theta_R \tag{3.12}$$

Now, if $T_f = T$, this equation returns the maximum possible liquid water content for a given m_s. This is true since if any further liquid water is added, the concentration would reduce, the freezing point temperate would increase, and this liquid water would freeze. The actual liquid water content, then, is given by

$$\theta_L = min\left(\theta_T, \frac{m_s \cdot 4p_1}{\left(\left((T_0 - T_f)2p_1 - p_2\right)^2 - {p_2}^2\right)V} + \theta_R\right) \tag{3.13}$$

where θ_T is the total water content, corresponding to ψ_a. This model then predicts θ_L based on ψ_a and m_s, with no dependency on the soil hydraulic properties. Simulation of the salt exclusion model for different salt concentrations and moisture content is shown in Figure 3-8 below. The simulations show that freezing point depression increases with increasing salt concentration or more water remains unfrozen at the same temperature at higher salt concentrations (represented by a shift of the curve to the left-hand side of the plot).

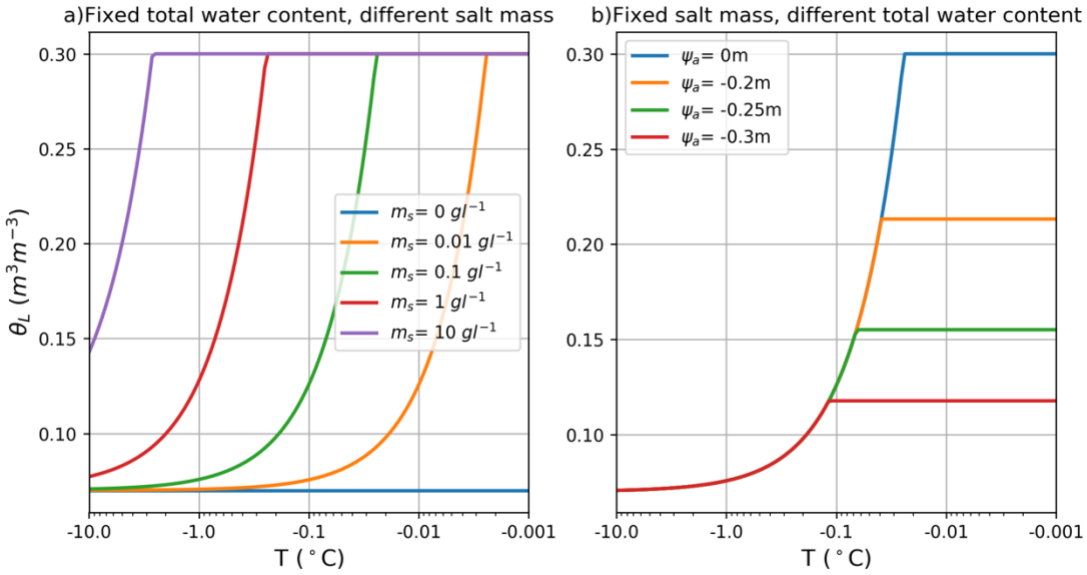

Figure 3-8: Simulated results for the salt exclusion model using arbitrary parameters and differing (a) salt mass (per bulk soil volume) and (b) ψ_m (or total water contents)

3.3.1.3 Combined capillary salt model

Now Equation 3.3 describes freezing point depression due to capillary forces and Equation 3.11 describes freezing point depression due to salt. In order to represent the effect of both capillary forces and salts, Equation 3.3, 3.4 and 3.11 must be combined, isolating θ_L at one end of the resulting equation. However, combining these three equations results in Equation 3.14 with θ_L on both sides of the equation. Thus, the equation remains unsolvable and this was verified with symbolic python (sympy).

$$\theta_L = min\left(\psi_a, \theta_R + (\theta_s - \theta_R)\left[\left[\frac{L_f \cdot T_d \cdot \alpha \left[T_0 + \frac{-p_2 - \sqrt{{p_2}^2 + \frac{m_s \cdot 4p_1}{(\theta_L - \theta_R)V}}}{2p_1}\right]}{g}\right]^n + 1\right]^{-m}\right) \quad (3.14)$$

The following iterative procedure was, therefore employed in solving equation 3.14:

1) Initial guess for $\theta_L = \theta_{L,i}$

2) Calculate T_f from Equation 3.11

3) Calculate ψ with Equation 3.3

4) Calculate θ_L with Equation 3.4

5) If $(\theta_L - \theta_{L,i})^2 > \epsilon$ then set $\theta_{L,i} = \omega\theta_L + (1 - \omega)\,\theta_{L-i}$ and return to 2. Repeat until converged or until maximum number of iterations is exceeded.

6) If the maximum number of iterations is exceeded, reduce the value of ω to 0.75 and rerun the model until it converges else ω is further reduced. If $\omega < 0.01$, the model has failed. Here ϵ is the maximum error threshold and ω is a weighting coefficient.

The same scenarios of salinity and moisture content simulated with the salt exclusion model were simulated using the combined capillary salt model (Equation 3.14), and the outputs are summarized in Figure 3.9. The same soil parameter values presented in Table 3-5 above were used.

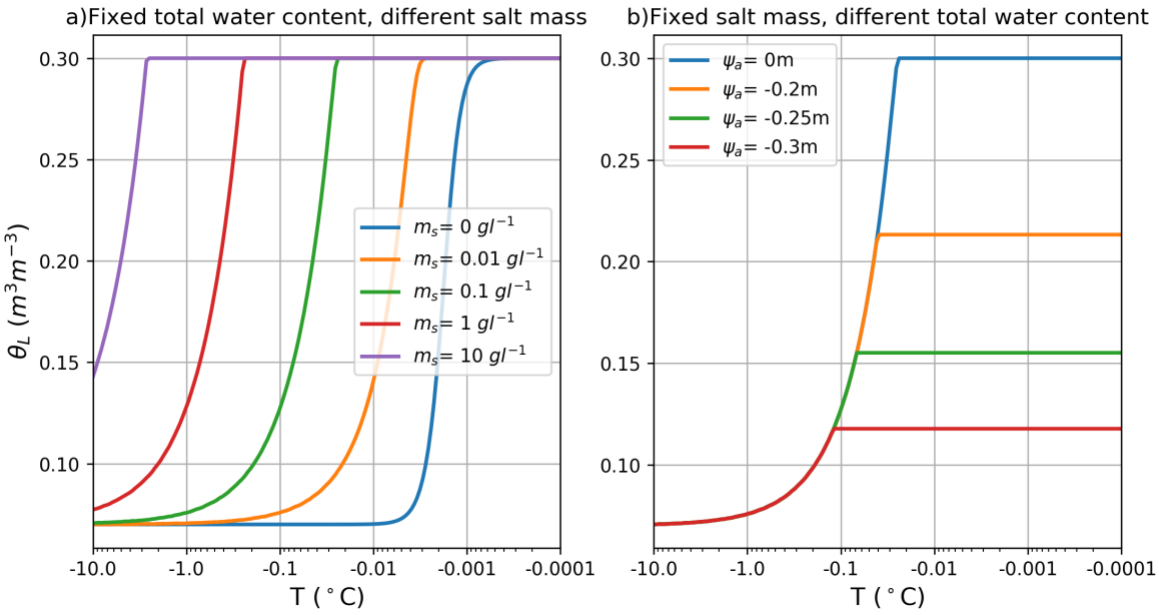

Figure 3-9: Simulations for the combined capillary salt model (Equation 3.14) using arbitrary soil parameter and differing (a) salt mass (per bulk soil volume) and (b) ψ_m (or total water contents)

The simulations for the combined capillary salt model (Figure 3-9) are qualitatively similar to those of the salt-exclusion model (Figure 3-8) even though the salt exclusion model is independent of the particle size distribution of the soil. Now the three models are compared quantitatively in Figure 3-10. Note that, the scenarios in Figure 3-10 are the same as those presented in Figure 3-6, 3-8 and 3-9.

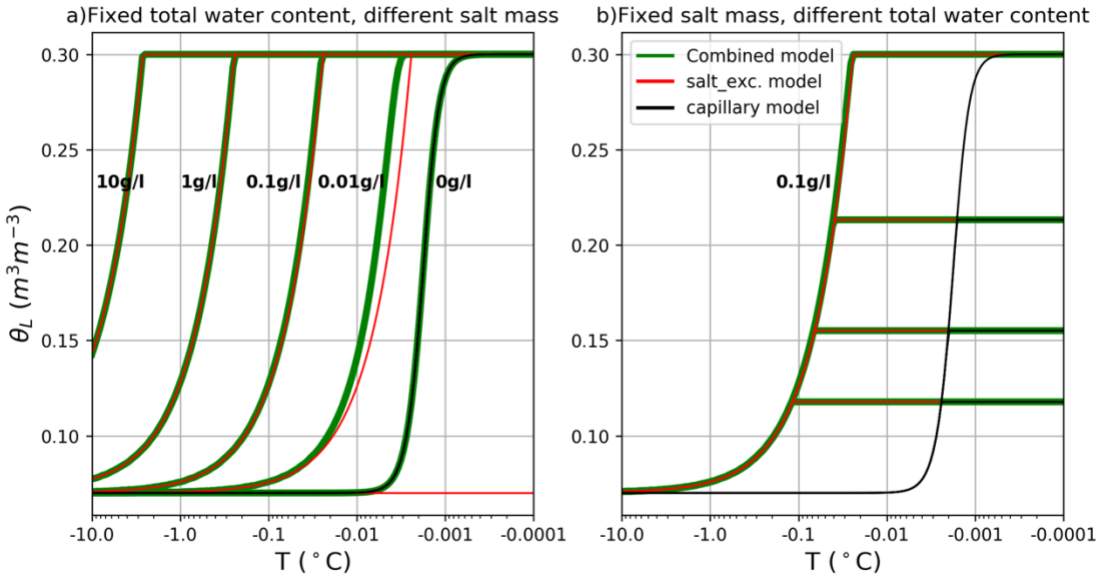

Figure 3-10. Comparing the outcomes of the 3 models

As shown in Figure 3-10a, in the absence of salt (0 $g\ l^{-1}$), the combined capillary salt model predicts the same liquid water content as the capillary model at the same freezing temperature. This outcome is as expected because, without salts, the combined capillary salt model is the same as the capillary model. Conversely, as salt is added to the soil, the combined capillary salt model having the capacity to accounts for salts responds to the salt and predict more liquid water content at the same temperature than the capillary model. The capillary model, on the other hand, is insensitive to salts and will not respond to the added salt. Further, with no salt, the salt-exclusion model predicts zero freezing point depression which is to say that all of the water turns into ice at 0 °C (flat line in Figure 3-10a), which make sense because the model is solely dependent on the mass of salt, so if there is no salt the water will freeze at the freezing point of bulk water (0 °C). The results also show that at lower salinities (0.01 $g\ l^{-1}$ and 1 $g\ l^{-1}$), the combined capillary salt model predicts more liquid water than the salt exclusion model at the same temperature, but at higher salinities (1 $g\ l^{-1}$ and 10 $g\ l^{-1}$), both models perform the same. The reason behind this observation is that as salt concentration increases, salts become the dominant force controlling freezing point so that there is no difference between the two models (salt exclusion and combined capillary salt models).

CHAPTER 4

RESULTS AND DISCUSSION

This chapter is organized into three sections. In section 4.1, results for the laboratory experiments are discussed. In section 4.2 results for both the SDN and OJP field sites are discussed. Finally, the capillary, salt exclusion and combined capillary salt models are compared with the observed data from the laboratory and the field sites in section 4.3.

4.1 Results for laboratory experiments

In this section of the thesis is the summary of the results for the laboratory experiments. The results for the SMC are detailed in subsection 4.1.1. The SFCs, including separate freezing and thawing curve as well as freeze-thaw plots for two moisture treatments, 0.05 $m^3\ m^{-3}$ (low moisture content) and 0.24 $m^3\ m^{-3}$ (high moisture content) are found in subsection 4.1.2.

4.1.1 Soil moisture characteristic curve

The observed SMC for the silica sand that was measured in a laboratory drying experiment, as described in section 3.1.1, is shown in Figure 4-1. The van Genuchten model (VGN) was fit to these data. The saturated moisture content (θ_s) was set to be equal to the measured porosity of the soil (0.42 $m^3\ m^{-3}$, see Table 3-1 of section 3.1). The residual moisture content (θ_r) was identified as the moisture content at which the matric potential of the soil stayed constant. The parameters n, m, and α were obtained by optimization, minimizing the root mean squared error (RMSE) in water content. After fitting the RMSE was 0.017. The green dots are observed data points from the start of the experiment and were excluded from the fitting because they were not consistent with a typical SMC curve. This may have been due to 1) errors in the measuring instrument or 2) unstable conditions in the soil sample at the beginning of the experiment.

The observed data did not extend up to 0 m (matric potential), because the soil was not completely saturated at the start of the experiment. The fitted parameters are summarized in table 4-1.

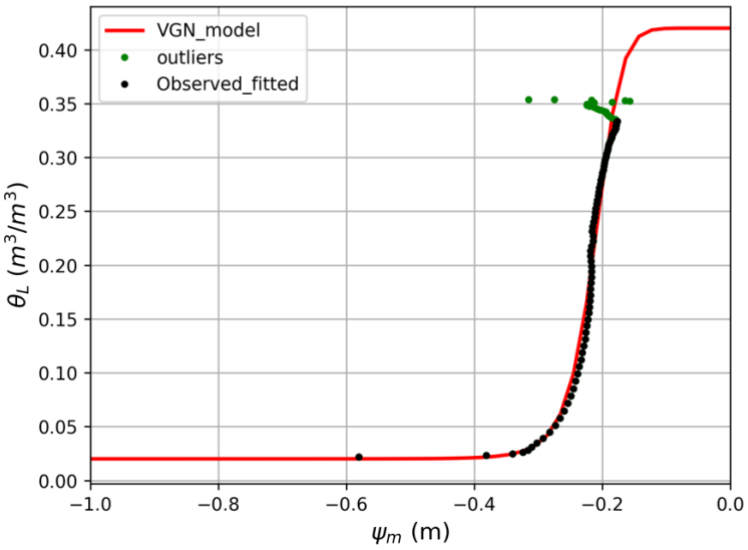

Figure 4-1: The soil moisture characteristic curve of silica sand measured using the HYPROP apparatus (black dots) and fitted to the van Genuchten model (solid red line)

Judging from the results, this soil has poor water retention, and drains rapidly as the matric potential drops below about -0.1 m. The soil reaches its residual moisture content (about 0.02 $m^3\ m^{-3}$) at a matric potential of about -0.38 m. This result is typical of coarse textured soils that lose moisture rapidly due to their large pore sizes.

Table 4-1: Fitted parameters and RMSE for the SMC of the silica sand

VGN parameters	Value
$\alpha\ (m^{-1})$	-4.79
n	10.11
$m(1-{}^{1}/_{n})$	0.90
$\theta_r\ (m^3\ m^{-3})$	0.02
$\theta_s(m^3\ m^{-3})$	0.42

4.1.2 Soil freezing characteristic curves

SFCs were measured for the silica sand for freezing and thawing conditions at two different target unfrozen moisture contents, 0.05 $m^3\ m^{-3}$ and 0.24 $m^3\ m^{-3}$. For the lower moisture content treatments (0.05 $m^3\ m^{-3}$), measurements were obtained with four NaCl concentrations: 0 $g\ l^{-1}$(no salt), 2 $g\ l^{-1}$, 8$g\ l^{-1}$, and 16 $g\ l^{-1}$. For the higher moisture content treatment (0.24 $m^3\ m^{-3}$), SFCs were obtained for 0 $g\ l^{-1}$ (no salt), and 2 $g\ l^{-1}$ (measurements at 8$g\ l^{-1}$, and 16 $g\ l^{-1}$ were not obtained due to the laboratory shutdown associated with the COVID 19 pandemic). For each experiment, observations were taken at three depths in the column, 5 cm, 15 cm and 30 cm. The observations are shown in Figure 4-2 and 4-3, respectively. Also, the separate freezing and thawing curves are compared in the freeze-thaw plots of Figure 4-2 and 4-3.

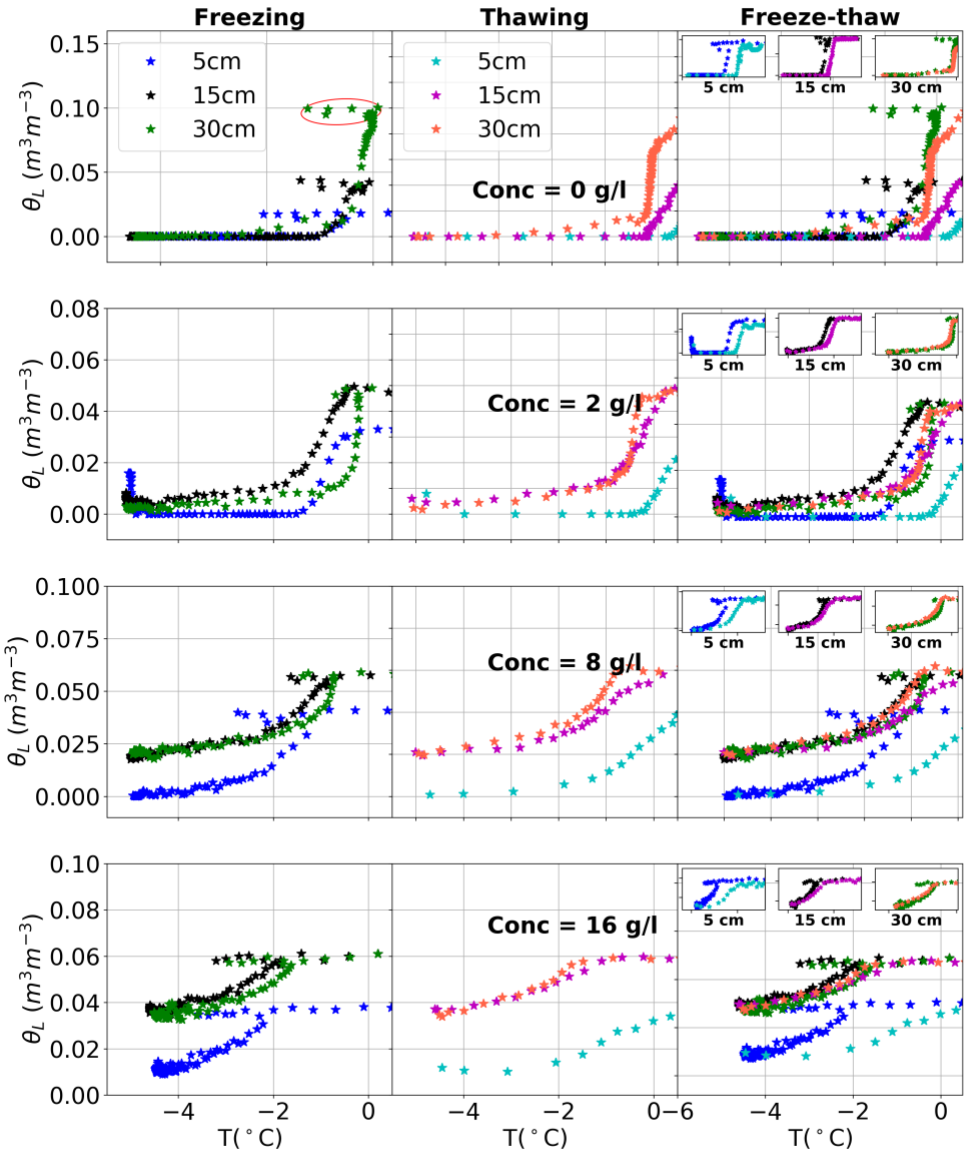

Figure 4-2: The SFCs of the silica sand for different salt concentrations measured at a target moisture content of 0.05 $m^3\ m^{-3}$. The small insert plots in column 3 of each panel is the comparison of the freezing and thawing curves for the different soil depths. The red ring in the first plot of panel 1 (from the top) represents supercooling.

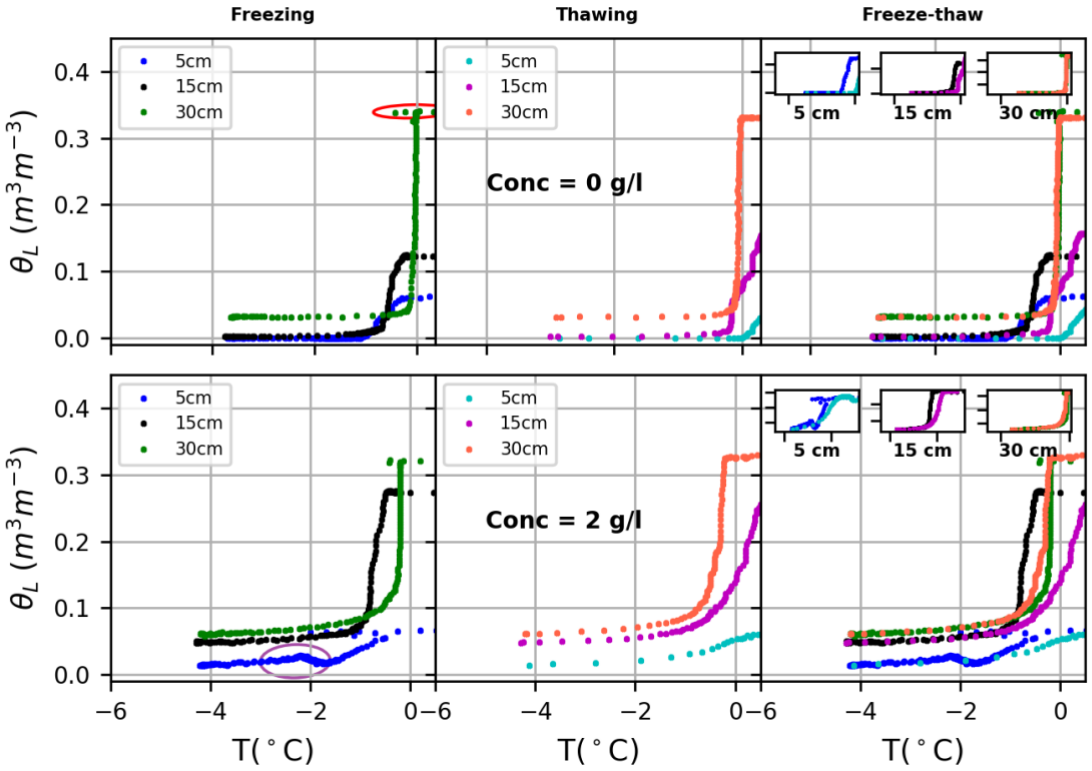

Figure 4-3: The SFCs of the silica sand for different salt concentrations measured at a target moisture content of 0.24 $m^3\ m^{-3}$. The small insert plots in column 3 of each panel is the comparison of the freezing and thawing curves for the different soil depths. The red ring in the first plot of panel 1 (from the top) represents supercooling.

The results show a vertical redistribution of moisture in the soil column, especially for the higher moisture content treatments (Figure 4-3) with the deeper depths (30 cm) having more moisture than the shallower depths (5 cm has the lowest moisture). This is due to the movement of moisture by gravity during the time the soil was left to equilibrate. Secondly, for all soil depths, soil moisture decreased with decreasing soil temperature during freezing (Figure 4-2 and 4-3). The results also reveal the phenomenon of supercooling during soil freezing (red rings in Figure 4-2 and 4-3). The temperature of the soil decreased to what is termed as the temperature of spontaneous nucleation (T_{SN})(Kozlowski, 2009; Zhou et al., 2020) without a change in moisture content. Supercooling is a metastable stage in freezing and is common in laboratory experiments. T_{SN} is the temperature at

which a stable ice nucleus for ice crystallization forms in a freezing soil (Kozlowski, 2009; Zhang et al., 2020). After reaching the T_{SN} there is a release of latent heat that warms the soil to its freezing point where freezing begins (Kozlowski, 2009; Ren & Vanapalli, 2020; Zhou et al., 2020). Depicted in the purple ring in Figure 4.3 above and more clearly in Figure 4-5 below is possible evidence of moisture migration during soil freezing. Here the liquid moisture increased with decreasing soil temperature. This observation may be due to the migration of moisture from unfrozen layers toward the freezing front, a phenomenon termed as cryosuction. Experiments of Mizoguchi (1990), as described in Hansson et al. (2004) revealed the same phenomena during soil freezing. According to Hansson et al. (2004), this is due to the high hydraulic gradient established in the soil during freezing which causes moisture to move upwards toward the freezing front. At the freezing front, the migrated water refreezes, resulting in an increase in the total moisture content of the soil at the freezing front.

Meanwhile, during thawing, the liquid water content increased as the soil warmed up. The thawing curves of the SFC, are qualitatively similar to the freezing curves except for the supercooling effect, which is absent. Quantitatively, however, the freezing limb of the SFC tend to hold more moisture than the thawing limb at the same temperature which is to say that the SFCs are hysteretic. As depicted in the freeze-thaw plots in Figure 4-2 and 4-3, at every temperature between 0 and about -2 ℃ the freezing curves of the SFC held more moisture than the thawing curves. This result is consistent with previously reported curves from Koopmans & Miller (1966), Tice et al. (1989) and Watanabe & Osada (2017). The hysteretic effect decreased with soil depth with the 30 cm depth showing negligible to no difference between the thawing and freezing curves.

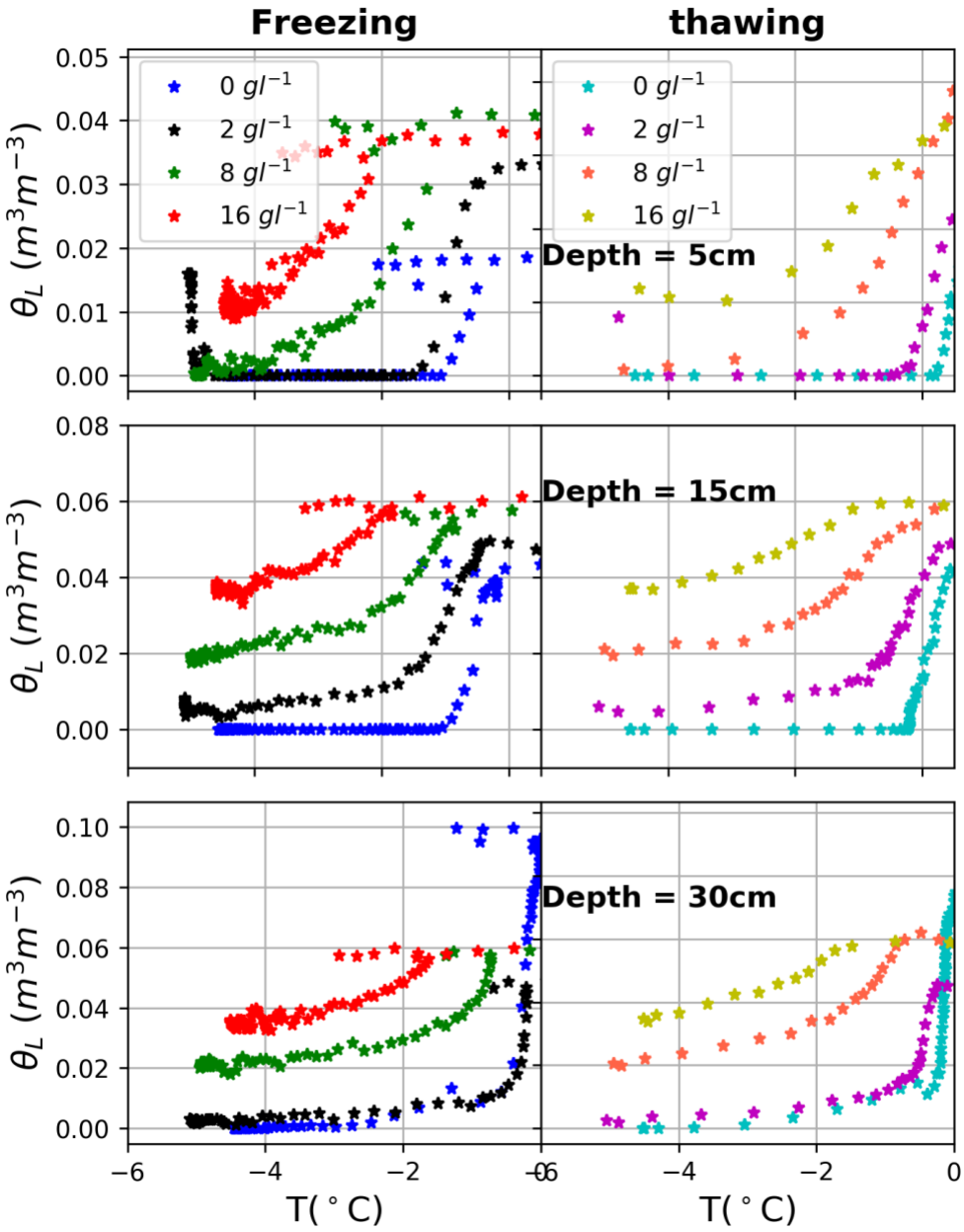

Figure 4-4: Comparison of the SFCs of different salt concentrations at a target moisture content of $0.05\ m^3\ m^{-3}$

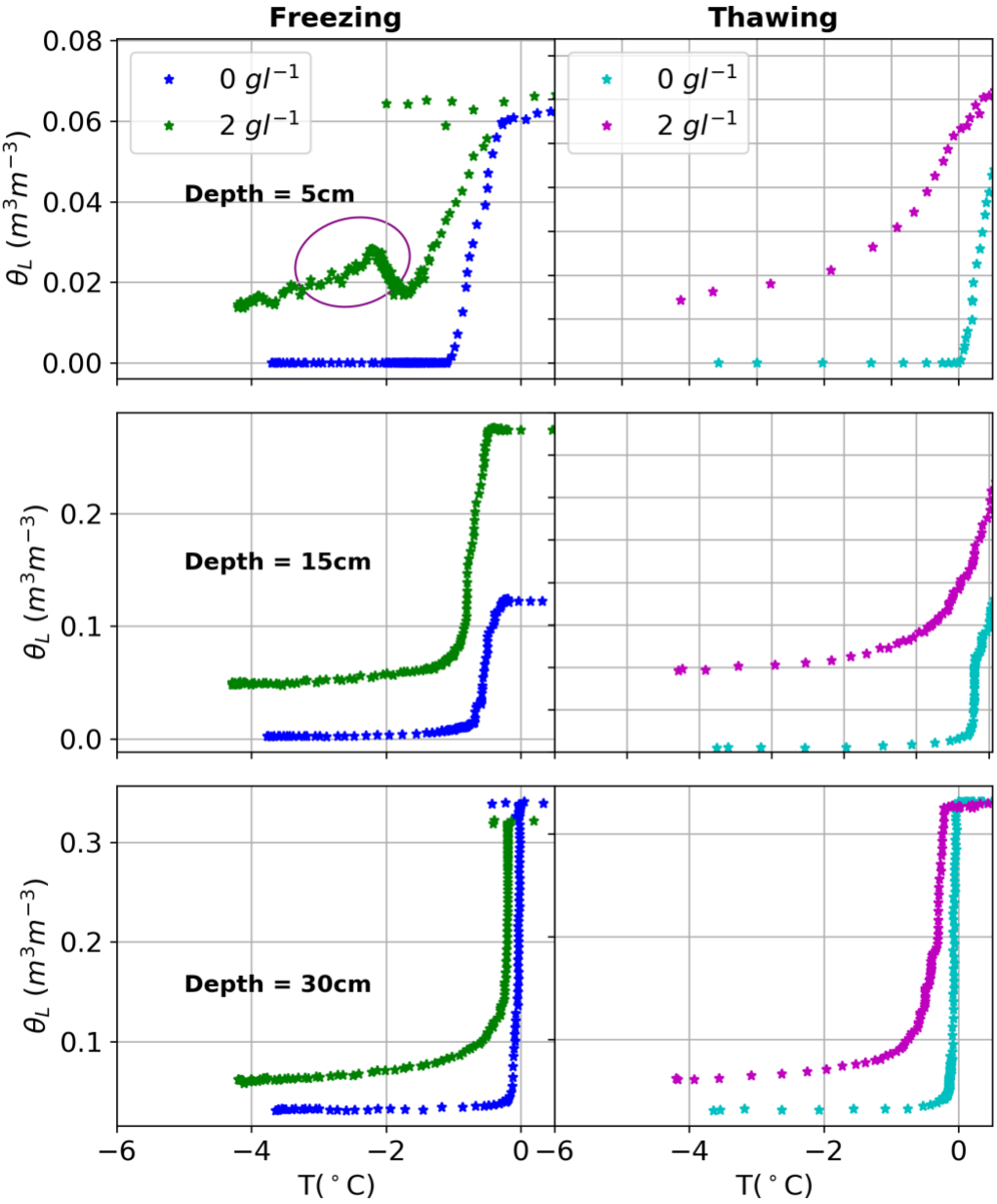

Figure 4-5: Comparison of the SFCs of different salt concentrations at a target moisture content of $0.24\ m^3\ m^{-3}$

SFCs for the different pore-water dissolved salt concentrations are plotted in Figure 4-4 (at a target moisture content of 0.05 $m^3\ m^{-3}$) and Figure 4-5 (at a target moisture content of 0.24 $m^3\ m^{-3}$). The results show, as expected, that higher salinity results in enhanced freezing point depression, or in other words, more liquid water is retained in the soil at higher salt concentrations. Conceptually the salts shift the freezing curve to the left-hand side of the plot, which is exactly the same as what was seen with the salt exclusion and combined capillary salt models in the presence of salts in section 3.3.

4.2 Results for field experiments

This section of the thesis is devoted to discussing the results for the SDN and the OJP field sites.

4.2.1 SDN-Soil moisture and freezing characteristic curves

Here, results for the SDN soil moisture profile are presented. The SMCs for the SDN site fitted to the VGN model (pink solid line) are presented in Figure 4-6 below. The results show that the SMCs for the different years are different. Some specific reasons for this observation may include 1) shrinking or swelling of the soils, particularly because the soil here is rich in clay, and 2) the shifting of measuring instruments due to any of the other two reasons. This thesis does not address the changing SMCs with time, the 2013 curves are used in all analysis, since the 2013 curves are wetter than the other years and looks reasonably consistent at all the soil depths. The curves were fitted to the VGN model by minimizing the root mean square error (RMSE), which is calculated from the difference between the observed moisture content and the predicted moisture content from the VGN model. The final parameter values for the fittings are documented in Table 4-2.

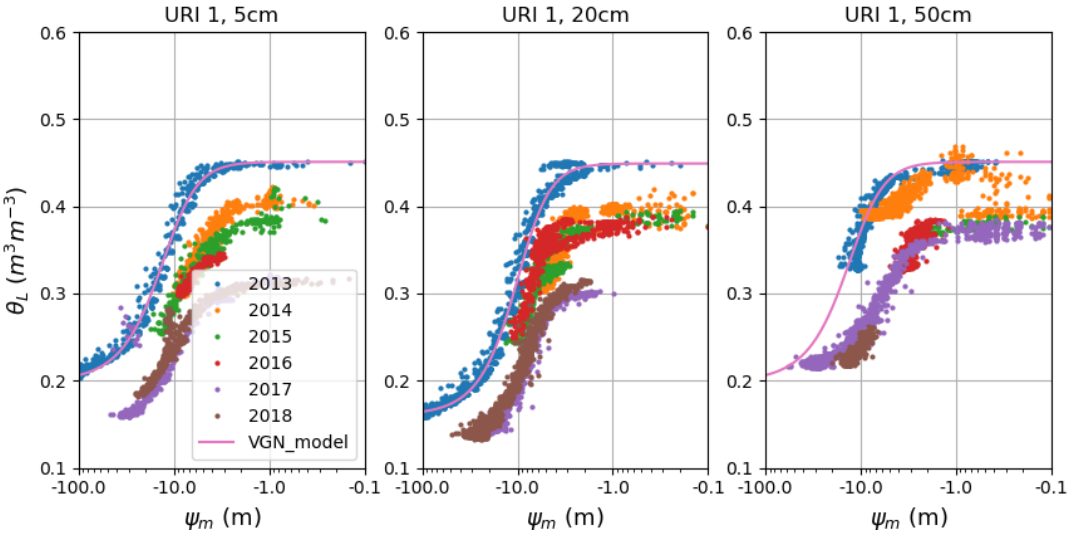

Figure 4-6: Soil moisture characteristic curve for SDN URI 1 fitted to the VGN model

Table 4-2: Fitted parameter values of VGN for SDN URI 1

Soil depth	Fitted year	α (m^{-1})	n	m $(1 - 1/n)$	θ_r ($m^3\ m^{-3}$)	θ_s ($m^3\ m^{-3}$)	RMSE
5 cm	2013	0.094	2.55	0.61	0.198	0.45	0.0095
20 cm	2013	0.12	2.72	0.63	0.16	0.45	0.0119
50 cm	2013	0.094	2.55	0.61	0.198	0.45	0.0095

The SFCs for the SDN site is shown in Figure 4-7. For the 50 cm soil depth, some of the years have no freezing and thawing data, since the soil at this depth did not freeze significantly (i.e. drop much below 0 ^{o}C).

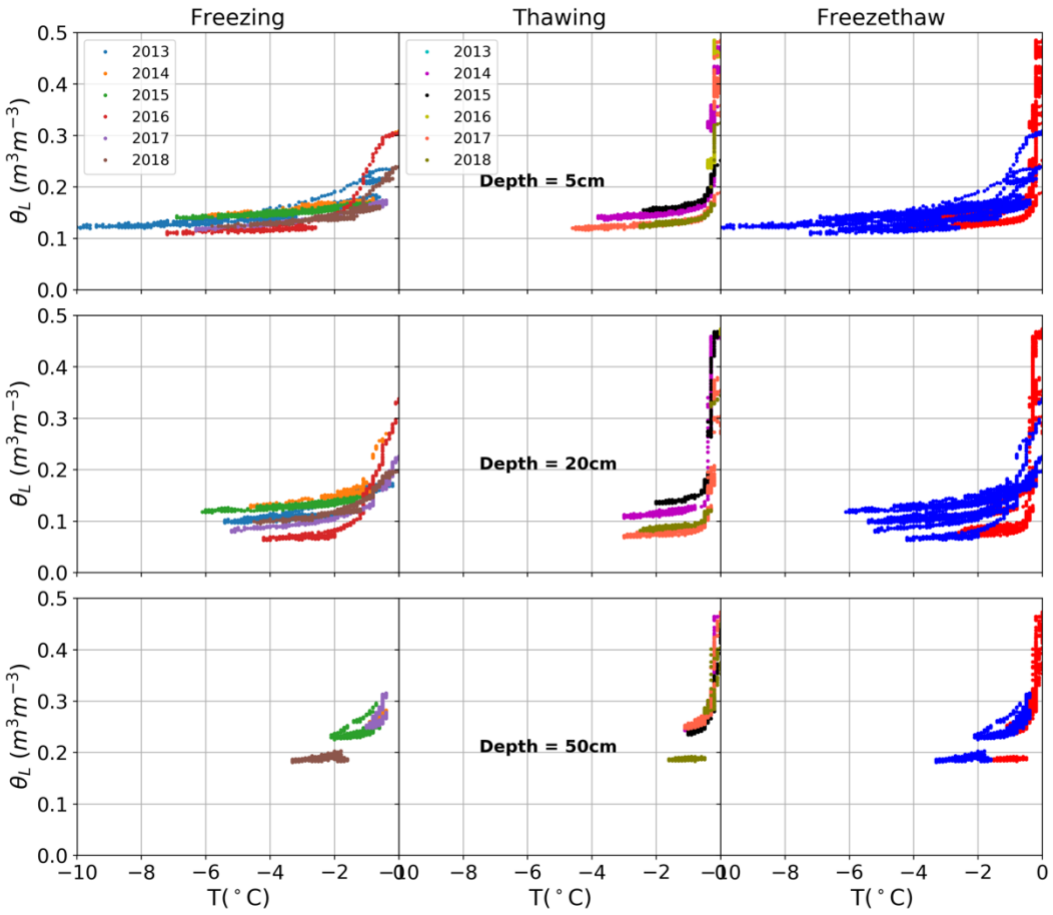

Figure 4-7: Soil freezing characteristic curves for SDN URI 1

It can be seen also that the initial moisture content of the freezing curves depends on how wet the soils were before freezing. Soil freezing commenced around November each year and the soils at this time were reasonably dry and that is why the freezing curves are not fully saturated. How dry the soils were, depends on how much rainfall fell in the late summer or fall months. The thawing curves, however, end with a very wet, perhaps fully saturated, condition, which may be due to snowmelt infiltration and/or cryosuction, which results in an increase in the total moisture content of the soil after thawing. Finally, the freeze-thaw plots (plots on the column 3) shown here are hysteretic in nature. Thus, the freezing curve (in blue color) at the same temperature holds more liquid water than the thawing curves (in red color).

4.2.2 OJP-soil moisture and freezing characteristic curves

The SMC of the OJP site (blue dotted line) and the VGN model (red line) is shown in Figure 4-8. The SMC data were measured by Cuenca et al. (1997) using in situ moisture probes and tension disk infiltrometers as well as soil cores in the laboratory (refer to section 3.2.2.2 of the thesis or Cuenca et al., 1997 for more details on how the SMC was measured). Similar to the laboratory soil, the OJP soil is coarse textured and loses moisture rapidly.

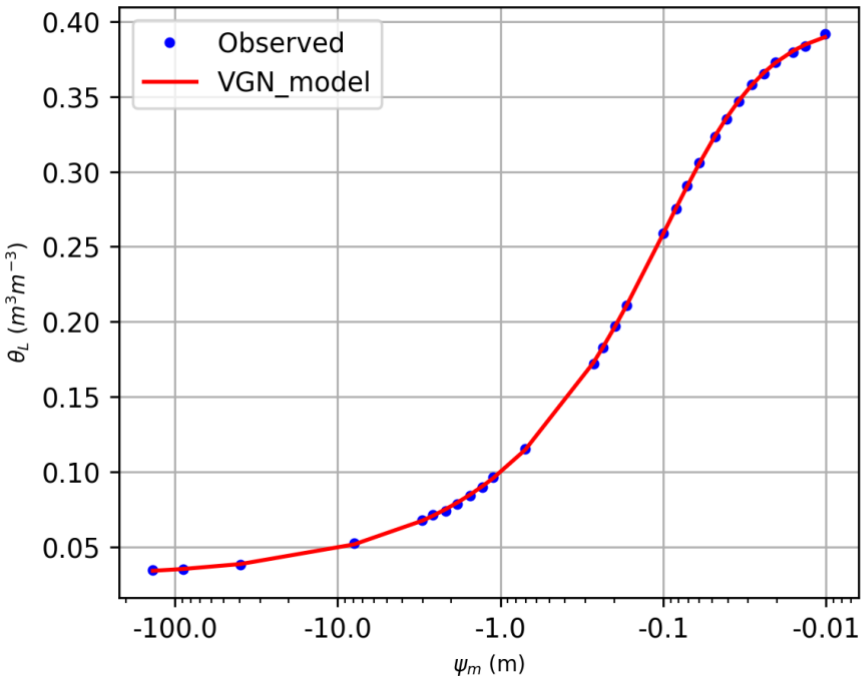

Figure 4-8: Soil moisture characteristic curve for OJP site fitted to the VGN model

Table 4-3: Fitted parameter values of VGN for OJP site

Parameter	α (m^{-1})	n	m $\left(1-{}^{1}/_{n}\right)$	θ_r $(m^3\ m^{-3})$	θ_s $(m^3\ m^{-3})$	RMSE
value	19.44	1.6	0.4	0.03	0.4	0.00076

The SFCs, including separate freezing and thawing curves as well as freeze-thaw plots for the same site, are summarized in Figure 4-9 below. The results are consistent with those observed in the laboratory and at the SDN site. Soil moisture content decreases with decreasing soil temperature during freezing, and the vice versa is true for thawing. Also, the SFC is shown to be hysteretic, but not as significant as at the SDN site. Again, the soil condition after thawing is wetter than at the start of freezing, which is due to the same reasons as discussed for the SDN site, snowmelt infiltration and or cyosuction.

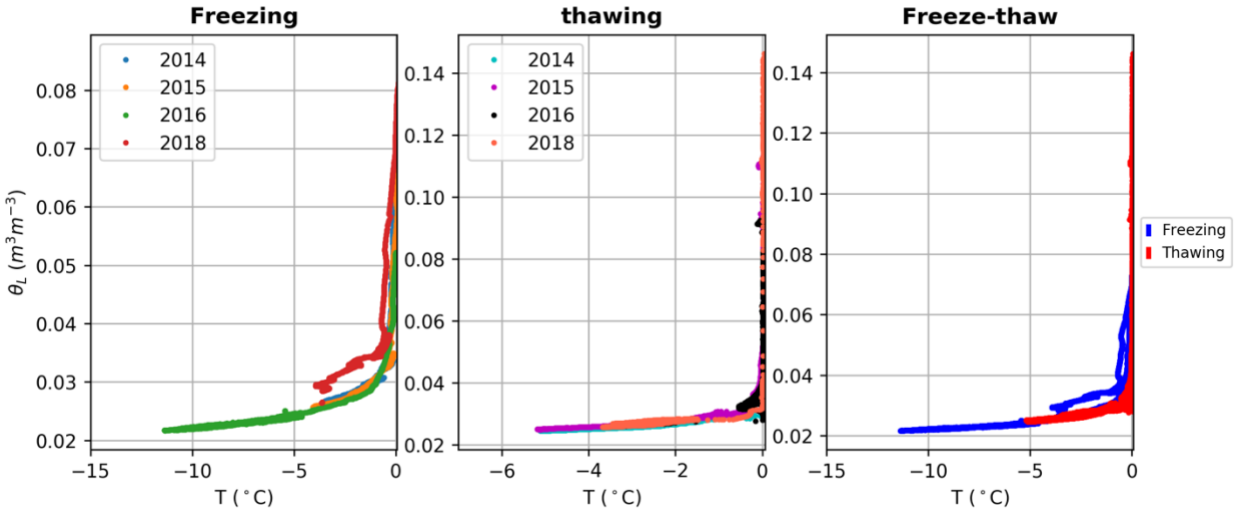

Figure 4-9: Soil freezing characteristic curves for the OJP site fitted to the VGN model

4.3 Comparing models with laboratory and field data sets

4.3.1 Comparing models with laboratory measured SFCs

The validation results for the three models (capillary, salt exclusion and the combined capillary salt models) using laboratory measured SFCs are presented in Figure 4-10. The 30 cm freezing data is used for this validation exercise since the shallower probes (5 cm and 15 cm probes) froze rapidly and were possibly not in thermodynamic equilibrium, and hence may overpredict the freezing point depression in the soil. However, the 30 cm probes were deep enough to have equilibrated before freezing commenced. Also, the θ_r for the lower moisture content treatments (0.00 $m^3\ m^{-3}$) were different from that which was obtained from the SMC (0.02 $m^3\ m^{-3}$), which may be due to errors in the measuring instrument especially under dry conditions in a coarse-textured soil. In such instances, θ_r was changed to 0.00 $m^3\ m^{-3}$. This adjustment was to allow the models to predict the entire range of values for the SFC and will not have any significant effect on the results presented here. Note also that salt concentrations were converted to mass of salt by multiplying by the liquid water content of the soil (θ_L). These masses of salt were then used in the model runs.

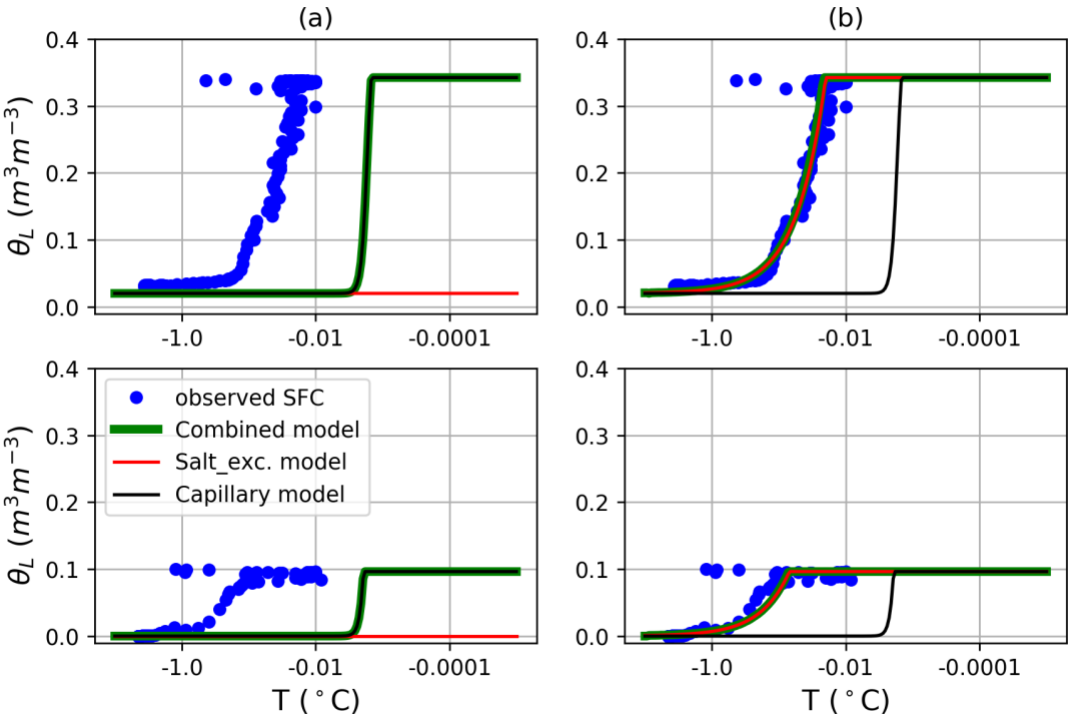

Figure 4-10: Performance of the three models (capillary, salt-exclusion and combined capillary salt models) against laboratory observed SFCs at 30 cm depth with no salt added: (a) with no salt in the models; and (b) with a residual amount (0.12 g) of salt added in the models. Upper panel is results for higher antecedent moisture content and lower panel is results for lower antecedent moisture content.

Figure 4-10 shows the performance of the three models versus the observed SFC without salt (Figure 4-10a) and with residual amount of salt added (Figure 4-10b). The results show that the capillary model which is based on the GCE underestimated freezing point depression in the experiments with no salt (Figure 4-10a). Also, the combined capillary salt model behaved just as the capillary model and the salt exclusion model did not work. In theory, the capillary model relates the SMC directly to the SFC through the GCE, so if the capillary model SFCs does not match the observations, as seen here, this either means there is a problem with the GCE model, or that there is a problem with how either (or both) the SMC or SFCs were measured. Lastly, despite our efforts to minimize solutes, the soil pore water may have contained non-negligible amounts of dissolved salts that may have resulted in higher depression of the freezing point in the SFCs. This was tested by adding different amounts of salt to the models and found that adding 0.12 g of salt gave excellent

results, as shown in Figure 4-10b. In this case, both the salt exclusion and combined capillary salt model performed very well to reproduce the observed SFCs (Figure 4-10b). Judging from how well the fit is in Figure 4-10b for both the salt exclusion and combined capillary salt models, the presence of dissolved salts seems to be a more credible explanation to why the capillary model underestimated freezing point depression in the soil.

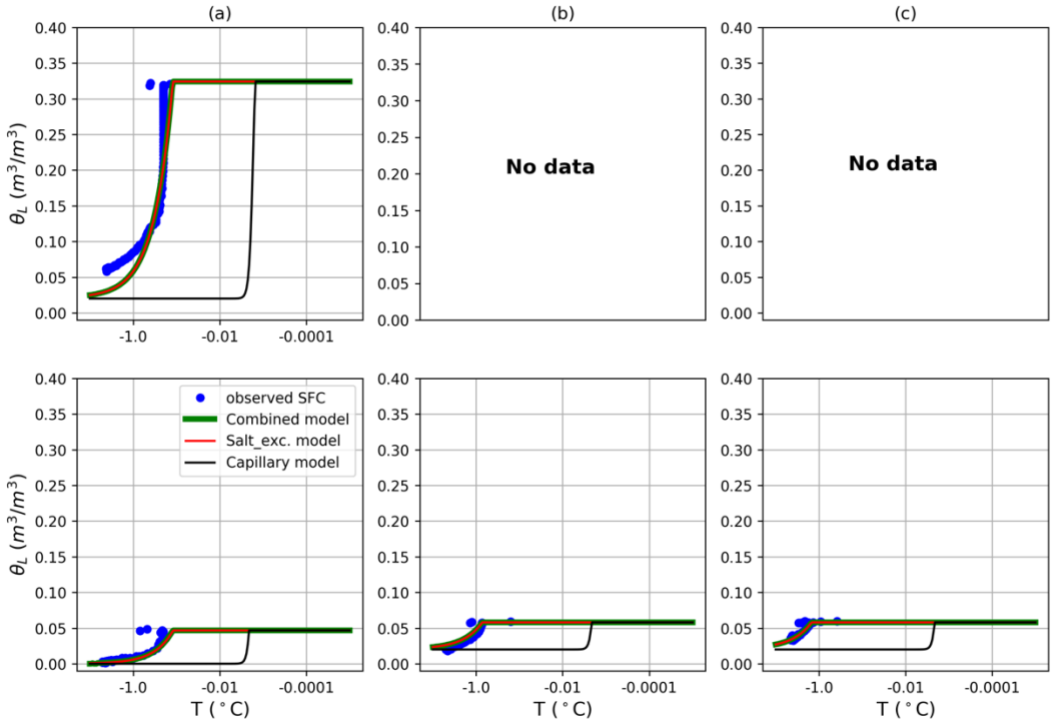

Figure 4-11: Performance of the three models (capillary, salt-exclusion and combined capillary salt models) against laboratory observed SFCs at 30 cm depth for different salt concentration a) 2 $g\ l^{-1}$ b) 8 $g\ l^{-1}$, and c) 16 $g\ l^{-1}$. Upper panel is results for higher antecedent moisture content and lower panel is results for lower antecedent moisture content.

For the experiments where a fixed concentration of NaCl salt was added (Figure 4-11), both the salt exclusion and the combined capillary salt models performed well without further calibration or refinement. The salt exclusion model does very well, which is interesting, especially because it is independent of the pore size distribution of the soil. One will argue that if the soils indeed had a residual amount of salt, then the actual salt concentrations in the saline experiments in Figure 4-11

will be higher than the 2 $g\ l^{-1}$, 8 $g\ l^{-1}$ and 16$g\ l^{-1}$ and that the model performances should not be that good. However, this is probably not so because the high salt concentrations masked the effect of the residual amount of salt (0.12 g). The capillary model underpredicted the amount of liquid moisture in the saline treatments (Figure 4-11) which is as expected because the model does not account for salts.

4.3.2 Comparing models with observed SFCs for the SDN site

Figure 4-12, 4-13, and 4-14 are the model validation results using observed data from the SDN site at 5 cm, 20 cm and 50 cm soil depths, respectively. Figure 4-12a, 4-13a, and 4-14a are the 2013 SMCs for the SDN URI 1 5 cm, 20 cm and 50 cm soil depths, respectively, fitted to the VGN model (these SMCs are the same as those presented in Figure 4-6 above). The parameter values (Table 4-2) for these SMCs were used in the model runs. In Figure 4-12b, 4-13b and 4-14b, the models were run without salts. The models were then run with an observed salt concentration for the site (Figure 4-12c, 4-13c, and 4-14c). The concentration of the various ions at the SDN site, as reported by Davies (2012) is shown in Table 4-4. Soil samples from the SDN site were analyzed in the laboratory for the various ions using an inductively coupled plasma emission spectrometry (Davies, 2012). Observations for hole A13 at a depth of 10 cm (3.55 $g\ l^{-1}$) was used for this particular model run. The reason for choosing this particular salt concentration is that it is closer to the soil moisture profile under study. Again, the observed salt concentration (3.55 $g\ l^{-1}$) was converted to equivalent masses of salt by multiplying with the observed moisture contents for the respective years and soil depths. Finally, Figure 4-12d, 4-13d, and 4-14d are the results after fitting the models to the observed data points by manually adjusting the salt masses. Note again that, here too, the residual moisture contents were adjusted where necessary to enable the models to predict the entire range of value for the SFC.

The results show that for all the soil depths, both the capillary and the combined capillary salt models underestimated freezing point depression in the no salt runs at the site (Figure 4-12b, 4-13b, and 4-14b) while the salt exclusion model did not work. This result is understandable because the SDN site has salts at least judging from Table 4-4 below, and since the capillary model cannot account for salts, it underestimated freezing point depression. Conversely, the combined capillary

salt model can account for the salts but since it was run without salts it behaved just like the capillary model. The salt exclusion model entirely depends on the mass of salt and will not apply to a no salt scenario. Also, except for the 50 cm depth (Figure 4-14c) where liquid water content was overestimated, both the salt exclusion and the combined capillary salt model were able to predict the observed SFCs closely when they were run with the observed salt masses (Figure 4-12c and Figure 4-13c). The overestimation of liquid water content at the 50 cm depth may be a proof that the soil here has less salt as compared to the shallower depths (5 cm and 20 cm). The observed salt concentration presented in Table 4-4 confirms this. From the table, salt concentration decreased with soil depth for the particular observation used in this study (A13-32.5 m from pond S107). Following the fitting, the performance of both the salt exclusion and the combined capillary salt model became even better (Figure 4-12d, 4-13d, and 4-14d). The salt masses used in the fitted runs for the SDN site are captured in Table 4-5 below. The capillary model failed in the two runs thus the runs with the observed salt masses (Figure 4-12c, 4-13c, and 4-14c) and in the fitting runs (Figure 4-12d, 4-13d and 4-14d) because in both runs salt was added to the model.

Table 4-4: Concentration of major cations at the SDN site in $g\ l^{-1}$ (after Davies, 2012)

Hole	Depth (cm)	Cl	Ca	K	Mg	Na	S	Total salt
A2 - 2.5m from S107	10	0.0061	0.158	0.034	0.051	0.0087	0.243	0.5008
	35	0.0066	0.0955	0.0154	0.0371	0.0084	0.102	0.265
	50	0.0078	0.0906	0.0172	0.0439	0.0099	0.209	0.3784
A9 - 22.5m from S107	30	0.0076	0.261	0.0115	0.239	0.0959	1.42	2.035
	60	0.0047	0.559	0.0157	0.237	0.045	2.28	3.1414
	100	0.0054	0.565	0.0123	0.106	0.0306	1.76	2.4793
A13 - 32.5m from S107	10	0.03	0.388	0.0404	0.452	0.129	2.51	3.5494
	40	0.0045	0.103	0.0075	0.107	0.0653	0.58	0.8673
	60	0.0081	0.0968	0.0102	0.0669	0.062	0.417	0.661

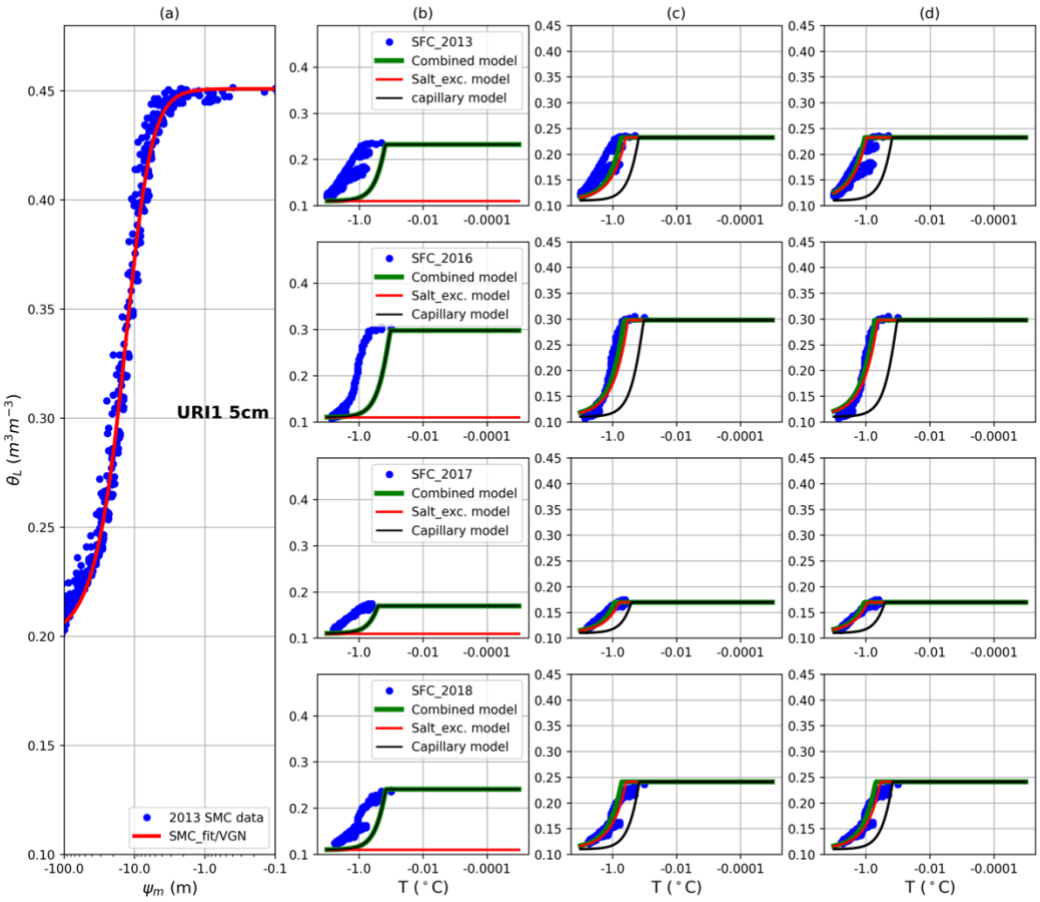

Figure 4-12: Performance of the three models (capillary, salt-exclusion and combined capillary salt models) against observed SFCs for SDN URI 1 at 5 cm depth, (a) fitted soil moisture characteristic curves (b) models applied without salt c) models run with the observed salt mass d) model fitted by adjusting the salt masses

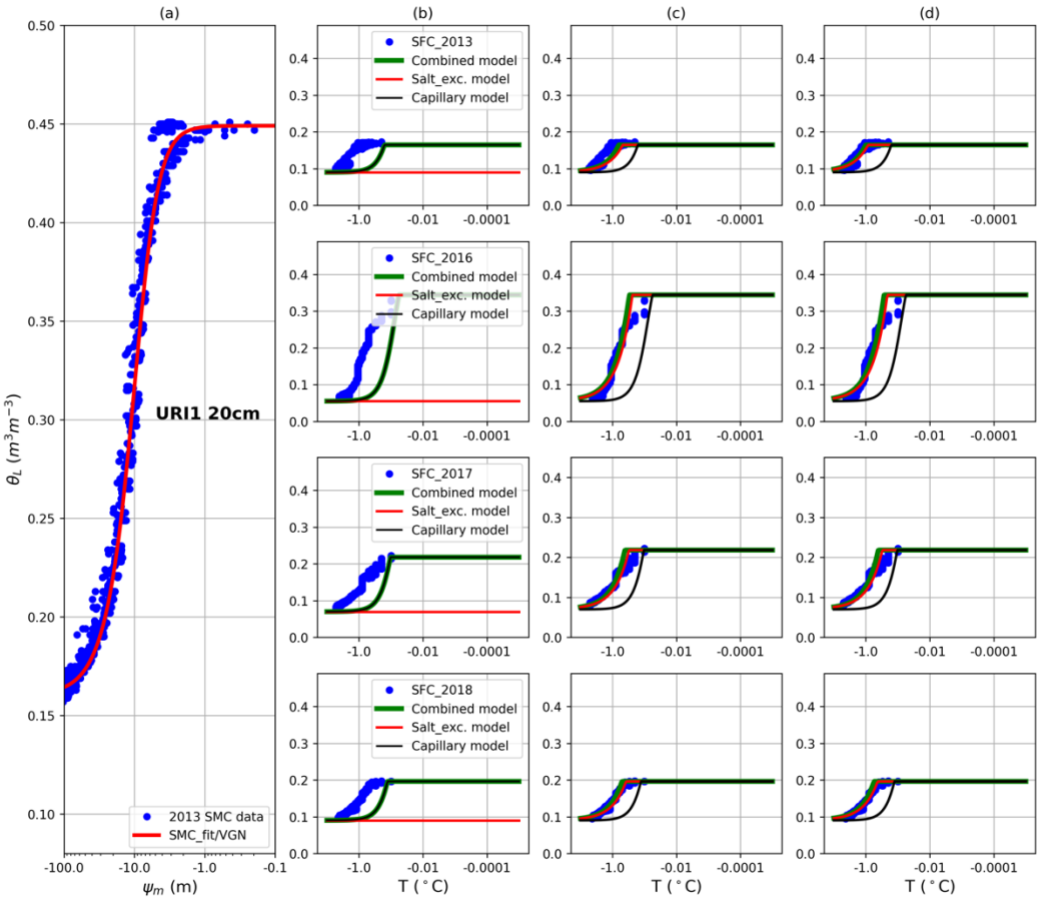

Figure 4-13: Performance of the three models (capillary, salt-exclusion and combined capillary salt models) against observed SFCs for SDN URI 1 at 20 cm depth, (a) fitted soil moisture characteristic curves (b) models applied without salt c) models run with observed salt masses d) model fitted by adjusting the salt masses.

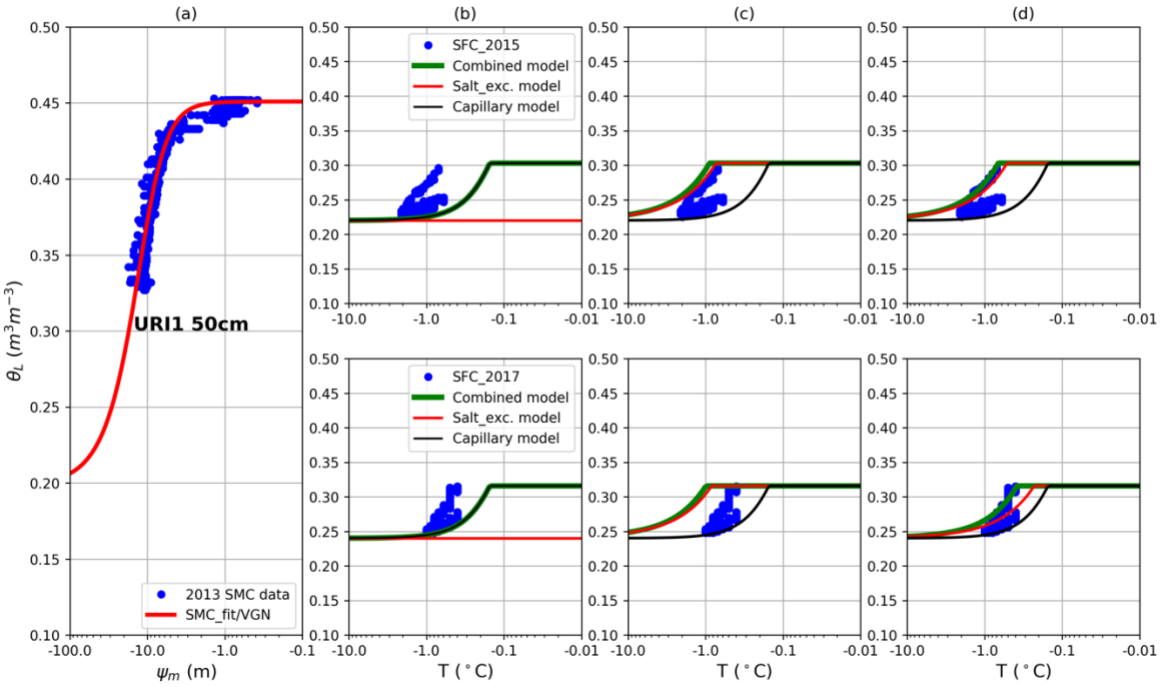

Figure 4-14: Performance of the three models (capillary, salt-exclusion and combined capillary salt models) against observed SFCs for SDN URI 1 at 50 cm depth, (a) fitted soil moisture characteristic curves (b) models applied without salt c) models run with observed salt masses d) model fitted by adjusting the salt masses.

Table 4-5: Amount of salt in grams (g) used in the unfitted (runs with observed salt masses) and the fitting runs for the SDN site. For the unfitted runs, the salt masses were calculated from the observed salt concentration of 3.5 $g\ l^{-1}$ for the different soil depths.

Year	Unfitted runs	Fitting runs
URI 1, 5cm		
2013	0.84	2
2016	1.08	1.4
2017	0.64	0.9
2018	0.85	0.8
URI 1 20 cm		
2013	0.62	1.1
2016	1.22	1.1
2017	0.8	0.8
2018	0.7	0.8
URI 1 50 cm		
2015	1.07	0.75
2017	1.1	0.31

4.3.3 Comparing models with observed SFCs for the OJP site

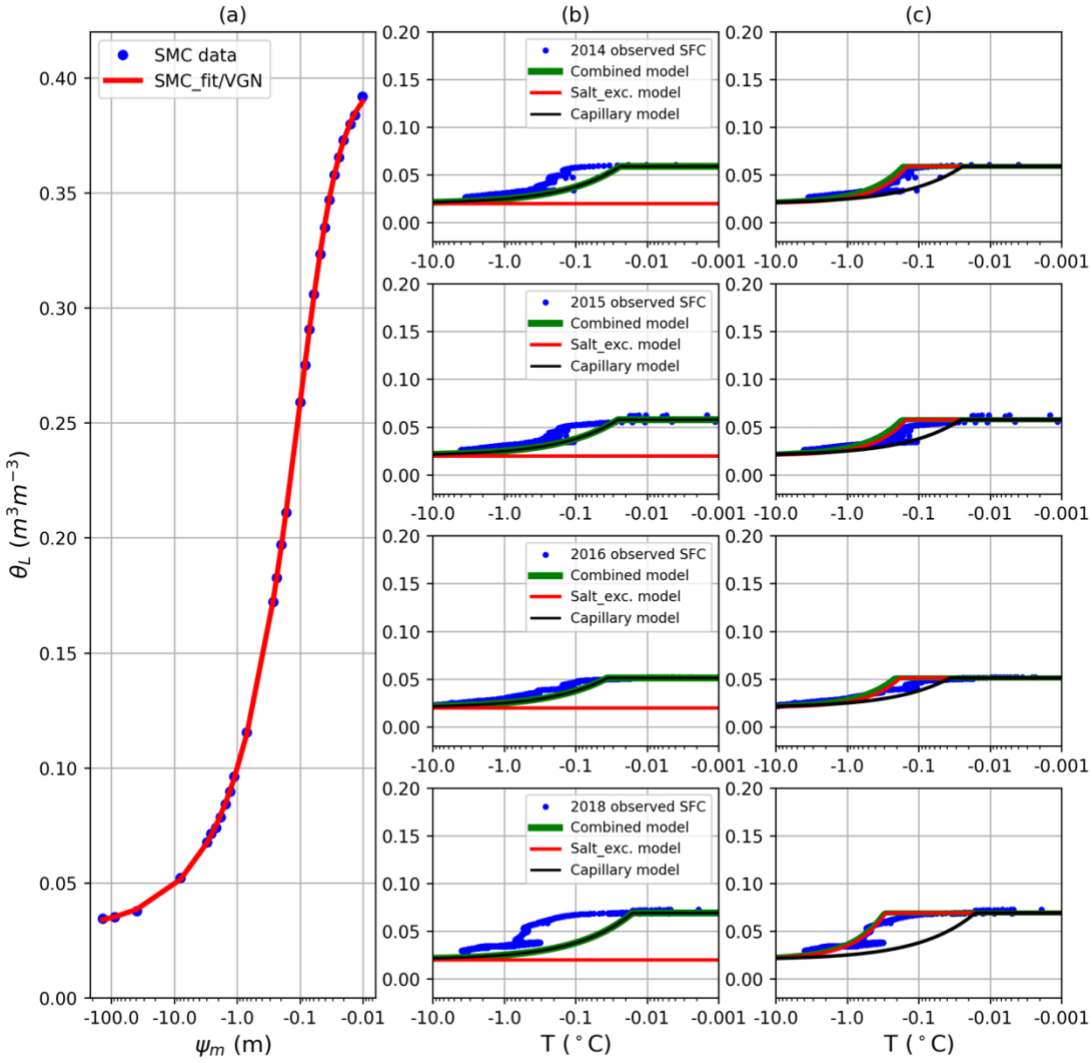

Figure 4-15: Performance of the three models (capillary, salt-exclusion and combined capillary salt models) with observed SFCs at the OJP site, (a) fitted soil moisture characteristic curve (b) models applied without salt c) models fitted by adding some salts.

Figure 4-15 is the summary of the performance of the three models at the OJP site first without salt (Figure 4-15b) and after curve fitting (Figure 4-15c) by adding arbitrary amounts of salt. Here the unfitted runs (running the model with observed salt masses) were not performed. This is because the observed salt concentration for the OJP site was not known. The masses of salt used in the fitted runs for this site is shown in Table 4-6. Again, the results show that the capillary model could not predict the observations at the site in the no salt runs (Figure 4-15b). The reason for this underestimation is the same as speculated earlier in the SDN validations, the presence of salt. However, the underestimation here is smaller than at the SDN site (compare Figure 4-15b to Figure 4-12b, 4-13b, and 4-14b). Comparing the salt masses used in the fitting run for the OJP site (Table 4-6) to those used in the SDN (Table 4-5), it is obvious that the SDN site has more salt than the OJP soil hence this result. Again, after fitting, the performance of both the salt exclusion and the combined capillary salt models improved significantly (Figure 4-15b).

Table 4-6: Amount of salt in grams added to the OJP soil in the fitting runs

Year	2014	2015	2016	2018
Salt mass (g)	0.1	0.1	0.1	0.25

CHAPTER 5

CONCLUSIONS

In this thesis, both observed data from the laboratory and field as well as models were used to gain an understanding of freezing point depression and to improve the prediction of liquid water content in frozen soils.

In the laboratory, the SMC of a silica sand was measured using a HYPROP apparatus. The results showed that the soil has poor water retention ability and drains rapidly due to its large pore sizes. The SFC of the same sand was measured using a series of column experiments with controlled total water content and pore-water salinity. The experiments were successful in producing well-defined SFCs that matched expectations, where the form of the decrease in liquid water content with temperature was similar to the form of the SMC. Increasing the salinity resulted in enhanced freezing point depression, again as was expected. The observed SFCs were hysteretic, with the freezing curves having more liquid water than the thawing curves at the same temperature. There was also evidence of moisture migration during soil freezing which is attributed to cryosuction: during freezing, high hydraulic gradients are established in the soil resulting in the upward movement of water from the unfrozen areas beneath the freezing front to the freezing front (Hansson et al., 2004), where the water refreezes.

Data were collected from established seasonally frozen field sites in the prairies (SDN site) and the boreal forest (OJP site) in Saskatchewan, Canada. The field results showed that the SMCs for the SDN site were different for different years, which may be due to changes in soil properties as a result of the shrinking and expansion of the soil as well as the shifting of measuring instruments. Just as seen with the SFCs of the silica sand measured in the laboratory, the SFCs for the SDN and OJP sites are hysteretic. Further, the freezing curves of the SDN and OJP soils were not fully saturated at the start of freezing. This is because the soils had a dry antecedent moisture condition

prior to freezing. The thawing curve of the field soils, however, ends in a very wet condition, which may be due to either or both snowmelt infiltration and cryosuction. Based on the observed SFCs from the field and laboratory, the freezing and thawing process in soils can be conceptualized, as shown in Figure 5-1 below. The conceptual figure shows that the freezing temperature of soil pore water is depressed. As discussed earlier, the depression of the freezing point of liquid water in frozen soils is due to both salts and the capillary effect. Figure 5-1 also depicts the hysteretic nature of the SFC: the freezing curve has higher liquid water content at the same temperature than the thawing curves. Lastly, Figure 5-1 shows that the soil has a higher moisture content after thawing than it had before freezing, as seen in the field experiment. This is suspected to be due to either or both snowmelt infiltration and cryosuction as discussed earlier.

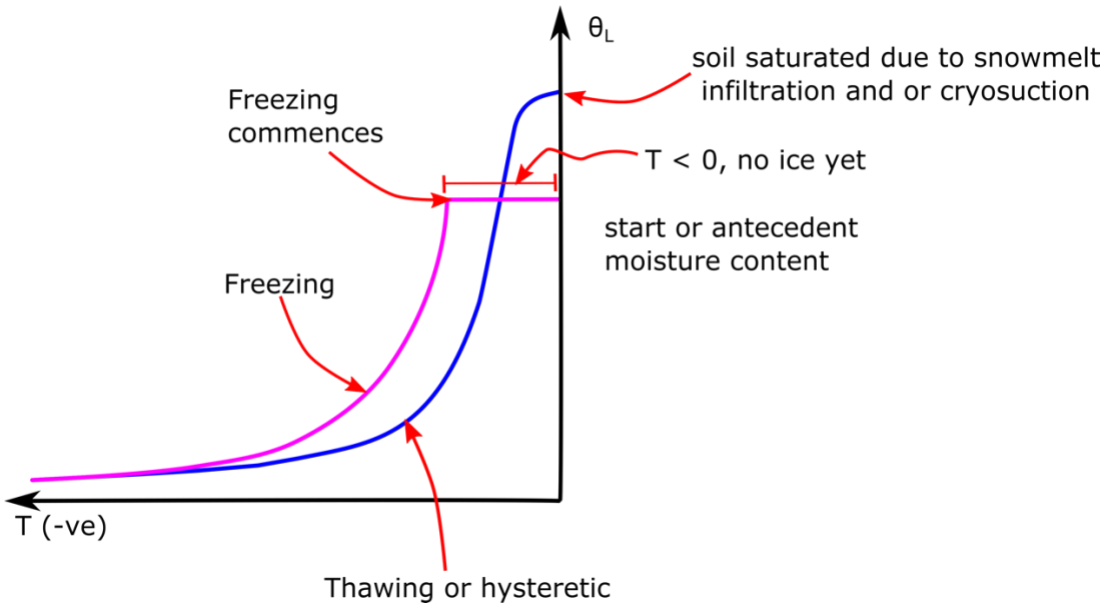

Figure 5-1: Conceptual diagram depicting the difference between freezing and thawing in frozen soils

In the modelling studies, three alternative models were developed to explain the SFC: 1) the capillary model which is based on the GCE and assumes no salt condition in soils; 2) the salt exclusion model which is based solely on the salt concentration and; 3) the combined capillary salt model which accounts for both the effect of salt and capillary force on the SFC. In the absence of

salt, the capillary model and the combined capillary model are the same while the salt exclusion model predicts no freezing point depression at all – that is all of the water freezes at 0 ℃. At high salt concentrations, the salt exclusion and the combined capillary salt models perform the same. Nevertheless, when the amount of salt in the soil is small, the combined capillary salt model predicts more liquid water in a frozen soil at the same temperature, than the salt exclusion model.

In applying the models, the capillary model underestimated the liquid water content of the laboratory silica sand even in the salt-free experiments. This is hypothesized, to be because the silica sand has a residual amount of salt. Meanwhile, in the same salt-free experiments, the combined capillary salt model behaved just like the capillary model while the salt exclusion model did not work. However, upon adding a residual amount of salt to both models (salt exclusion and combined capillary salt models), they were able to fit the observed SFCs. Similarly, in the laboratory experiments with a specified amount of salt added, both the salt exclusion and the combined capillary salt models did well with no calibration or refinement. In the field experiments, the capillary model underestimated liquid water content under the no salt-runs. This is because the field soils had some salt, especially the SDN site, which has been shown to have significant amounts of salt. However, when known amounts of salt were added to the models, both the salt exclusion and combined capillary salt model were able to predict liquid water content very closely. The performances of the two models were made even better by adjusting the amount of salt. These results suggest that salinity is a dominant control on the SFC in real soils and that the combined capillary salt model is the most realistic of the three models considered here. However, because it is intractable, requiring an iterative solution, this model, in its current form, might be impractical in hydrological models. The combined capillary salt model can be applied to a soil where the salinity is known, or where the salt concentration is not known; this can be treated as a parameter to fit these models to observed SFCs. This could be done in a conventional manner, that is either by trial and error or optimization. The outcome is that one additional parameter is needed (the salt concentration) to parameterize the hydraulic properties of a frozen soil, as compared with an unfrozen soil. In model applications where the salt concentration is also modelled, this can be used directly to determine the SFC, and no additional parameters are required. Notwithstanding, the salt exclusion model has its advantage; that is, it is tractable and can be used successfully in highly

saline soils. Lastly, the capillary model may be used but only in a salt-free soil. The only problem is that a completely salt-free soil may not exist in natural environments.

In summary, this research has provided an empirical and conceptual understanding of freezing point depression in frozen soil and the effect of salt on the SFC. These are keen insights that can help improve the capacity of cold region models in predicting cold climate hydrological processes and events more accurately. Future studies on this topic should focus on 1) finding an improved mathematical solution procedure for the combined capillary salt model and 2) further testing of the new models at different field sites to consolidate understanding of their behavior and performance.

REFERENCES

Almeida, E. L. de, Teixeira, A. dos S., Silva Filho, F. C. da, Assis Júnior, R. N. de, Leão, R. A. de O., Almeida, E. L. de, Teixeira, A. dos S., Silva Filho, F. C. da, Assis Júnior, R. N. de, & Leão, R. A. de O. (2015). Filter paper method for the determination of the soil water retention curve. *Revista Brasileira de Ciência Do Solo*, *39*(5), 1344–1352. https://doi.org/10.1590/01000683rbcs20140546

Anderson, G. M. (2005). Thermodynamics of natural systems (2nd ed.). Cambridge University Press.

Appels, W. M., Coles, A. E., & McDonnell, J. J. (2018). Infiltration into frozen soil: From core-scale dynamics to hillslope-scale connectivity. *Hydrological Processes*, *32*(1), 66–79. https://doi.org/10.1002/hyp.11399

Azmatch, T. F., Sego, D. C., Arenson, L. U., & Biggar, K. W. (2012). Using soil freezing characteristic curve to estimate the hydraulic conductivity function of partially frozen soils. *Cold Regions Science and Technology*, *83–84*, 103–109. https://doi.org/10.1016/j.coldregions.2012.07.002

Bam, E. K. P., Brannen, R., Budhathoki, S., Ireson, A. M., & Spence, C. (2019). Meteorological, soil moisture, surface water, and groundwater data from the St. Denis National Wildlife Area, Saskatchewan, Canada. 11. *Earth System Science Data Discussions* (pp 1-21). https://doi.org/10.5194/essd-2018-125

Bam, E. K. P., & Ireson, A. M. (2019). Quantifying the wetland water balance: A new isotope-based approach that includes precipitation and infiltration. *Journal of Hydrology*, *570*, 185–200. https://doi.org/10.1016/j.jhydrol.2018.12.032

Barr, A. G., van der Kamp, G., Black, T. A., McCaughey, J. H., & Nesic, Z. (2012). Energy balance closure at the BERMS flux towers in relation to the water balance of the White Gull Creek watershed 1999–2009. *Agricultural and Forest Meteorology*, *153*, 3–13. https://doi.org/10.1016/j.agrformet.2011.05.017

Bing, H., & Ma, W. (2011). Laboratory investigation of the freezing point of saline soil. *Cold Regions Science and Technology*, *67*(1), 79–88. https://doi.org/10.1016/j.coldregions.2011.02.008

Bitelli, M., Flury, M., & Campbell, G. S. (2003). A thermodielectric analyzer to measure the freezing and moisture characteristic of porous media. *Water Resources Research*, *39*(2). https://doi.org/10.1029/2001WR000930

Bittelli, M. (2010). Measuring soil water potential for water management in agriculture: A Review. *Sustainability*, *2*(5), 1226–1251. https://doi.org/10.3390/su2051226

Braudeau, E., Hovhannissian, G., Assi, A. T., & Mohtar, R. H. (2014). Soil water thermodynamic to unify water retention curve by pressure plates and tensiometer. *Frontiers in Earth Science*, *2*. https://doi.org/10.3389/feart.2014.00030

Breitmeyer, R. J., & Fissel, L. (2017). Uncertainty of soil water characteristic curve measurements using an automated evaporation technique. *Vadose Zone Journal*, *16*(13), vzj2017.07.0136. https://doi.org/10.2136/vzj2017.07.0136

Budhathoki, S. 1989-. (2018). Modelling snowmelt infiltration processes in seasonally frozen ground [Thesis, University of Saskatchewan]. https://harvest.usask.ca/handle/10388/8468

Bulut, R., & Leong, E. C. (2008). Indirect Measurement of Suction. *Geotechnical and Geological Engineering*, *26*(6), 633. https://doi.org/10.1007/s10706-008-9197-0

Caicedo, B. (2017). Physical modelling of freezing and thawing of unsaturated soils. *Géotechnique*, *67*(2), 106–126. https://doi.org/10.1680/jgeot.15.P.098

Campbell, G. S. (1988). Soil water potential measurement: An overview. *Irrigation Science*, *9*(4), 265–273.

Campbell Scientific, Inc.: 229 Heat dissipation matric water potential sensor instruction manual, revision: 5/09, 2009.

Cheng, Q., Sun, Y., Jones, S. B., Vasilyev, V. I., Popov, V. V., Wang, G., & Zheng, L. (2014). In situ measured and simulated seasonal freeze–thaw cycle: A 2-year comparative study between layered and homogeneous field soil profiles. *Journal of Hydrology*, *519*, 1466–1473.

https://doi.org/10.1016/j.jhydrol.2014.09.023

Christensen, A. F., He, H., Dyck, M. F., Lenore Turner, E., Chanasyk, D. S., Naeth, M. A., & Nichol, C. (2013). In situ measurement of snowmelt infiltration under various topsoil cap thicknesses on a reclaimed site. *Canadian Journal of Soil Science*, *93*(4), 497–510. https://doi.org/10.4141/cjss2012-048

Clark, G. A. (1990). Measurement of soil water potential. *HortScience*, *25*(12), 1548–1551. https://doi.org/10.21273/HORTSCI.25.12.1548

Cresswell, H. P., Green, T. W., & McKenzie, N. J. (2008). The adequacy of pressure plate apparatus for determining soil water retention. *Soil Science Society of America Journal*, *72*(1), 41. https://doi.org/10.2136/sssaj2006.0182

Cuenca, R. H., Stangel, D. E., & Kelly, S. F. (1997). Soil water balance in a boreal forest. *Journal of Geophysical Research: Atmospheres*, *102*(D24), 29355–29365. https://doi.org/10.1029/97JD02312

Davies, S.R. (2012). The Hydrological behaviour of Canadian prairie wetlands under changing climatic conditions: during wet summers [Master's Thesis, Imperial College of London, UK].

Day, A. D., & Ludeke, K. L. (1993). Soil moisture. In A. D. Day & K. L. Ludeke (Eds.), *Plant Nutrients in Desert Environments* (pp. 19–22). Springer Berlin Heidelberg. https://doi.org/10.1007/978-3-642-77652-6_5

Dey, P., Sundriyal, P., & Sahoo, S. K. (2017). Science of lagging behind- hysteresis in soil moisture characteristic curve - A review. *International Journal of Current Microbiology and Applied Sciences*, *6*(10), 151–156. https://doi.org/10.20546/ijcmas.2017.610.019

Elder, A. N., & Rasmussen, T. C. (1994). Neutron probe calibration in unsaturated tuff. *Soil Science Society of America Journal*, *58*(5), 1301–1307. https://doi.org/10.2136/sssaj1994.03615995005800050004x

Flerchinger, G. N., Seyfried, M. S., & Hardegree, S. P. (2006). Using soil freezing characteristics to model multi-season soil water dynamics. *Vadose Zone Journal*, *5*(4), 1143. https://doi.org/10.2136/vzj2006.0025

Francisca, F. M., & Montoro, M. A. (2012). Measuring the dielectric properties of soil–organic mixtures using coaxial impedance dielectric reflectometry. *Journal of Applied Geophysics*, *80*, 101–109. https://doi.org/10.1016/j.jappgeo.2012.01.011

Grewal, K. S., Buchan, G. D., & Tonkin, P. J. (1990). Estimation of field capacity and wilting point of some New Zealand soils from their saturation percentages. *New Zealand Journal of Crop and Horticultural Science*, *18*(4), 241–246. https://doi.org/10.1080/01140671.1990.10428101

Guan, X. J., Westbrook, C. J., & Spence, C. (2010). Shallow soil moisture – ground thaw interactions and controls – Part 1: Spatiotemporal patterns and correlations over a subarctic landscape. *Hydrology and Earth System Sciences*, *14*(7), 1375–1386. https://doi.org/10.5194/hess-14-1375-2010

Haghighi, H., Chapoy, A., & Tohidi, B. (2008). Freezing point depression of electrolyte solutions: Experimental measurements and modeling using the cubic-plus-association equation of state. *Industrial & Engineering Chemistry Research*, *47*(11), 3983–3989. https://doi.org/10.1021/ie800017e

Hansson, K., Šimůnek, J., Mizoguchi, M., Lundin, L.-C., & Genuchten, M. T. van. (2004). Water flow and heat transport in frozen soil: Numerical solution and freeze–thaw applications. *Vadose Zone Journal*, *3*(2), 693–704. https://doi.org/10.2136/vzj2004.0693

Hayashi, M. (2013). The cold vadose zone: Hydrological and ecological significance of frozen-soil processes. *Vadose Zone Journal*, *12*(4), 0. https://doi.org/10.2136/vzj2013.03.0064

Hayashi, M., van der Kamp, G., & Rosenberry, D. O. (2016). Hydrology of prairie wetlands: Understanding the integrated surface-water and groundwater processes. *Wetlands*, *36*(S2), 237–254. https://doi.org/10.1007/s13157-016-0797-9

Hayashi, M., van der Kamp, G., & Rudolph, D. L. (1998). Water and solute transfer between a prairie wetland and adjacent uplands, 2. Chloride cycle. *Journal of Hydrology*, *207*(1–2), 56–67. https://doi.org/10.1016/S0022-1694(98)00099-7

He, H., Dyck, M., Zhao, Y., Si, B., Jin, H., Zhang, T., Lv, J., & Wang, J. (2016). Evaluation of five composite dielectric mixing models for understanding relationships between effective permittivity and unfrozen water content. *Cold Regions Science and Technology*, *130*, 33–42. https://doi.org/10.1016/j.coldregions.2016.07.006

Hohmann, M. (1997). Soil freezing — the concept of soil water potential. State of the art. *Cold Regions Science and Technology*, *25*(2), 101–110. https://doi.org/10.1016/S0165-232X(96)00019-5

Holten, R., Bøe, F. N., Almvik, M., Katuwal, S., Stenrød, M., Larsbo, M., Jarvis, N., & Eklo, O. M. (2018). The effect of freezing and thawing on water flow and MCPA leaching in partially frozen soil. *Journal of Contaminant Hydrology*, *219*, 72–85. https://doi.org/10.1016/j.jconhyd.2018.11.003

Hong, W.-T., Jung, Y.-S., Kang, S., & Lee, J.-S. (2016). Estimation of soil-water characteristic curves in multiple-cycles using membrane and TDR system. *Materials*, *9*(12). https://doi.org/10.3390/ma9121019

Iiyama, I. (2016). Differences between field-monitored and laboratory-measured soil moisture characteristics. *Soil Science and Plant Nutrition*, *62*(5–6), 416–422. https://doi.org/10.1080/00380768.2016.1242367

Ireson, A. M., Barr, A. G., Johnstone, J. F., Mamet, S. D., Van Der Kamp, G., Whitfield, C. J., Michel, N. L., North, R. L., Westbrook, C. J., Debeer, C., Chun, K. P., Nazemi, A., & Sagin, J. (2015). The changing water cycle: The boreal plains ecozone of Western Canada. *Wiley Interdisciplinary Reviews: Water*, *2*(5), 505–521. https://doi.org/10.1002/wat2.1098

Irwin. Remson. (1962). Review of some elements of soil-moisture theory. *Geological survey professional paper 411-D. US Govt. Printing Office. Washington, USA.* https://pubs.usgs.gov/pp/0411d/report.pdf

Kelleners, T. J., & Norto, J. B. (2012). Determining water retention in seasonally frozen soils using hydra impedance sensors. *Soil Science Society of America Journal*, *76*(1), 36. https://doi.org/10.2136/sssaj2011.0222

Kim, Y., Chae, D., Kim, K., & Cho, W. (2016). Physical and mechanical characteristics of frozen ground at various sub-zero temperatures. *KSCE Journal of Civil Engineering*, *20*(6), 2365–2374. https://doi.org/10.1007/s12205-015-0542-6

Kong, B., Xia, F., Yu, B., Xia, T., & Ding, Z. (2020). Pore size changes in marine soft soil under various freezing conditions. *Journal of Marine Science and Engineering*, *8*(3), 170. https://doi.org/10.3390/jmse8030170

Koopmans, R. W. R., & Miller, R. D. (1966). Soil freezing and soil water characteristic curves. *Soil Science Society of America Journal*, *30*(6), 680–685.

Kozlowski, T. (2009). Some factors affecting supercooling and the equilibrium freezing point in soil–water systems. *Cold Regions Science and Technology*, *59*(1), 25–33. https://doi.org/10.1016/j.coldregions.2009.05.009

Kreba, S. A., & Maule, C. P. (2010). Estimating vertical soil water fluxes with tracers and time domain reflectometry (TDR) in a sand column under controlled laboratory conditions. *Canadian Biosystems Engineering*, *52*, 9.

Kurylyk, B. L., & Watanabe, K. (2013). The mathematical representation of freezing and thawing processes in variably saturated, non-deformable soils. *Advances in Water Resources*, *60*, 160–177. https://doi.org/10.1016/j.advwatres.2013.07.016

LeBlanc, F. (2017). Laboratory investigation of infiltration processes in frozen soil and the influence of antecedent moisture content and macroporosity. http://dx.doi.org/10.11575/PRISM/26710

Lewis, J., & Sjöstrom, J. (2010). Optimizing the experimental design of soil columns in saturated and unsaturated transport experiments. *Journal of Contaminant Hydrology*, *115*(1–4), 1–13. https://doi.org/10.1016/j.jconhyd.2010.04.001

Malaya, C., & Sreedeep, S. (2012). Critical Review on the Parameters Influencing Soil-Water Characteristic Curve. *Journal of Irrigation and Drainage Engineering*, *138*(1), 55–62. https://doi.org/10.1061/(ASCE)IR.1943-4774.0000371

Maulé, C. P., & Gray, D. M. (1994). Estimated snowmelt infiltration and runoff for the prairie provinces. *Canadian Water Resources Journal*, *19*(3), 253–265. https://doi.org/10.4296/cwrj1903253

Miller, R. D. (1980). Freezing phenomena in soils. In *Freezing phenomena in soils* (pp. 254–299). *Academic*. New York, USA.

Mizoguchi, M. (1990). Water, heat and salt transport in freezing soil [Ph.D. thesis In Japanese, University of Tokyo, Japan].

Mohammed, A. A., Kurylyk, B. L., Cey, E. E., & Hayashi, M. (2018). Snowmelt Infiltration and macropore flow in frozen soils: Overview, knowledge gaps, and a conceptual framework. *Vadose Zone Journal*, *17*(1). https://doi.org/10.2136/vzj2018.04.0084

Nachshon, U., Ireson, A., van der Kamp, G., Davies, S. R., & Wheater, H. S. (2014). Impacts of climate variability on wetland salinization in the North American prairies. *Hydrology and Earth System Sciences*, *18*(4), 1251–1263. https://doi.org/10.5194/hess-18-1251-2014

Nagare, R. M., Schincariol, R. A., Quinton, W. L., & Hayashi, M. (2011). Effects of freezing on soil temperature, freezing front propagation and moisture redistribution in peat: laboratory investigations. *Hydrology Earth System Science Journal, 6(2):501–515.* https://doi.org/10.5194/hess-16-501-2012

Nazarbakhsh, M., Ireson, A. M., & Barr, A. G. (2020). Controls on evapotranspiration from jack pine forests in the Boreal Plains Ecozone. *Hydrological Processes*, *34*(4), 927–940. https://doi.org/10.1002/hyp.13674

Oliviera, I. B. (Universidade F. da B., Demond, A. H., & Salehzadeh, A. (1996). Packing of sands for the production of homogeneous porous media. *Soil Science Society of America Journal, 60 (1), 49–53.* http://agris.fao.org/agris-search/search.do?recordID=US9608609

Öquist, M. G., Sparrman, T., Klemedtsson, L., Drotz, S. H., Grip, H., Schleucher, J., & Nilsson, M. (2009). Water availability controls microbial temperature responses in frozen soil CO2 production. *Global Change Biology*, *15*(11), 2715–2722. https://doi.org/10.1111/j.1365-2486.2009.01898.x

Parsons, D. F., Hayashi, M., & Kamp, G. van der. (2004). Infiltration and solute transport under a seasonal wetland: bromide tracer experiments in Saskatoon, Canada. *Hydrological Processes*, *18*(11), 2011–2027. https://doi.org/10.1002/hyp.1345

Patterson, D. E., & Smith, M. W. (1985). Unfrozen water content in saline soils: results using time-domain reflectometry. *Canadian Geotechnical Journal*, *22*(1), 95–101.

Pekrioglu Balkis, A. (2019). Determination of SWRC for unsaturated sands, comparative study – Filter paper method versus hanging column technique. *European Journal of Science and Technology*, (16), 403–413. https://doi.org/10.31590/ejosat.539620

Peng, W., Lu, Y., Xie, X., Ren, T., & Horton, R. (2019). An Improved Thermo-TDR Technique for Monitoring Soil Thermal Properties, Water Content, Bulk Density, and Porosity. *Vadose Zone Journal*, *18*(1), 190026. https://doi.org/10.2136/vzj2019.03.0026

Pham, H., & Fredlund, D. (2005). A study of hysteresis models for soil-water characteristic curves. *Canadian Geotechnical Journal*, *42*(6), 1548–1568. https://doi.org/10.1139/T05-071

Pires, L. F., Brinatti, A. M., & Saab, S. da C. (2015). Experimental Method to Determine Some Physical Properties in Physics Classes. *Revista Brasileira de Ciência Do Solo*, *39*(5), 1507–1512. https://doi.org/10.1590/01000683rbcs20140766

Qi, Z., Jingfang, S., & Wenwei, L. (2018). A survey about characteristics of soil water retention curve. *IOP Conference Series: Earth and Environmental Science*, *153*, 062076. https://doi.org/10.1088/1755-1315/153/6/062076

Ren, J., & Vanapalli, S. K. (2018). Prediction of resilient modulus of frozen unbound road materials using soil-freezing characteristic curve. *Canadian Geotechnical Journal*, *55*(8), 1200-. Gale Academic OneFile Select.

Ren, J., & Vanapalli, S. K. (2019). Comparison of soil-freezing and soil-water characteristic curves of two Canadian soils. *Vadose Zone Journal*, *18*(1). https://doi.org/10.2136/vzj2018.10.0185

Ren, J., & Vanapalli, S. K. (2020). Effect of freeze–thaw cycling on the soil-freezing characteristic curve of five Canadian soils. *Vadose Zone Journal*, *19*(1), e20039. https://doi.org/10.1002/vzj2.20039

Richards, L. A., & Fireman, M. (1943). Pressure-plate apparatus for measuring moisture sorption and transmission by soils. *Soil Science*, *56*(6), 395–404.

Ridley, A. M., & Burland, J. B. (1993). A new instrument for the measurement of soil moisture suction. *Géotechnique*, *43*(2), 321–324. https://doi.org/10.1680/geot.1993.43.2.321

Rohatgi, A. (2015). *WebPlotDigitizer User Manual Version 3.9*. 23.

Romano, N. (2014). Soil moisture at local scale: Measurements and simulations. *Journal of Hydrology*, *516*, 6–20. https://doi.org/10.1016/j.jhydrol.2014.01.026

Roth, K., Schulin, R., Flühler, H., & Attinger, W. (1990). Calibration of time domain reflectometry for water content measurement using a composite dielectric approach. *Water Resources Research*, *26*(10), 2267–2273. https://doi.org/10.1029/WR026i010p02267

Schjønning, P., McBride, R. A., Keller, T., & Obour, P. B. (2017). Predicting soil particle density from clay and soil organic matter contents. *Geoderma*, *286*, 83–87. https://doi.org/10.1016/j.geoderma.2016.10.020

Schmugge, T. J., Jackson, T. J., & McKim, H. L. (1980). Survey of methods for soil moisture determination. *Water Resources Research*, *16*(6), 961–979. https://doi.org/10.1029/WR016i006p00961

Seyfried, M. S., & Murdock, M. D. (2004). Measurement of soil water content with a 50-MHz soil dielectric sensor. *Soil Science Society of America Journal*, *68*(2), 394–403. https://doi.org/10.2136/sssaj2004.3940

Silva, B. M., Silva, É. A. da, Oliveira, G. C. de, Ferreira, M. M., & Serafim, M. E. (2014). Plant-available soil water capacity: estimation methods and implications. *Revista Brasileira de Ciência Do Solo*, *38*(2), 464–475. https://doi.org/10.1590/S0100-06832014000200011

Spaans, Egbert J. A., & Baker, J. M. (1995). Examining the use of time domain reflectometry for measuring liquid water content in frozen soil. *Water Resources Research, 31*(12), 2917–2925. https://doi.org/10.1029/95WR02769

Spaans, E.J.A. (1994). The soil freezing characteristic: Its measurement and similarity to the soil moisture characteristic [PhD thesis, University of Michigan].

Spaans, E.J.A., & Baker, J. M. (1996). The soil freezing characteristic: Its measurement and similarity to the soil moisture characteristic. *Soil Sci. Soc. Am. J., 60*, 13–19.

Stähli, M., & Stadler, D. (1997). Measurement of water and solute dynamics in freezing soil columns with time domain reflectometry. *Journal of Hydrology, 195*(1–4), 352–369. https://doi.org/10.1016/S0022-1694(96)03227-1

Stevens Water Monitoring Systems Inc.: The Hydra Probe® Soil Sensor, User's Manual, 1–63, July 2007.

Stewart, R. E., & Kantrud, H. A. (1971). Classification of natural ponds and lakes in the glaciated prairie region (Report No. 92; Resource Publication, p. 64). USGS Publications Warehouse. http://pubs.er.usgs.gov/publication/rp92

Susha Lekshmi, S. U., Singh, D. N., & Shojaei Baghini, M. (2014). A critical review of soil moisture measurement. *Measurement, 54*, 92–105. https://doi.org/10.1016/j.measurement.2014.04.007

Tarantino, A., Ridley, A. M., & Toll, D. G. (2008). Field measurement of suction, water content, and water permeability. *Geotechnical and Geological Engineering*, *26*(6), 751–782. https://doi.org/10.1007/s10706-008-9205-4

Teixeira, W. G., Schroth, G., Marques, J. D., & Huwe, B. (2003). Sampling and TDR probe insertion in the determination of the volumetric soil water content. *Revista Brasileira de Ciência Do Solo, 27*(4), 575–582. https://doi.org/10.1590/S0100-06832003000400001

Teng, J. (2020). Parameterization of soil freezing characteristic curve for unsaturated soils. *Cold Regions Science and Technology*, 8.

Tian, H., Wei, C., Lai, Y., & Chen, P. (2018). Quantification of water content during freeze–thaw cycles: A nuclear magnetic resonance-based method. *Vadose Zone Journal, 17*(1), 160124. https://doi.org/10.2136/vzj2016.12.0124

Tian, Z., Ren, T., Kojima, Y., Lu, Y., Horton, R., & Heitman, J. L. (2017). An improved thermo-time domain reflectometry method for determination of ice contents in partially frozen soils. *Journal of Hydrology*, *555*, 786–796. https://doi.org/10.1016/j.jhydrol.2017.10.055

Tice, A. R., Oliphant, J., Nakano, Y., & Jenkins, T. F. (1982). Relationship between the Ice and Unfrozen Water Phases in Frozen Soil as Determined by Pulsed Nuclear Magnetic Resonance and Physical Desorption Data. /paper/Relationship-between-the-Ice-and-Unfrozen-Water-in-Tice-Oliphant/9e715c26df9c80e22b2547a113599c9cd53a5f51

Topp, G. C., Davis, J. L., & Annan, A. P. (1980). Electromagnetic determination of soil water content: Measurements in coaxial transmission lines. *Water Resources Research*, *16*(3), 574–582. https://doi.org/10.1029/WR016i003p00574

Tuller, M., Or, D., & Hillel, D. (2004). Retention of water in soil and the soil water characteristic curve. *Encyclopedia of Soils in the Environment*, *4*, 278–289.

UMS. (2011). T4/T4e, Pressure Transducer Tensiometer Manual. UMS GmbH, Munich, Germany.

UMS (2015): Manual HYPROP, version 2015-01, 99 pp. UMS GmbH, Gmunder Strabe 37 Munich, Germany. http://ums-muc.de/static/Manual_HYPROP.pd

van Genuchten, M. (1980). A closed-form equation for predicting the hydraulic conductivity of unsaturated soils 1. *Soil Science Society of America Journal*, *44*(5), 892–898. https://doi.org/10.2136/sssaj1980.03615995004400050002x

Vanapalli, S. K., Fredlund, D. G., Pufahl, D. E., & Clifton, A. W. (1996). Model for the prediction of shear strength with respect to soil suction. *Canadian Geotechnical Journal*, *33*(3), 379–392. https://doi.org/10.1139/t96-060

Wallhan, E. F. (1939). Use of tensiometers for soil moisture measurement in ecological research. *Ecology*, *20*(3), 403–412. JSTOR. https://doi.org/10.2307/1930393

Wang, Li, Z., Wang, W. k, & Li, Y. T. (2011). Measurement of soil moisture characteristic curves of sandy medium by sandy funnel method. *2011 International Symposium on*

Water Resource and Environmental Protection, *3*, 1885–1887. https://doi.org/10.1109/ISWREP.2011.5893622

Wang, M., Kong, L., & Zang, M. (2015). Effects of sample dimensions and shapes on measuring soil–water characteristic curves using pressure plate. *Journal of Rock Mechanics and Geotechnical Engineering*, *7*(4), 463–468. https://doi.org/10.1016/j.jrmge.2015.01.002

Watanabe, K., Kito, T., Wake, T., & Sakai, M. (2011). Freezing experiments on unsaturated sand, loam and silt loam. *Annals of Glaciology*, *52*(58), 37–43. https://doi.org/10.3189/172756411797252220

Watanabe, K., & Mizoguchi, M. (2002). Amount of unfrozen water in frozen porous media saturated with solution. *Cold Regions Science and Technology*, *34*(2), 103–110. https://doi.org/10.1016/S0165-232X(01)00063-5

Watanabe, K., & Osada, Y. (2017). Simultaneous measurement of unfrozen water content and hydraulic conductivity of partially frozen soil near 0 °C. *Cold Regions Science and Technology*, *142*, 79–84. https://doi.org/10.1016/j.coldregions.2017.08.002

Watanabe, K., & Wake, T. (2009). Measurement of unfrozen water content and relative permittivity of frozen unsaturated soil using NMR and TDR. *Cold Regions Science and Technology*, *59*(1), 34–41. https://doi.org/10.1016/j.coldregions.2009.05.011

West, L. J., Rippin, D. M., Murray, T., Mader, H. M., & Hubbard, B. (2007). Dielectric permittivity measurements on ice cores: implications for interpretation of radar to yield glacial unfrozen water content. J. Environ. Eng. Geophys., 12,37–45. https://doi.org/10.2113/JEEG12.1.37

Whalley, W. R., Ober, E. S., & Jenkins, M. (2013). Measurement of the matric potential of soil water in the rhizosphere. *Journal of Experimental Botany*, *64*(13), 3951–3963. https://doi.org/10.1093/jxb/ert044

Williams, P. J. (1964). Unfrozen water content of frozen soils and soil moisture suction. *Géotechnique*, *14*(3), 231–246. https://doi.org/10.1680/geot.1964.14.3.231

Williams, P. J. (1970). Properties and behaviour of freezing soils. *Norwegian Geotechnical Institute*, *72*.

Williams, P. J., & Smith, M. W. (1989). The frozen earth. Cambridge University Press.

Wu, D., Zhou, X., & Jiang, X. (2018). Water and salt migration with phase change in saline soil during freezing and thawing processes. *Groundwater*, *56*(5), 742–752. https://doi.org/10.1111/gwat.12605

Xie, S., Jian-jun, Q., Yuan-ming, L., Zhi-wei, Z., & Xiang-tian, X. (2015). Effects of freeze-thaw cycles on soil mechanical and physical properties in the Qinghai-Tibet Plateau. *Journal of Mountain Science*, *12*(4), 999–1009. https://doi.org/10.1007/s11629-014-3384-7

Yan, G., Li, Z., Bore, T., Scheuermann, A., Galindo-Torres, S., & Li, L. (2017). The measurement of primary drainage curve using hanging column and large soil column test. ResearchGate. https://www.researchgate.net/publication/318734619

Yao, Y.-S., Zheng, J.-L., Chen, Z.-S., Zhang, J.-H., & Li, Y. (2016). Field measurements and numerical simulations of temperature and moisture in highway engineering using a frequency domain reflectometry sensor. *Sensors (Basel, Switzerland)*, *16*(6). https://doi.org/10.3390/s16060857

Yoshikawa, K., & Overduin, P. P. (2005). Comparing unfrozen water content measurements of frozen soil using recently developed commercial sensors. *Cold Regions Science and Technology*, *42*(3), 250–256. https://doi.org/10.1016/j.coldregions.2005.03.001

Zhang, C., & Liu, Z. (2018). Freezing of water confined in porous materials: role of adsorption and unfreezable threshold. *Acta Geotechnica*, *13*(5), 1203–1213. https://doi.org/10.1007/s11440-018-0637-6

Zhang, M., Zhang, X., Lai, Y., Lu, J., & Wang, C. (2020). Variations of the temperatures and volumetric unfrozen water contents of fine-grained soils during a freezing–thawing process. *Acta Geotechnica*, *15*(3), 595–601. https://doi.org/10.1007/s11440-018-0720-z

Zhang, S., Teng, J., He, Z., & Sheng, D. (2016). Importance of vapor flow in unsaturated freezing soil: a numerical study. *Cold Regions Science and Technology*, *126*, 1–9. https://doi.org/10.1016/j.coldregions.2016.02.011

Zhang, T., Barry, R., Knowles, K., Ling, F., & Armstrong, R. L. (2003). Distribution of seasonally and perennially frozen ground in the Northern Hemisphere. *Proc. 8th Int. Conf. Permafrost*, *2*, 1289–1294.

Zhao, Y., Si, B., He, H., Xu, J., Peth, S., Horn, R., Zhao, Y., Si, B., He, H., Xu, J., Peth, S., & Horn, R. (2016). Modeling of coupled water and heat transfer in freezing and thawing soils, inner Mongolia. *Water*, *8*(10), 424. https://doi.org/10.3390/w8100424

Zhou, J., Wei, C., Lai, Y., Wei, H., & Tian, H. (2018). Application of the generalized clapeyron equation to freezing point depression and unfrozen water content. *Water Resources Research*, *54*(11), 9412–9431. https://doi.org/10.1029/2018WR023221

Zhou, X., Zhou, J., Kinzelbach, W., & Stauffer, F. (2014). Simultaneous measurement of unfrozen water content and ice content in frozen soil using gamma ray attenuation and TDR. *Water Resources Research*, *50*(12), 9630–9655. https://doi.org/10.1002/2014WR015640

LIST OF APPENDICES

Appendix A: Tables

Table A-1: Raw data for particle density measured using the pycnometer method

M_1 (g)	V_1 (cm^3)	(M_2) g	M_s=M_2-M_1 (g)	V_w (cm^{-3})	V_s =V_1-V_w (cm^3)	$\rho_s = (M_s/V_s)$ ($g\ cm^{-3}$)
55.35	125	190.87	135.52	70.63	54.37	2.493

Where ρ_s is particle density, M_1 is the mass of the empty pycnometer, M_2 is the mass of pycnometer and soil, V_1 is the total volume of the pycnometer, V_W is the volume of water used to top up the flask to the 125 cm^{-3} mark.

Table A-2: Raw data for soil porosity

Replicates	V_t (cm^{-3})	V_{w1} (cm^{-3})	V_{w2} (cm^{-3})	$V_{w2} - V_{w1}$ (V_s) (cm^{-3})	$V_t - V_s(V_f)$ (cm^{-3})	$\eta = V_f/V_t$
1	73	39	83	44	30	0.41
2	41	52	76	24	17	0.42
Average						0.415

Where η is the measured soil porosity, $\boldsymbol{V_t}$ is the total volume of the soil, $\boldsymbol{V_{w1}}$ is the volume of water in a cylinder, $\boldsymbol{V_{w2}}$ is the volume of the measured after pouring soil into the water in the cylinder, and $\boldsymbol{V_f}$ is the volume occupied by water.

Table A-3: Original data for the particle size distribution of the silica sand measured using the mechanical shaking method

Gravel	Coarse Sand	Medium Sand	Fine Sand	Silt	Clay	
> 4.75 mm	2 to 4.75 mm	0.425 to 2 mm	0.075-0.425 mm	0.005 - 0.075 mm	<0.002 mm	sum (%)
0.0	0.0	31.3	68.7	0	0	0
Sieve Number	**Aperature Diameter (mm)**	**Mass: Sieve + Soil (g)**	**Sieve Mass (g)**	**Cumulative Mass (g)**	**Cumulative % Retained**	**% Passing**
3	74.5			0	0.0%	100.0%
2	50			0	0.0%	100.0%
1.5	37.5			0	0.0%	100.0%
1 inch	24.5	751.66	751.66	0	0.0%	100.0%
3/4	19	512.5	512.5	0	0.0%	100.0%
3/8	9.5	492.29	492.29	0	0.0%	100.0%
4	4.75	482.59	482.59	0	0.0%	100.0%
10	2	440.24	440.24	0	0.0%	100.0%
20	0.85	370.68	370.02	0.66	0.2%	99.8%
40	0.425	468.29	341.52	127.43	31.3%	68.7%
60	0.25	590.86	333.44	384.85	94.6%	5.4%
100	0.15	330.93	309.07	406.71	100.0%	0.0%
200	0.075	305.17	305.05	406.83	100.0%	0.0%
pan		362.2	362.1	406.91	100.0%	0.0%

Table A-4: Original data from the HYPROP apparatus which was used in constructing the SMC of the silica sand

pF [-]	Water Content [Vol%]
1.499	35.39
1.439	35.36
1.336	35.33
1.216	35.28
1.196	35.23
1.267	35.16
1.329	35.07
1.351	34.97
1.351	34.87
1.342	34.77
1.329	34.65
1.318	34.53
1.31	34.43
1.298	34.33
1.288	34.21
1.286	34.09
1.283	33.97
1.278	33.83
1.271	33.7
1.255	33.55
1.247	33.39
1.25	33.23
1.25	33.05
1.252	32.87
1.253	32.68
1.257	32.49

1.263	32.28
1.266	32.07
1.269	31.85
1.272	31.62
1.275	31.39
1.279	31.14
1.281	30.88
1.284	30.62
1.286	30.36
1.289	30.08
1.292	29.79
1.294	29.48
1.296	29.18
1.298	28.87
1.301	28.55
1.303	28.22
1.306	27.88
1.308	27.53
1.311	27.18
1.313	26.81
1.315	26.44
1.318	26.05
1.32	25.67
1.323	25.27
1.325	24.86
1.327	24.45
1.33	24.03
1.333	23.59
1.335	23.15
1.332	22.7

1.331	22.24
1.337	21.78
1.339	21.31
1.339	20.84
1.338	20.36
1.337	19.88
1.336	19.39
1.336	18.89
1.338	18.34
1.34	17.76
1.34	17.21
1.341	16.67
1.343	16.11
1.345	15.55
1.347	14.97
1.35	14.38
1.353	13.77
1.356	13.14
1.36	12.51
1.364	11.87
1.368	11.22
1.373	10.56
1.378	9.89
1.384	9.22
1.39	8.54
1.397	7.86
1.405	7.17
1.414	6.48
1.425	5.79
1.437	5.11

1.451	4.49
1.466	3.94
1.481	3.47
1.492	3.09
1.5	2.82
1.511	2.64
1.532	2.48
1.581	2.33
1.764	2.19
2.038	2.06
2.145	1.94
2.165	1.82
2.184	1.71

Appendix B: Figures

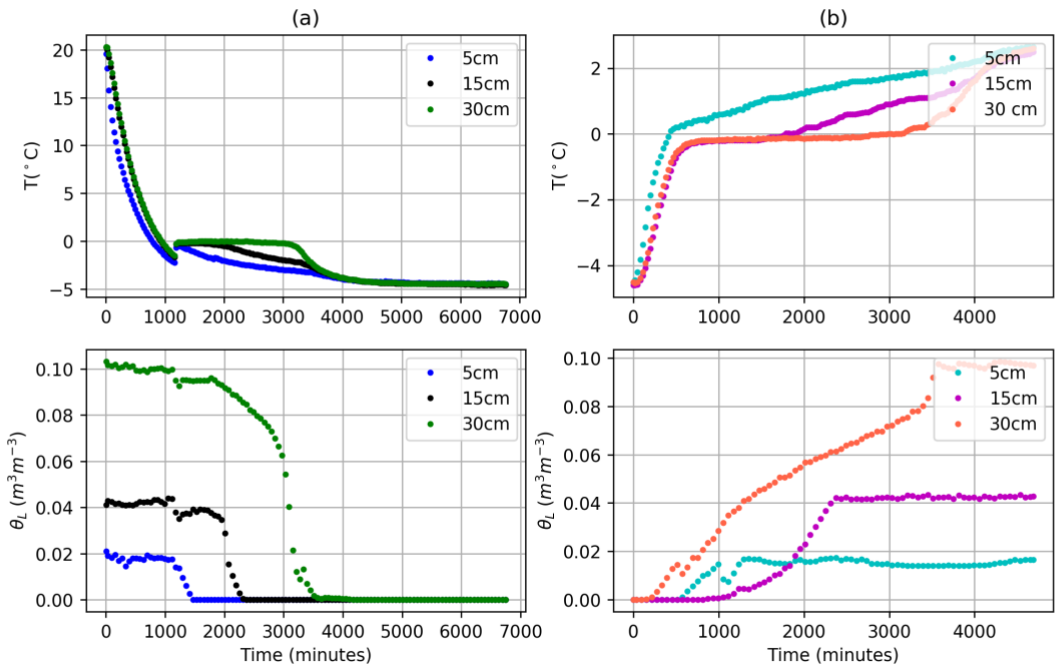

Figure B-1: Time series plot for soil temperature and moisture content for 0 $g\ l^{-1}$ salt concentration at a target moisture content of 0.05 $m^3\ m^{-3}$ a) freezing b) thawing

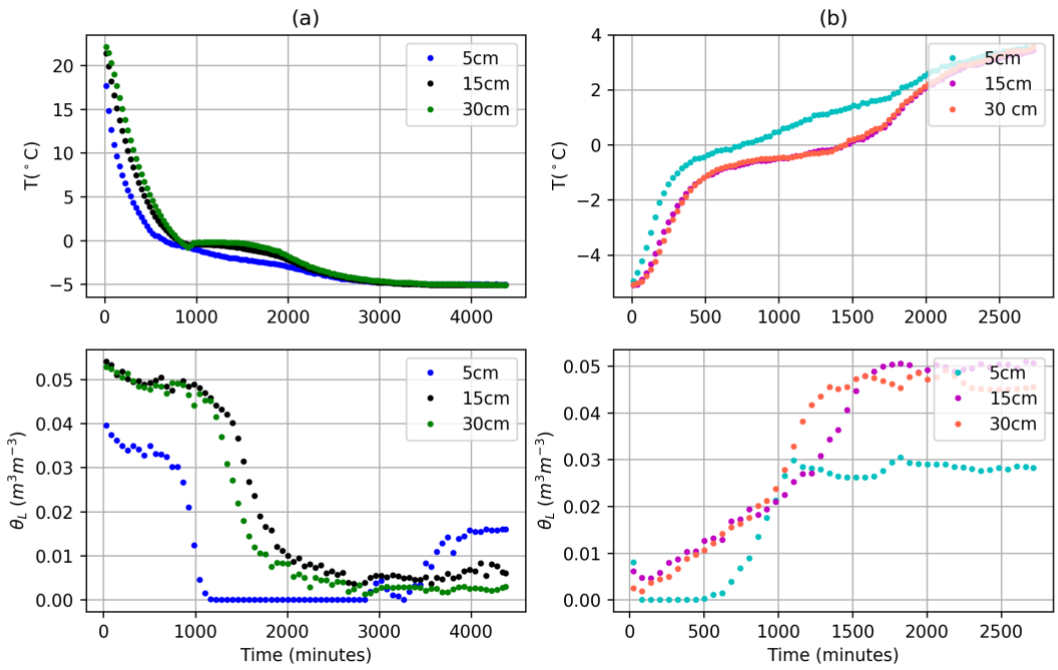

Figure B-2: Time series plot for soil temperature and moisture content for 2 $g\ l^{-1}$ salt concentration at a target moisture content of 0.05 $m^3\ m^{-3}$ a) freezing b) thawing

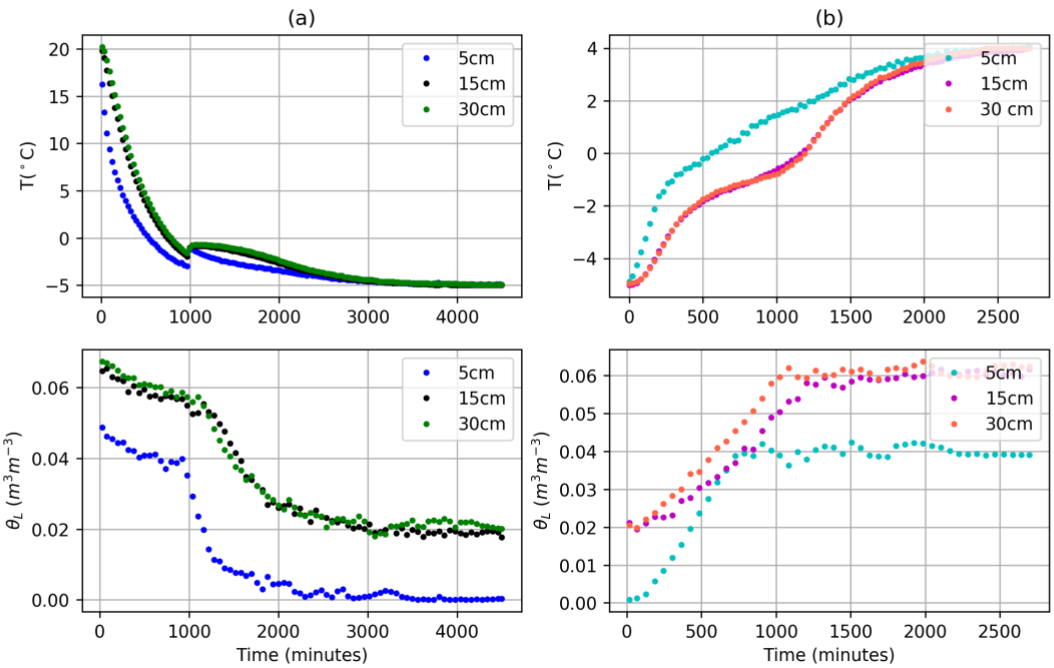

Figure B-3: Time series plot for soil temperature and moisture content for 8 $g\ l^{-1}$ salt concentration at a target moisture content of 0.05 $m^3\ m^{-3}$ a) freezing b) thawing

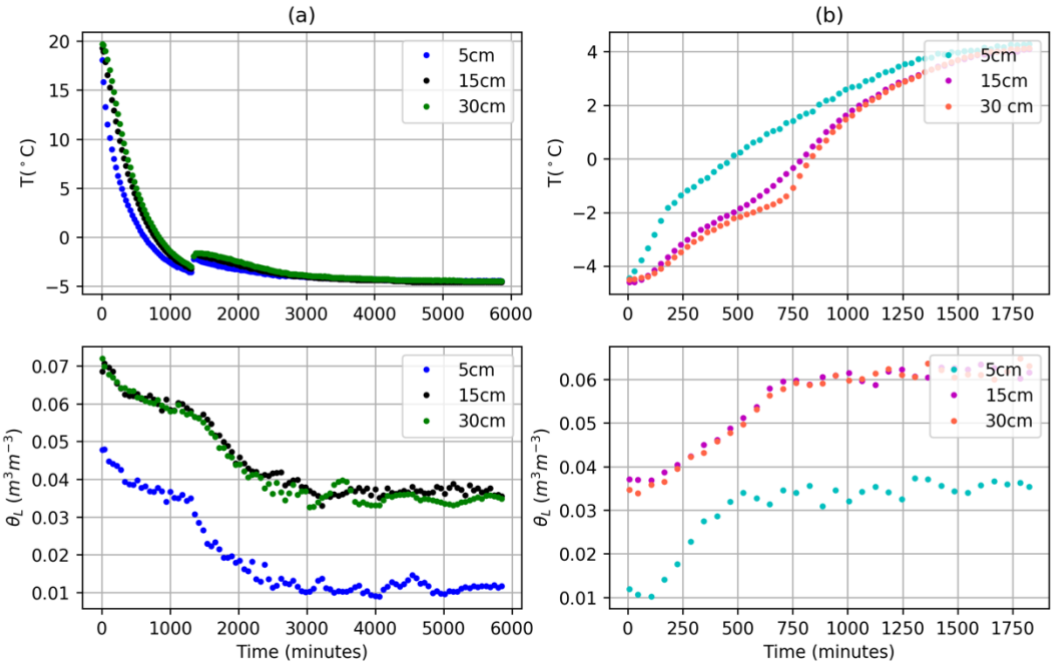

Figure B-4: Time series plot for soil temperature and moisture content for 16 $g\ l^{-1}$ salt concentration at a target moisture content of 0.05 $m^3\ m^{-3}$ a) freezing b) thawing

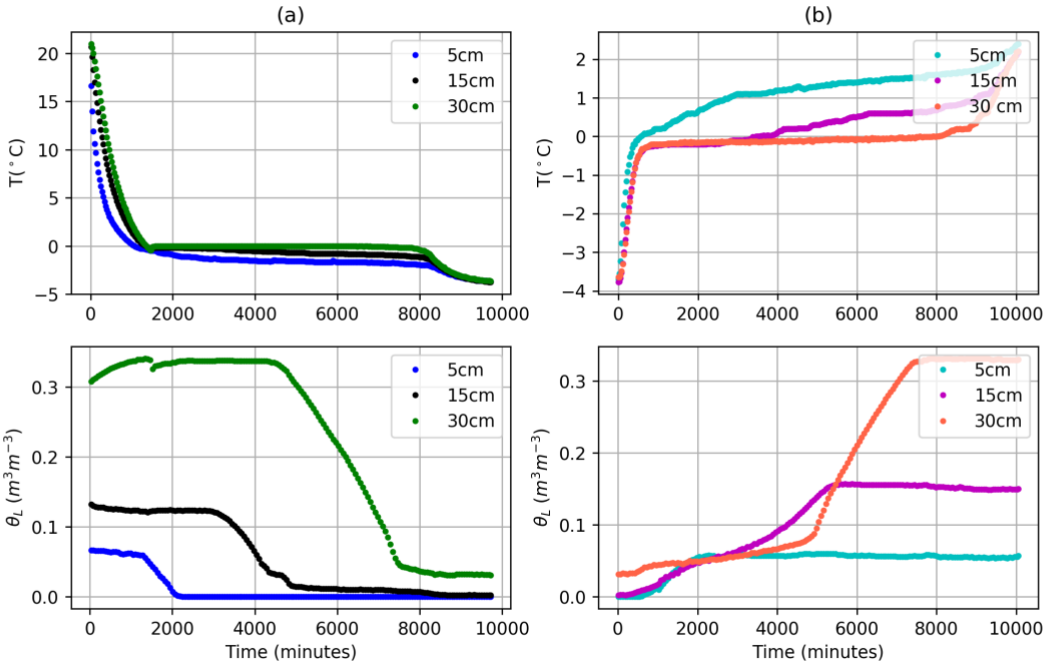

Figure B-5: Time series plot for soil temperature and moisture content for 0 $g\ l^{-1}$ salt concentration at a target moisture content of 0.24 $m^3\ m^{-3}$ a) freezing b) thawing

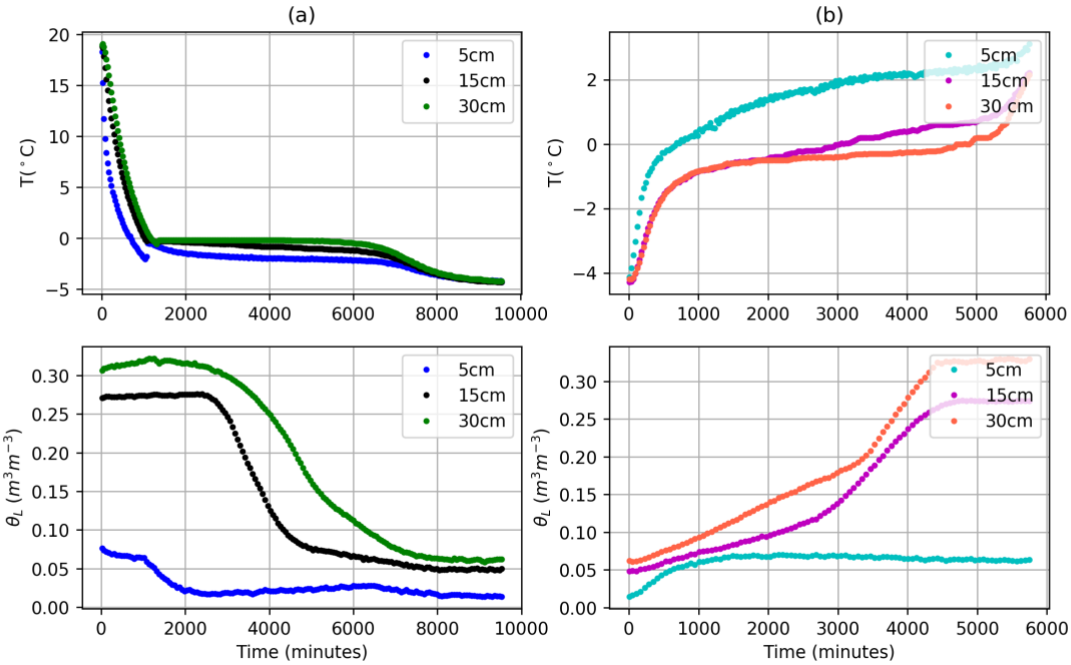

Figure B-6: Time series plot for soil temperature and moisture content for 2 $g\ l^{-1}$ salt concentration at a target moisture content of 0.24 $m^3\ m^{-3}$ a) freezing b) thawing

Figure B-7: This picture shows a routine inspection of the experiment